UNIVERSIDADE FEDERAL DE JUIZ DE FORA
FACULDADE DE ENGENHARIA & INSTITUTO DE CIÊNCIAS EXATAS
PROGRAMA DE PÓS-GRADUAÇÃO EM MODELAGEM COMPUTACIONAL

Guilherme Martins Couto

Modulation of Cardiac Arrhythmogenesis by Spatially Correlated Fibrosis

Juiz de Fora

2026

Guilherme Martins Couto

Modulation of Cardiac Arrhythmogenesis by Spatially Correlated Fibrosis

Dissertação apresentada ao Programa de Pós-Graduação em Modelagem Computacional da Universidade Federal de Juiz de Fora como requisito parcial à obtenção do título de Mestre em Modelagem Computacional. Área de concentração: Modelagem Computacional.

Orientador: Prof. Dr. Rodrigo Weber dos Santos

Coorientador: Prof. Dr. Joventino de Oliveira Campos

Juiz de Fora

2026

Ficha catalográfica elaborada através do Modelo Latex do CDC da UFJF
com os dados fornecidos pelo(a) autor(a)

Couto, Guilherme Martins.
Modulation of Cardiac Arrhythmogenesis by Spatially Correlated Fibrosis / Guilherme Martins Couto. – 2026.
96 f. : il.

Orientador: Rodrigo Weber dos Santos
Coorientador: Joventino de Oliveira Campos
Dissertação (Mestrado) – Universidade Federal de Juiz de Fora, Faculdade de Engenharia & Instituto de Ciências Exatas. Programa de Pós-Graduação em Modelagem Computacional, 2026.

1. Fibrose. 2. Arritmia. 3. Eletrofisiologia Computacional. 4. Caracterização Estrutural. I. Santos, Rodrigo Weber dos, orient. II. Campos, Joventino de Oliveira, coorient. III. Título.

Guilherme Martins Couto

Modulation of Cardiac Arrhythmogenesis by Spatially Correlated Fibrosis

Dissertação apresentada ao Programa de Pós-graduação em Modelagem Computacional da Universidade Federal de Juiz de Fora como requisito parcial à obtenção do título de Mestre em Modelagem Computacional. Área de concentração: Modelagem Computacional.

Aprovada em 25 de junho de 2026.

BANCA EXAMINADORA

Prof. Dr. Rodrigo Weber dos Santos - Orientador
Universidade Federal de Juiz de Fora

Prof. Dr. Brodie A. J. Lawson
Queensland University of Technology, Austrália

Prof. Dr. Bernardo Martins Rocha
Universidade Federal de Juiz de Fora

Juiz de Fora, 26/06/2026.

Documento assinado eletronicamente por **Rodrigo Weber dos Santos**, **Professor(a)**, em 26/06/2026, às 16:08, conforme horário oficial de Brasília, com fundamento no § 3º do art. 4º do Decreto nº 10.543, de 13 de novembro de 2020.

Documento assinado eletronicamente por **Brodie Lawson**, **Usuário Externo**, em 01/07/2026, às 19:50, conforme horário oficial de Brasília, com fundamento no § 3º do art. 4º do Decreto nº 10.543, de 13 de novembro de 2020.

Documento assinado eletronicamente por **Bernardo Martins Rocha**, **Professor(a)**, em 03/07/2026, às 08:59, conforme horário oficial de Brasília, com fundamento no § 3º do art. 4º do Decreto nº 10.543, de 13 de novembro de 2020.

A autenticidade deste documento pode ser conferida no Portal do SEI-Ufjf (www2.ufjf.br/SEI) através do ícone Conferência de Documentos, informando o código verificador **3052170** e o código CRC **28E1B23D**.

Dedico este trabalho aos meus pais, Fátima e Gustavo,
que sempre me incentivaram a ser curioso.

AGRADECIMENTOS

Há pouco mais de dois anos, quando tomei a decisão de fazer um mestrado, não imaginava que, em pouco tempo, eu passaria por transformações tão importante em minha vida. Foram meses intensos com muitos desafios e aprendizados, porém nunca solitários. Das poucas certezas que carrego, saber que ninguém faz nada sozinho talvez seja a principal delas. Portanto, em nome do que cultivo e do que acredito e por ter pessoas tão incríveis ao meu lado, que foram decisivas nessa minha caminhada, faço questão de expressar a minha gratidão.

Em primeiro lugar, aos meus pais, Fátima e Gustavo, que acreditam no poder transformador da educação e em mim. Infelizmente, concluir um mestrado ainda é um privilégio para poucos, e eu só cheguei até aqui graças ao apoio e dedicação incansáveis deles que garantiram tudo que eu precisei. Para sempre, o que eu fizer será dedicado a vocês — em forma de agradecimento, por amor e admiração.

Junto com meus pais, minha irmã Lívia é uma das grandes responsáveis por eu ser quem sou. Durante esses dois anos, moramos juntos, e, dentre tantas outras coisas que ela me ensinou sobre a vida, aprendi, com ela, o verdadeiro e profundo sentido da palavra casa. Obrigado, minha irmã, pelas conversas, pelo sorriso, pela companhia e pelo exemplo. Você é muito especial!

Nessa reta final, conheci a Aline, e meus dias passaram a ter mais luz e mais cores. Desse nosso encontro tão lindo, a partir de nossas trocas, nossa parceria e minha admiração, passei a ter — pela lente do amor — uma nova perspectiva sobre as coisas do mundo, sobre pesquisar e fazer ciência, sobre a arte, sobre lidar com as pessoas e, é claro, sobre amar. Obrigado por estar ao meu lado. Sou muito feliz e grato por tudo que temos cultivado até aqui e espero que continuemos florescendo por muito mais tempo.

Não posso deixar jamais de agradecer aos meus amigos que são parte fundamental de quem sou. Assim, agradeço imensamente a Bia, Gabriel, Vitória, Petito, Gustavo, Lucas, Hannah, Sarah, Ana, Thiago, Yan e Mayra. Por vocês, todo o meu amor e carinho. Obrigado por terem estado comigo em cada momento desses últimos anos e por me ensinarem tanto.

Também quero agradecer ao Laboratório de Fisiologia Computacional, ao Programa de Pós-graduação em Modelagem Computacional e a todos os colegas que conheci nesses espaços e me acolheram. As nossas conversas, aulas, reuniões e pausas para café foram determinantes em minha trajetória e trouxeram-me valiosos aprendizados.

Aos meus orientadores, Rodrigo e Joventino, gostaria de registrar meu mais profundo respeito e gratidão por tudo que tenho aprendido com vocês ao longo desses anos que se estendem para além do mestrado. Foi graças ao estímulo e confiança que tiveram em mim que pude construir este e outros trabalhos. Foram vocês que me mostraram os caminhos

da pesquisa acadêmica e despertaram em mim essa paixão.

Por fim, agradeço a Universidade Federal de Juiz de Fora, pública e de qualidade, por ter me acolhido e proporcionado o ambiente ideal para minha formação. Estendo, pelo financiamento e disponibilidade de recursos, meus agradecimentos ao CNPq, CAPES, FAPEMIG, EBSERH, FINEP e SINAPAD Santos-Dumont.

— Como é belo o mundo e como são horríveis os labirintos! — eu disse, aliviado.
— Como seria belo o mundo se houvesse uma regra para andar pelos labirintos — respondeu o meu mestre.
(Umberto Eco; tradução de Aurora Fornoni Bernardini, Homero Freitas de Andrade. *O nome da rosa*. 26. ed. Editora Record, 2024, p. 213)

RESUMO

A fibrose cardíaca cria barreiras estruturais que perturbam a propagação elétrica, precipitando arritmias. Modelos computacionais frequentemente aproximam a fibrose utilizando ruído aleatório não correlacionado, negligenciando a complexa microarquitetura do tecido biológico. Neste trabalho, investigamos como diferentes estruturas fibróticas inspiradas em histologia interagem com ondas de propagação para modular a reentrada sustentada. Estendemos um gerador baseado em ruído Perlin — introduzindo um modo de composição de fibrose para alta densidade e suporte a zonas de borda — para sintetizar padrões *compact*, *diffuse*, *interstitial* e *patchy*. Essas arquiteturas foram caracterizadas por meio de um conjunto de descritores morfológicos e topológicos e pela teoria da percolação. Em seguida, realizamos simulações eletrofisiológicas em domínios 2D e 3D utilizando a formulação do monodomínio acoplada a um modelo celular ventricular detalhado, adaptado para reproduzir hipóxia aguda. Os resultados revelaram que padrões espacialmente correlacionados possuem limiares de percolação mais elevados do que o ruído não correlacionado, produzindo perfis de vulnerabilidade distintos. A fibrose *compact*, caracterizada por aglomerados maciços e densos, ancorou circuitos estáveis com fracionamento mínimo de ondas, apresentando o menor risco relativo de reentrada entre os padrões. Em contrapartida, a fibrose *diffuse* fracionou significativamente as frentes de onda, criando múltiplos pontos de ancoragem e a maior incidência de reentrada. As arquiteturas *interstitial* e *patchy* forçaram condução tortuosa em zigue-zague; notavelmente, a fibrose *patchy* foi o único padrão que exibiu maior arritmogenicidade em 3D, utilizando sua combinação de filamentos alongados e macroestrutura densas para estabilizar ondas de rolagem. A quantificação dessas interações onda-topologia fornece uma base para embasar modelos computacionais mais precisos e conscientes da geometria da fibrose cardíaca e da sua arritmogênese.

Palavras-chave: fibrose, arritmia, eletrofisiologia computacional; caracterização estrutural.

ABSTRACT

Cardiac fibrosis creates structural barriers that disrupt electrical propagation, precipitating arrhythmias. Computational models frequently approximate fibrosis using uncorrelated random noise, neglecting the complex micro-architecture of biological tissue. Here, we investigated how different histology-inspired fibrotic structures interact with propagating waves to modulate sustained reentry. We extended a Perlin noise-based generator — introducing a high-density composition mode and border zone support — to synthesize *compact*, *diffuse*, *interstitial*, and *patchy* patterns. These architectures were characterized using a set of morphological and topological descriptors and percolation theory. Subsequently, we conducted electrophysiological simulations across 2D and 3D domains using the monodomain formulation coupled with a detailed ventricular cellular model adapted to reproduce acute hypoxia. The results revealed that spatially correlated patterns possess higher percolation thresholds than uncorrelated noise, yielding distinct vulnerability profiles. *Compact* fibrosis, characterized by massive and dense clusters, anchored stable circuits with minimal wave fractionation, presenting the lowest relative reentry risk among the patterns. Conversely, *diffuse* fibrosis significantly fractionated wavefronts, creating multiple anchoring points and the highest reentry incidence. *Interstitial* and *patchy* architectures forced tortuous, zigzag conduction; notably, *patchy* fibrosis was the only pattern that exhibited increased arrhythmogenicity in 3D, utilizing its combination of elongated strands and dense macro-structures to stabilize scroll waves. Quantifying these topology-specific wave interactions provides a foundation to inform more accurate and geometry-conscious computational modeling of cardiac fibrosis and arrhythmogenesis.

Keywords: fibrosis; arrhythmia; computational electrophysiology; structural characterization.

LIST OF FIGURES

LIST OF TABLES

SUMARY

1 INTRODUCTION

Cardiovascular diseases remain the leading cause of mortality worldwide, with sudden cardiac death (SCD) accounting for a significant proportion of these fatalities. The vast majority of SCD episodes are precipitated by lethal ventricular arrhythmias, such as ventricular tachycardia and fibrillation, which arise from profound disruptions in the heart's electrical propagation. A primary structural driver responsible for creating the arrhythmogenic substrate that sustains these life-threatening electrical disturbances is cardiac fibrosis. Understanding the complex mechanisms by which this structural remodeling dictates wave propagation is one of the most relevant challenges in electrophysiology and computational cardiology.

1.1 PATHOPHYSIOLOGY OF CARDIAC FIBROSIS AND METABOLIC HYPOXIA

The myocardium is a composite excitable medium characterized by a complex cellular organization supported by an extracellular matrix (ECM). Under healthy conditions, a delicate balance is maintained between contracting cardiomyocytes and the cardiac fibroblasts responsible for ECM turnover (CAMELLITI; BORG; KOHL, 2005). However, following cardiac injury or systemic inflammation, fibroblasts undergo a phenotypic conversion into active myofibroblasts, leading to the excessive accumulation of ECM proteins, particularly collagen. This pathological remodeling, known as cardiac fibrosis, manifests primarily through two pathogenic mechanisms: *reparative* and *reactive* fibrogenesis (TALMAN; RUSKOAHO, 2016; FRANGOGIANNIS, 2021; GLASHAN et al., 2018; MARUYAMA; IMANAKA-YOSHIDA, 2022; BOER et al., 2019).

Reparative (or replacement) fibrosis is triggered by localized cardiomyocyte necrosis, most commonly following a myocardial infarction, resulting in a dense collagen scar. While critical for preventing ventricular rupture, it creates massive macroscopic barriers within the myocardial electrical syncytium (TALMAN; RUSKOAHO, 2016; FRANGOGIANNIS, 2021; BOER et al., 2019). In contrast, reactive fibrosis is an initially adaptive response to chronic stimuli (e.g., pressure overload or ageing) characterized by excessive ECM deposition within interstitial spaces without direct cell death. This progressively stiffens the myocardium and creates pervasive microscopic barriers (TALMAN; RUSKOAHO, 2016; FRANGOGIANNIS, 2021; BOER et al., 2019). These two primary fibrotic pathways are schematically contrasted in Fig. 1. In advanced stages of heart failure, reparative and reactive fibrosis frequently coexist, creating a highly heterogeneous tissue landscape (GLASHAN et al., 2018; MARUYAMA; IMANAKA-YOSHIDA, 2022; BOER et al., 2019).

Clinical evidence establishes fibrosis as a risk factor that drastically worsens patient prognosis and increases the likelihood of SCD (GULATI et al., 2013; LUNDE et al., 2024).

Figure 1 – Morphological comparison between reactive and reparative (or replacement) cardiac fibrosis. Reactive fibrogenesis (middle panels) is characterized by accumulation of ECM proteins and perivascular bundling without direct cell death, acting as pervasive microscopic barriers that stiffen the tissue. In contrast, replacement fibrosis (right panels) is triggered by cardiomyocyte necrosis (e.g., myocardial infarction), where activated myofibroblasts deposit a dense collagen scar to replace dead cells, creating a dense barrier for electrical propagation.

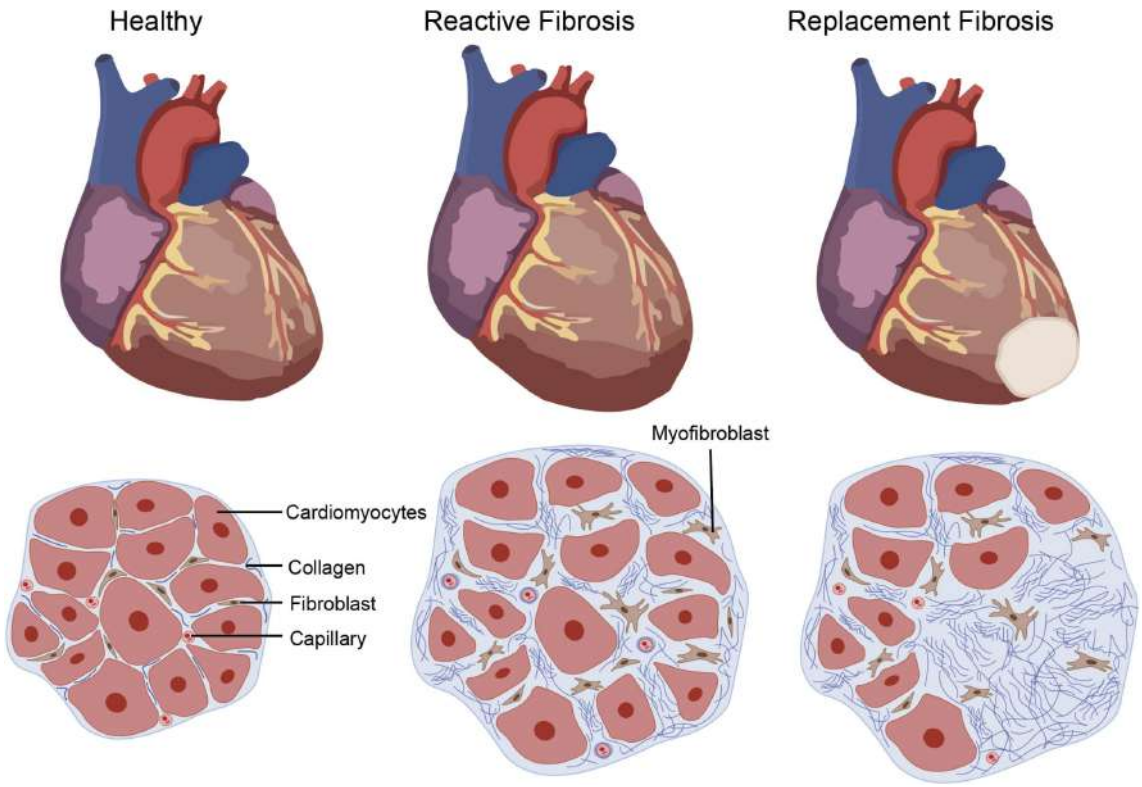

Source: Adapted from Zeng *et al.* (ZENG et al., 2024).

The pathological impact of this remodeling extends beyond pure structural discontinuity; it is intimately coupled with a compromised metabolic microenvironment (VERHEULE; SCHOTTEN, 2021). The expansion of the ECM increases oxygen diffusion distances, frequently subjecting fibrotic regions to localized hypoxia (DARBY; HEWITSON, 2016). Furthermore, hypoxia and inflammation often act as primary triggers for fibrogenesis in conditions such as respiratory disorders, viral infections, or recurrent ischemic episodes (BRADLEY; FLORAS, 2009; YEGHIAZARIANS et al., 2021; MARIN-NETO et al., 2007; TSCHÖPE et al., 2021). Regardless of the initiating mechanism, the simultaneous presence of structural barriers and functional hypoxia is a common denominator in arrhythmogenesis (SACHETTO; ALONSO; SANTOS, 2018; OLIVEIRA et al., 2018). Hypoxia abbreviates the cardiac Action Potential Duration (APD) and depresses excitability. The interplay between abbreviated wavelengths and structural tortuosity creates an unstable and dangerous dynamic medium (SHAW; RUDY, 1997; SACHETTO; ALONSO; SANTOS, 2018; ZHAO et al., 2023), these mechanisms will be more detailed in Sec. 1.3.

1.2 COMPLEX PROPAGATION IN CARDIAC ELECTROPHYSIOLOGY

It is possible to see that fibrosis transforms the myocardium into a heterogeneous medium populated by non-conducting obstacles. The interaction between electrical propagating waves and these barriers is a primary driver of wavefront fractionation and sustained reentrant circuits associated with arrhythmia (WINFREE, 1991; ALONSO; SANTOS; BÄR, 2016; ALONSO; BÄR; ECHEBARRIA, 2016). Crucially, the arrhythmogenic potential of these obstacles is determined not merely by their total density (MCDOWELL et al., 2011; MORITA et al., 2009; NGUYEN; QU; WEISS, 2014; BALABAN et al., 2018), but by their specific architecture as demonstrated by several studies (KAWARA et al., 2001; NGUYEN; QU; WEISS, 2014; JONG et al., 2011; TUSSCHER; PANFILOV, 2007; MYKLEBUST; MALECKAR; AREVALO, 2024; DOKUCHAEV; PANFILOV; SOLOVYOVA, 2020; DISERTORI; MASÈ; RAVELLI, 2017; MASÈ et al., 2024; OKENOV et al., 2025).

Histological investigations categorize the fibrotic textures into four major distinct phenotypes (KAWARA et al., 2001; NGUYEN; QU; WEISS, 2014; JONG et al., 2011; GLASHAN et al., 2018): *compact* (dense and large scars); *diffuse* (scattered collagen deposits introducing microscopic heterogeneities) (KAWARA et al., 2001; JONG et al., 2011; NGUYEN; QU; WEISS, 2014); *interstitial* (reticular meshes expanding endomysial spaces, impairing transverse propagation and promoting zigzag conduction) (BAKKER et al., 1993; KUDRYASHOVA et al., 2019); and *patchy* (long and irregular strands separating entire muscle bundles) (KAWARA et al., 2001; NEZLOBINSKY; SOLOVYOVA; PANFILOV, 2020). The architecture of these four classifications are visually represented through histologically derived binary maps in Fig. 2 (LAWSON et al., 2024), highlighting the complex spatial correlation inherent to each pattern.

Computational modeling is indispensable for dissecting these interconnected mechanisms (CAMPOS et al., 2013; SACHETTO; ALONSO; SANTOS, 2018; OLIVEIRA et al., 2018; LAWSON et al., 2020; O'HARA et al., 2022; PEREIRA et al., 2024; SOARES et al., 2025; TRAYANOVA; CHANG, 2016). However, capturing the spatial correlation inherent to real cardiac fibrosis remains challenging (CLAYTON et al., 2011), as clinical imaging often lacks sufficient resolution (HASSAN; BARRETT; CROSSMAN, 2020; RAVASSA et al., 2023). Consequently, *in silico* studies frequently approximate fibrotic substrates using a *uniform* probability distribution per pixel, giving each one the same chance of being considered fibrotic or not, as illustrated in Fig. 3 (SACHETTO; ALONSO; SANTOS, 2018). This approach results in fibrosis being represented by random white noise that is not spatially autocorrelated. While fundamental for understanding classical site percolation (SAHIMI, 1994), these models lack the structure typical of biological systems (LAWSON et al., 2024).

Figure 2 – Histologically derived binary maps of the four primary fibrosis classifications. The segmented profiles illustrate representative sections (1.84 × 2.94 mm) used to extract spatial features for computational texturing: *interstitial*, *compact*, *diffuse*, and *patchy*.

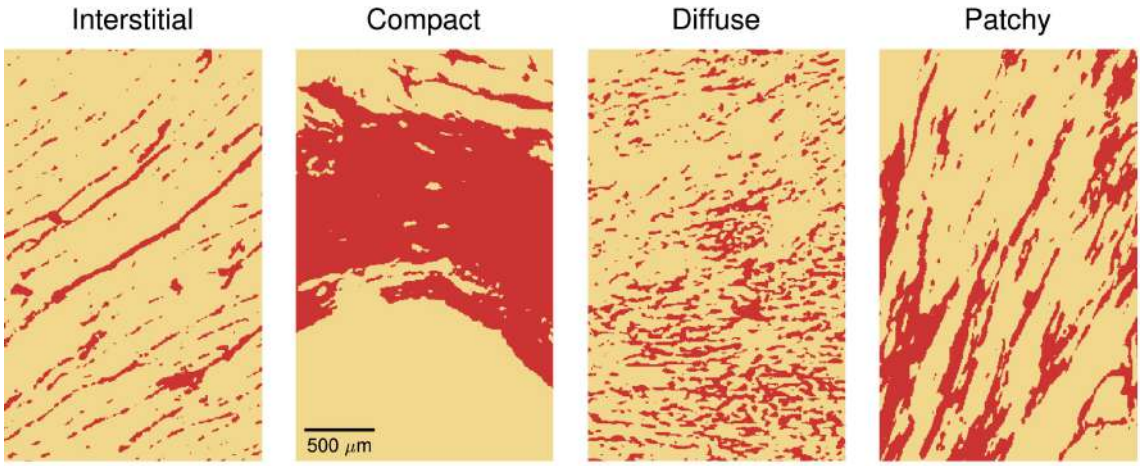

Source: Adapted from Lawson *et al.* (LAWSON et al., 2024), based on original histological slices by de Jong *et al.* (JONG et al., 2011).

Figure 3 – Computational modeling of diffuse fibrosis using a *uniform* probability distribution per pixel, giving each one the same chance of being considered fibrotic or not, resulting in a random white noise. The snapshot illustrates a transmembrane potential wavefront fractionating through a 4 × 4 cm slab where fibrotic obstacles were assigned with a *uniform* spatial probability.

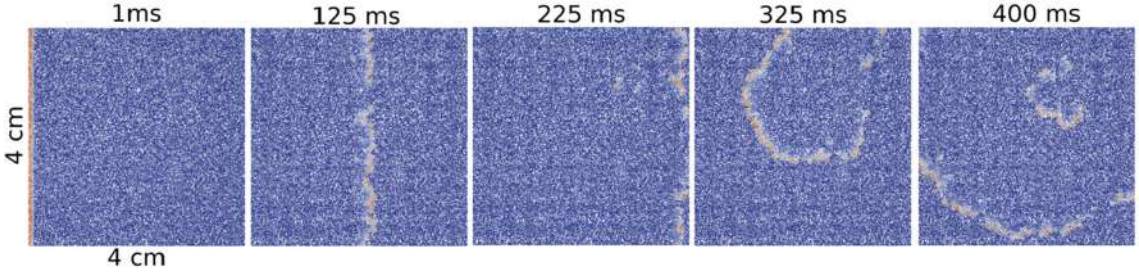

Source: Adapted from Sachetto *et al.* (SACHETTO; ALONSO; SANTOS, 2018).

1.3 BIOPHYSICAL MECHANISMS OF ARRHYTHMOGENESIS: SOURCE-SINK MISMATCH AND CONDUCTION BLOCKS

The mechanism through which micro-structural fibrotic remodeling triggers sustained reentrant arrhythmias relies fundamentally on the balance of electrotonic currents, a phenomenon governed by the *source-sink* relationship. The *source* is defined as the local intracellular depolarizing current generated by the active upstroke of cardiomyocytes undergoing action potential. Conversely, the *sink* represents the downstream passive membrane area of adjacent unexcited cells at their resting potential that must absorb this

current to reach their activation threshold (CIACCIO et al., 2018).

Under healthy physiological conditions, the structural uniformity of the myocardial syncytium ensures a high conduction safety factor, meaning the source current generated by an advancing wavefront significantly exceeds the requirements of the downstream sink. However, the structural interposition of non-conducting collagen obstacles disrupts this equilibrium, destabilizing propagation through two interdependent phenomena:

1. **Source-Sink Mismatch at Structural Expansions:** When a wavefront navigating through a highly tortuous or constricted myocardial corridor (such as a narrow anatomical isthmus embedded within an *interstitial* or *diffuse* network) emerges into a large unremodeled excitable region, the small volume of active myocytes inside the channel (a restricted source) struggles to deliver sufficient charge to depolarize the vast unexcited volume ahead (a massive sink) (OLIVEIRA et al., 2018; CIACCIO et al., 2018). This sudden dissipation of electrotonic current causes a severe localized drop in the conduction safety factor, inducing conduction delays or complete propagation failure, establishing the first necessary condition for a micro-reentry (as schematically illustrated in Fig. 4b).

2. **Generation of Unidirectional Conduction Blocks:** For a sustained reentrant circuit to establish itself, an advancing wavefront must experience a unidirectional block, a condition in which conduction fails in one direction but successfully propagates through an alternative route. While structural asymmetry can mechanically induce this block via direction-dependent source-sink mismatches (OLIVEIRA et al., 2018; CIACCIO et al., 2018) explained above, unidirectional block is also intimately linked to functional tissue heterogeneity. In a remodeled or ischemic substrate, spatial dispersion of cell repolarization creates a highly non-uniform distribution of refractoriness. When a propagating wavefront encounters a region where cells remain within their effective refractory period, that specific segment of the wave is blocked. Then, for the surviving portions of the wavefront to navigate an alternative route and successfully re-excite the initially blocked pathway, the spatial wavelength of the electrical impulse (APD $\times$ Conduction Velocity (CV)) must be shorter than the anatomical path length, ensuring the cells have fully repolarized (Fig. 4e). This functional filtering breaks the wavefront's spatial continuity, establishing the asymmetric conduction pathways necessary to initiate and sustain micro-reentrant rotors.

The structural layout of a fibrotic region determines the location and frequency of these source-sink mismatches and conduction blocks. Fragmented and scattered patterns increase the density of micro-expansion zones, leading to wave breaks, while dense macroscopic obstacles alter the local curvature of the front, modifying the effective electri-

Figure 4 – Schematic representation of the micro-reentry mechanism induced by source-sink mismatch. The formation of a sustained spiral relies on two interdependent biophysical conditions. First, a unidirectional block must occur, often precipitated by a severe source-sink mismatch when a wavefront emerges from a narrow structural tunnel into a massive unexcited area (panel b). Second, as the surviving wavefront propagates through an alternative route and returns to the initial site, it can only reenter the pathway if the local cells have fully repolarized (panel e). Consequently, the electrical wavelength (APD × CV) must be shorter than the anatomical length of the reentrant pathway.

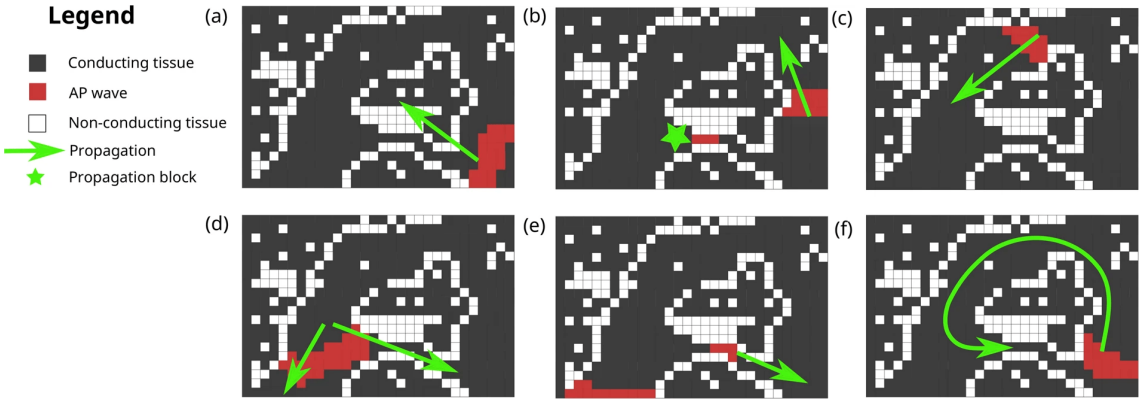

Source: Adapted from Oliveira *et al.* (OLIVEIRA et al., 2018).

cal load and dictating whether a wave will undergo safe redirection or transition into a self-sustaining arrhythmia.

1.4 DYNAMICS OF ROTOR ANCHORING AND SCROLL WAVES

Beyond conduction blocks, understanding how a fragmented wavefront transitions into an arrhythmia requires analysing the dynamics of rotor stabilization. When a wave breaks due to a source-sink mismatch or other functional unidirectional block, the resulting broken ends can either self-terminate at the domain boundaries or curve inward to form rotating spiral waves. In two dimensions, these rotors can become captured or pinned by non-conducting obstacles, a process known as rotor anchoring. The stability of this anchoring depends on the geometry of the barrier; macroscopic boundaries provide stable columns that absorb the high-curvature tip of the spiral, fixing its rotation frequency and preventing the complex meandering drift characteristic of free rotors (as illustrated by the diverse tip trajectories in Fig. 5a-c) (FENTON et al., 2002; CHERRY; FENTON, 2008).

When expanding this phenomenon into three-dimensional tissues, the rotation axis of the spiral wave forms a continuous linear trajectory known as a scroll wave filament. These filaments possess an intrinsic mechanical property called filament tension, which forces them to minimize their length and curvature (FENTON; KARMA, 1998; CHERRY; FENTON, 2008; MAJUMDER; NAYAK; PANDIT, 2011; BIKTASHEV;

HOLDEN; ZHANG, 1994). If unanchored, or driven by specific tissue heterogeneities and negative tension, these filaments can undergo severe contortions, continually elongating and breaking into multiple new filaments through collisions (Fig. 5d-f). In a voxel-discretized disordered medium, a filament is subjected to continuous contortions that accumulate energy, often leading to instability and self-termination. Consequently, investigating how histology-inspired 3D fibrosis configurations provide spatial surfaces to stabilize these scroll waves is a key requirement to unraveling the volumetric nature of propagation reentries.

Figure 5 – Dynamics of 2D spiral wave tips and 3D scroll wave filaments. (a-c) In two-dimensional media, the tip of a free spiral wave can exhibit highly complex meandering trajectories (e.g., circular, epicycloidal, hypermeandering, or linear drift). Anchoring these wandering tips to macroscopic structural barriers stabilizes their rotation. (d-f) In 3D tissue, the rotation axis of the spiral forms a scroll wave filament. Under specific dynamic conditions, these filaments continually elongate, contort, and break through collisions with tissue boundaries or other filaments.

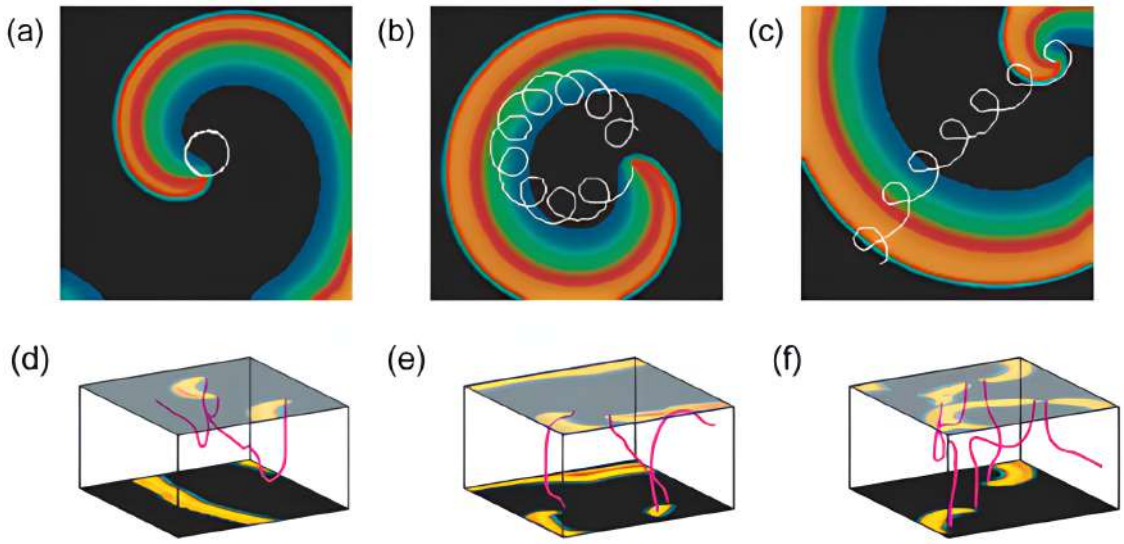

Source: Adapted from Cherry and Fenton (CHERRY; FENTON, 2008).

1.5 BRIEF LITERATURE REVIEW

The arrhythmogenic nature of cardiac fibrosis has been extensively documented in clinical and experimental settings. Seminal histological studies, such as the observations of zigzag conduction in infarcted human hearts (BAKKER et al., 1993), established early on that collagen deposition is not homogeneous. Over time, comprehensive histological analyses categorized fibrosis into distinct micro-architectures — namely *compact*, *diffuse*, *interstitial*, and *patchy* — each posing unique perils to tissue electrophysiology and significantly correlating with the incidence of ventricular tachyarrhythmias (NGUYEN; QU; WEISS, 2014; JONG et al., 2011; DISERTORI; MASÈ; RAVELLI, 2017; GLASHAN et al., 2018).

Despite this histological clarity, assessing these micro-structures *in vivo* remains a profound clinical challenge. Current non-invasive imaging modalities, such as Late Gadolinium Enhancement Cardiac Magnetic Resonance (LGE-CMR), lack the spatial resolution required to capture microscopic collagen distribution, often blurring fine fibrotic networks into generalized gray zones (HASSAN; BARRETT; CROSSMAN, 2020; RAVASSA et al., 2023). Consequently, computational modeling has emerged as an indispensable scientific tool to bridge the gap between microscopic structural remodeling and macroscopic whole-heart arrhythmogenesis (CLAYTON et al., 2011; TRAYANOVA; CHANG, 2016).

The computational representation of cardiac fibrosis has evolved significantly over the past decades. Early *in silico* investigations approximated fibrosis by randomly removing conductive elements from the computational grid, essentially treating fibrosis as uncorrelated white noise. These foundational studies demonstrated that macroscopic wave propagation, APD, and arrhythmia susceptibility are significantly dependent on the total myofibroblast density (TUSSCHER; PANFILOV, 2007; MORITA et al., 2009; MCDOWELL et al., 2011). However, as models matured, it became evident that total density is only one part of the equation.

Recent investigations have proven that the specific architecture of the obstacle field is just as critical as the collagen density itself. Studies by Balaban *et al.* (BALABAN et al., 2018) and Myklebust *et al.* (MYKLEBUST; MALECKAR; AREVALO, 2024) demonstrated that the choice of fibrosis modeling technique directly alters the morphology of ventricular arrhythmias in non-ischemic cardiomyopathies. The spatial distribution of non-conducting cells governs the self-organization of conducting pathways (KUDRYASHOVA et al., 2019), systematically defining how waves fractionate in cardiac tissue (MASÈ et al., 2024) and dictating the severe anisotropic conduction delays observed in histologically detailed electroanatomical models (CAMPOS et al., 2013).

To systematically capture these effects, recent computational efforts have focused on generating explicitly textured domains. Dokuchaev, Nezlobinsky, and Panfilov (DOKUCHAEV; PANFILOV; SOLOVYOVA, 2020; NEZLOBINSKY; SOLOVYOVA; PANFILOV, 2020) mapped the effects of anisotropic, diffuse, and patchy textures on wave propagation across both 2D and 3D simplified models. Furthermore, data-driven approaches are increasingly being used to extract generative texture rules directly from human histological slices (OKENOV et al., 2025).

Despite these advances, embedding controlled, spatially correlated, and scalable micro-architectures into high-performance biophysical simulations remains an active frontier. Recognizing the limitations of uncorrelated random distributions, Lawson *et al.* (LAWSON et al., 2020; LAWSON et al., 2024) pioneered the use of Perlin noise to generate physiologically realistic and spatially autocorrelated fibrotic fields.

1.6 OBJECTIVES

The general objective of this work is to develop, implement, and evaluate an integrated computational framework to investigate and quantify how spatially autocorrelated fibrotic micro-architectures modulate electrical wave propagation and the probability of sustained ventricular reentry under acute hypoxic conditions.

To achieve this general goal, the following specific objectives were established:

- **Quantify morphological and topological metrics:** Systematically characterize the fibrotic substrates across both 2D and 3D domains using geometric descriptors (spatial autocorrelation (GETIS, 2009), aspect ratio, fractal dimension (FALCONER, 2013; IANNACCONE; KHOKHA, 1996), mean cluster size (STAUFFER; AHARONY, 2018; SAHIMI; HUNT, 2021)) and Betti numbers (EDELSBRUNNER; HARER, 2010).
- **Conduct wave percolation analyses:** Evaluate the structural phase transitions of the generated networks (STAUFFER; AHARONY, 2018; SAHIMI; HUNT, 2021), determining critical percolation thresholds, transition widths, and topological conduction efficiencies.
- **Evaluate multi-scenario arrhythmogenic interaction between the electrical propagation wave and the fibrosis:** Map the dynamic mechanisms of wavefront fractionation, rotor anchoring, and scroll wave stabilization across three distinct experimental configurations: 2D homogeneous slabs, 2D localized lesions with border zone, and 3D volumetric tissues.
- **Construct non-linear mathematical risk profiles:** Develop a statistical pipeline using Firth's bias-reduced penalized logistic regression (FIRTH, 1993) and Generalized Additive Models (GAM) (HASTIE; TIBSHIRANI, 1986; WOOD, 2017) to translate discrete simulation outcomes into continuous risk curves, pinpointing peak vulnerability densities and defining relative risk odds ratios among the diverse fibrosis phenotypes.

1.7 SCIENTIFIC CONTRIBUTIONS

The computational frameworks, topological pipelines, and biophysical findings developed throughout this Master's degree represent multiple scientific contributions. These works encompass manuscripts prepared for journals, as well as studies presented at major international and national conferences in the fields of biomedical engineering and computational science.

The scientific production derived directly from, or closely related to, the development of this research project includes:

- Couto, Guilherme M., *et al.* "Modulation of Cardiac Arrhythmogenesis by Spatially Correlated Fibrosis." Manuscript in preparation for submission to *Chaos: An Interdisciplinary Journal of Nonlinear Science*

- Couto, Guilherme M., Joventido O. Campos, and Rodrigo W. dos Santos. "A Framework to Assess the Influence of Different Cardiac Fibrosis Phenotypes and Border Zone on Arrhythmogenesis." *Simpósio Brasileiro de Computação Aplicada à Saúde (SBCAS)*. SBC, 2026.

- Couto, Guilherme Martins, *et al.* "Evaluating the Influence of Different Realistic Fibrosis Patterns on Cardiac Arrhythmias using Computational Models." *Computing in Cardiology 52*. 2025.

- de Jesus Soares, Thaís, *et al.* "Uncovering Arrhythmic Substrate in a Heart Failure Patient Using Digital Twins." *Computing in Cardiology 52*. 2025.

- Pereira, J. P. B., *et al.* "Computational Modeling of Sources of Cardiac Arrhythmia to Determine Their Effect on Generating Arrhythmias: Ischemia, Diffuse Fibrosis, and Long QT Syndrome." *Brazilian Congress on Biomedical Engineering*. Cham: Springer Nature Switzerland, 2024.

Additionally, implementations regarding high-performance computing solvers, numerical splitting methods, and GPU-driven parallel acceleration techniques developed during the optimization of our numerical solver led to the following works:

- Couto, Guilherme M., *et al.* "High-Performance Cardiac Electrophysiology Simulation with SSI-ADI: Second-Order Accuracy and GPU-Driven Acceleration." *Computing in Cardiology 52*. 2025.

- Couto, Guilherme Martins, *et al.* "Accelerating the Simulations of Cardiac Arrhythmia with a Second-Order Numerical Method and High-Performance Computing." *International Conference on Computational Science and Its Applications*. Cham: Springer Nature Switzerland, 2023.

- Couto, Guilherme M., Noemi Z. Monteiro, and Rodrigo W. dos Santos. "Accelerating simulations of cardiac arrhythmias through robust numerical techniques and parallel computing." *Simpósio Brasileiro de Computação Aplicada à Saúde (SBCAS)*. SBC, 2023.

2 FIBROSIS GENERATION PIPELINE

Characterizing the topological architecture of non-conducting obstacles in cardiac tissue remains a profound challenge in computational modeling (MYKLEBUST; MALECKAR; AREVALO, 2024; LAWSON et al., 2024; OKENOV et al., 2025). Many *in silico* studies resort to simplified representations of fibrosis, employing white noise (TUSSCHER; PANFILOV, 2007; ALONSO; SANTOS; BÄR, 2016; LAWSON et al., 2020; PEREIRA et al., 2024; SOARES et al., 2025). While easy to generate, these approaches may fail to reproduce the specific heterogeneities, spatial autocorrelation, and distinct anisotropy observed in biological tissues (SAHIMI, 1994; CLAYTON et al., 2011). Recognizing these limitations, recent efforts have explicitly modeled oriented fibrotic clefts, leveraged high-resolution imaging, and applied spatially correlated stochastic processes to construct more structurally coherent fibrosis fields (NEZLOBINSKY; SOLOVYOVA; PANFILOV, 2020; HEIKHMAKHTIAR; TEKLE; LIM, 2021; NEZLOBINSKY; OKENOV; PANFILOV, 2021; GIARDINI et al., 2025). To overcome the constraints of uncorrelated uniform probability distribution and construct controlled topological substrates for electrophysiological simulations, we restructured and expanded a procedural generation pipeline based on Perlin noise developed by Lawson *et al.* (LAWSON et al., 2024).

2.1 PROCEDURAL SYNTHESIS OF CORRELATED TEXTURES

Originally developed to synthesize natural textures in computer graphics, Perlin noise is a band-limited gradient noise (PERLIN, 1985). It operates by assigning pseudo-random gradient vectors to nodes on a regular spatial grid and computing a smooth, interpolated value for any point based on the dot products between the gradients and the distance vectors to that point (Fig. 6). Unlike pure white noise, which produces indistinct scatter, Perlin noise generates continuous and auto-correlated features of controllable size.

To introduce the finer morphological details characteristic of biological obstacles, a multi-octave approach is utilized, where several scaled, higher-frequency noise fields are successively superimposed onto a base pattern. Given that the value of a Perlin noise field at point $\mathbf{x}$ is denoted by $\mathcal{P}(\mathbf{x})$, the refined noise fields $\mathcal{P}(\mathbf{x}, \gamma)$ are obtained by

$$\mathcal{P}(\mathbf{x}, \gamma) = \frac{1}{2} + \frac{\sqrt{2}(1-\gamma)}{2(1-\gamma^{N_o})} \sum_{i=1}^{N_o} \gamma^{i-1} \mathcal{P}_i(2^{i-1}\mathbf{x} + \delta\mathbf{x}_i), \tag{2.1}$$

where $0 < \gamma \leq 1$ defines the roughness of the noise field by down-weighting higher-frequency components, N_o is the number of combined octaves (in this study, $N_o = 4$), and the subscript i indicates that each noise field is generated using a distinct random seed to perturb the vectors, avoiding structural coincidences.

In two dimensions, an anisotropic noise field $\mathcal{N}$ is obtained by transforming an

Figure 6 – Schematic representation of the 2D Perlin noise generation process. (Left) A regular spatial grid is initialized with pseudo-random gradient vectors (green arrows) at each node. (Right) To determine the noise value at a specific domain point (blue circle), distance vectors (orange arrows) are computed from the surrounding grid nodes to the target point. The dot products (red squares) between these distance and gradient vectors are evaluated and smoothly interpolated to yield the final continuous noise value.

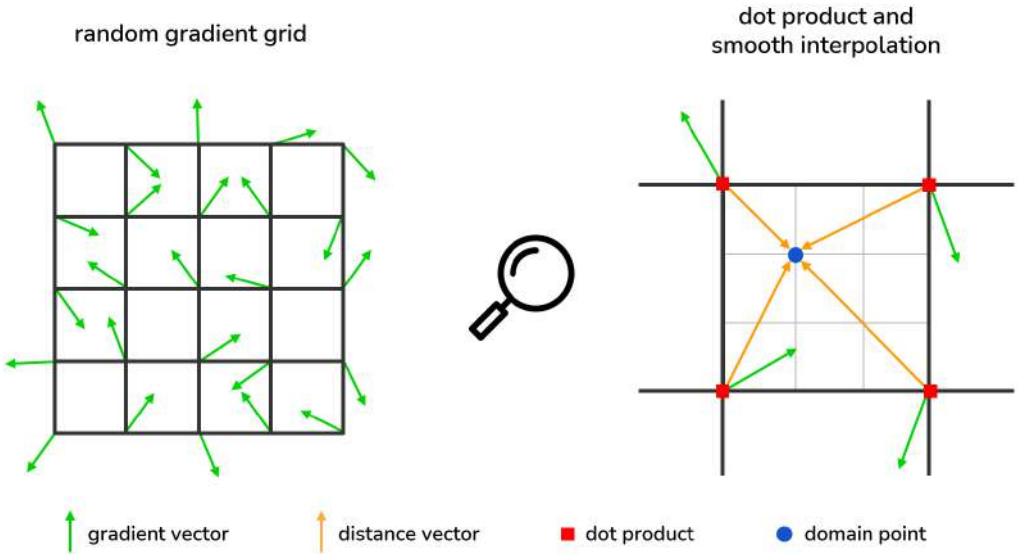

Source: Elaborated by the author (2026).

evaluation point $\mathbf{x}$ (expressed as a row vector) using

$$\mathcal{N}(\mathbf{x}) = \mathcal{P}\left(\frac{1}{l}\mathbf{x}\mathbf{R}_\phi^T\mathbf{A}_R, \gamma\right),$$

$$\mathbf{R}_\phi = \begin{pmatrix} \cos\phi & \sin\phi \\ -\sin\phi & \cos\phi \end{pmatrix}, \tag{2.2}$$

$$\mathbf{A}_R = \begin{pmatrix} 1/\sqrt{R} & 0 \\ 0 & \sqrt{R} \end{pmatrix},$$

where l represents the radius of the noise features before anisotropic stretching, R is the anisotropy ratio, and ϕ is the primary orientation direction.

For three-dimensional domains, these spatial transformations (Eqs. (2.2)) must be extended. The 2D rotation is expanded into a 3D matrix $\mathbf{R}_{\phi,\theta}$, governed by the primary fibre angle ϕ and the transmural angle θ. Correspondingly, the scaling matrix $\mathbf{A}_R$ is upgraded to a 3×3 representation that incorporates K, an additional parameter specifying the anisotropy between the fibre direction and the new third dimension. These operators

are given by

$$\mathbf{R}_{\phi,\theta} = \begin{pmatrix} \cos\phi\cos\theta & \sin\phi & -\cos\phi\sin\theta \\ -\cos\phi\sin\theta & \cos\phi & \sin\phi\sin\theta \\ \sin\theta & 0 & \cos\theta \end{pmatrix}, \tag{2.3}$$

$$\mathbf{A}_R = \begin{pmatrix} K^{-\frac{1}{3}}R^{-\frac{2}{3}} & 0 & 0 \\ 0 & K^{-\frac{1}{3}}R^{\frac{1}{3}} & 0 \\ 0 & 0 & K^{\frac{2}{3}}R^{\frac{1}{3}} \end{pmatrix},$$

more information about these operators are going to be described subsequently in this Section.

The framework developed by Lawson *et al.* (LAWSON et al., 2024), constructs the fundamental architecture through the weighted combination $\mathcal{G}$ of three distinct Perlin noise fields ($\mathcal{N}_b$, $\mathcal{N}_d$, and $\mathcal{F}$), as follows:

$$\mathcal{G}(\mathbf{x}) = \mathcal{N}_b(\mathbf{x})\left((1-f) + f\mathcal{F}(\mathbf{x})\right) + d\mathcal{N}_d(\mathbf{x}), \tag{2.4}$$

where f and d represent fibrosity and patchiness weights, respectively. The three noise fields serve distinct structural roles: $\mathcal{N}_b$ is a base field that defines the primary topology of obstacle clusters, $\mathcal{N}_d$ is a density variation field that introduces large-scale spatial heterogeneity, and $\mathcal{F}$ is a fibre field that make long deposits align with fibres. To achieve the final binary mask of the fibrotic pattern with the desired density, a threshold is applied to the combined and weighted field $\mathcal{G}$, as illustrated in Fig. 7.

Figure 7 – Overview of the procedural fibrosis pattern generation. The image demonstrates how the binarized fibrosis pattern is constructed from the weighted sum (Combined Field $\mathcal{G}$) of multiple octaves Perlin noise fields (Base Noise $\mathcal{N}_b$, Density Variation $\mathcal{N}_d$, and Fibre Selection $\mathcal{F}$), each with varying frequencies and amplitudes.

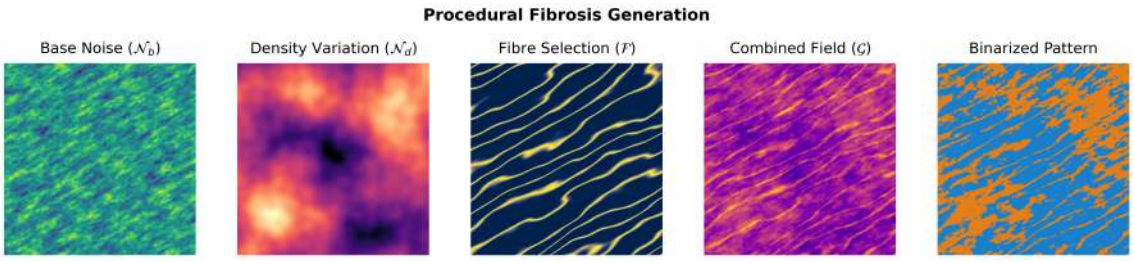

Source: Elaborated by the author (2026).

The primary topology is established by a base noise field $\mathcal{N}_b$, which follows Eq. (2.2) with base feature size l_b and base roughness γ_b. In 3D, to maintain the correct volumetric proportions and characteristic lengths of the features during the expansion, l_b must be

geometrically scaled according to $l_{b(3D)} = l_{b(2D)} K^{-1/3} R^{-1/6}$ (LAWSON et al., 2024). In our volumetric scenarios, we assumed an isotropic transverse plane by setting $K = 1$, ensuring uniform separation across the non-longitudinal axes.

The structure is further modulated by a density variation field $\mathcal{N}_d$ consisting of isotropic features without significant roughness ($\gamma_d = 0.5$) that introduces spatial macroscopic heterogeneity, which is given by:

$$\mathcal{N}_d(\mathbf{x}) = \mathcal{P}\left(\frac{1}{l_d}\mathbf{x}, \gamma_d\right). \tag{2.5}$$

Finally, a fibre selection field $\mathcal{F}$ aligns the generated patterns with the local tissue anisotropy, as established by:

$$\begin{aligned} \mathcal{F}(\mathbf{x}) &= \left(\frac{1}{2} + \frac{1}{2}\cos\left(\frac{2\pi}{L}\mathbf{e}_2^T \mathbf{R}_\phi \mathbf{x} + \Phi \mathcal{N}_f(\mathbf{x})\right)\right)^s, \\ \mathcal{N}_f(\mathbf{x}) &= \mathcal{P}\left(\begin{bmatrix} \beta_\parallel & 0 \\ 0 & \beta_\perp / L \end{bmatrix} \mathbf{R}_\phi \mathbf{x}, \gamma_f\right), \end{aligned} \tag{2.6}$$

where L is the fibre separation, $\mathbf{e}_2$ is the standard basis vector, $\Phi = 10\pi$ is the strength of phase modulation, $s = 15$ is a sharpening factor, $\beta_\parallel = \beta_\perp = 0.25$ are information about the spatial scale of fibres' dissimilarities, and $\gamma_f = 0.5$ is the phase modulation roughness.

To create regularly spaced fibres running along a single direction in a 3D volume, the field relies on a product of cosine functions varying along the two perpendicular directions, modulated by fields $\mathcal{Z}_j(\mathbf{x})$, as defined in Eqs. (2.7):

$$\begin{aligned} \mathcal{F}_{3D}(\mathbf{x}) &= \left(\frac{1}{2} + \frac{1}{2}\prod_{j=1}^{2}\cos\left(\frac{2\pi}{L_j}\mathbf{e}_{j+1}^T \mathbf{R}_{\phi,\theta}\mathbf{x} + \Phi \mathcal{Z}_j(\mathbf{x})\right)\right)^s, \\ \mathcal{Z}_j(\mathbf{x}) &= \mathcal{P}\left(\begin{bmatrix} \beta_\parallel & 0 & 0 \\ 0 & \beta_\perp / L_1 & 0 \\ 0 & 0 & \beta_\perp / L_2 \end{bmatrix} \mathbf{x}, \gamma_f\right), \end{aligned} \tag{2.7}$$

where L_j defines the fibre separation distances for those directions (in our transverse setting, $L_1 = L_2 = L$).

Our pipeline aims to reproduce four distinct fibrosis phenotypes based on histological taxonomy (Fig. 8): *compact* (dense contiguous blocks), *diffuse* (scattered short segments), *interstitial* (reticular mesh), and *patchy* (irregular contiguous clusters). The base parameter values defining the morphology of each phenotype are summarized in Table 1. While these parameters were originally calibrated by Lawson *et al.* (LAWSON et al., 2024) for 2D histological slices of ventricular epicardium (as presented in the study of Kawara *et al.* (KAWARA et al., 2001)), modeling 3D samples required mapping these properties

into an equivalent domain. To achieve this without altering the intrinsic signature of the phenotypes, we followed the 3D expansion methodology detailed by Lawson *et al.* (LAWSON et al., 2024). Specifically, we set the longitudinal and transverse fibre separations and alignments to be equal ($d_y = d_z$ and $R_y = R_z$). Moreover, for consistency across the ensemble generations, the two angles of $\mathbf{R}_{\phi,\theta}$ were maintained equal ($\phi = \theta$).

Figure 8 – Representative patterns of the generated fibrosis phenotypes. Orange pixels represent non-conductive collagenous obstacles, while blue pixels represent the myocardial tissue. We synthesize four distinct histology-inspired spatial correlated textures: *compact*, *diffuse*, *interstitial*, and *patchy*. The displayed densities correspond to the specific realizations shown.

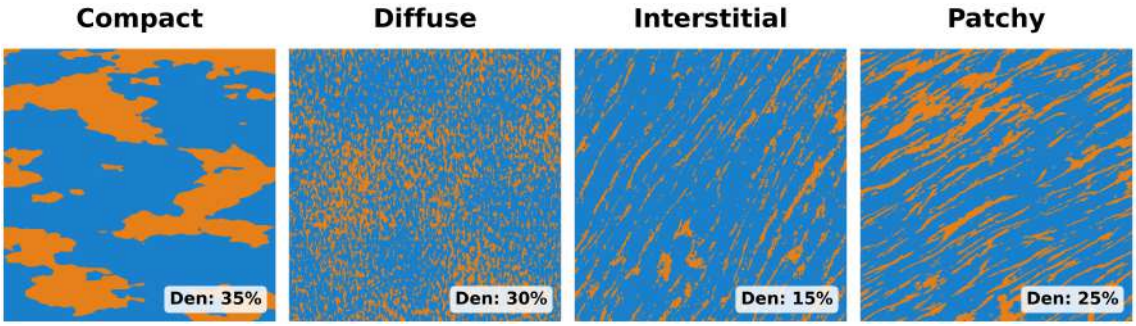

Source: Elaborated by the author (2026).

Table 1 – Generator parameters used for the creation of 2D fibrosis phenotypes derived from the histologically calibrated sets by Lawson *et al.* (LAWSON et al., 2024). Parameters are grouped by the specific noise field they modulate.

Parameter (Symbol)	Compact	Diffuse	Interstitial	Patchy
Base Noise Field				
Alignment (R)	2.47	2.17	1.89	2.50
Feature Size (l_b)	0.96	0.07	0.24	0.32
Roughness Base (γ_b)	0.59	0.44	0.96	0.78
Density Variation Field				
Patch Size (l_d)	2.03	1.22	4.67	2.10
Fibre Selection Field				
Fibre Orientation (ϕ)	Varied	Varied	Varied	Varied
Fibre Separation (L)	-	-	0.31	0.31
Weighted Combination				
Fibrosity (f)	0.00	0.00	0.30	0.38
Patchiness (d)	0.44	0.49	0.32	0.42

Source: Elaborated by the author (2026).

2.2 DENSITY SCALING AND THE COMPOSITION ALGORITHM

To systematically evaluate the fibrosis, it was necessary to vary the obstacle density across a broad spectrum (5% to 95%). During preliminary evaluations, we observed that achieving high densities by simply lowering the Perlin noise generation threshold — the original method, which for clarity we termed *single-pass* mode — compromised the topological signature of fractionated patterns. For instance, single-pass density scaling caused the features of *interstitial* fibrosis to artificially inflate and merge into solid contiguous blocks, losing their reticular nature. A similar behaviour, but with its own particularities, occurred with *diffuse* and *patchy*. Visual comparison of these structural artifacts is provided in Fig. 9.

Figure 9 – Comparison of generation modes in a 2D domain at a high target density (60%). In the single-pass mode (top row), fractionated patterns like *interstitial* lose their fine reticular clefts, merging into thick, blocky aggregates. The composition mode (bottom row) preserves the fine structural characteristics.

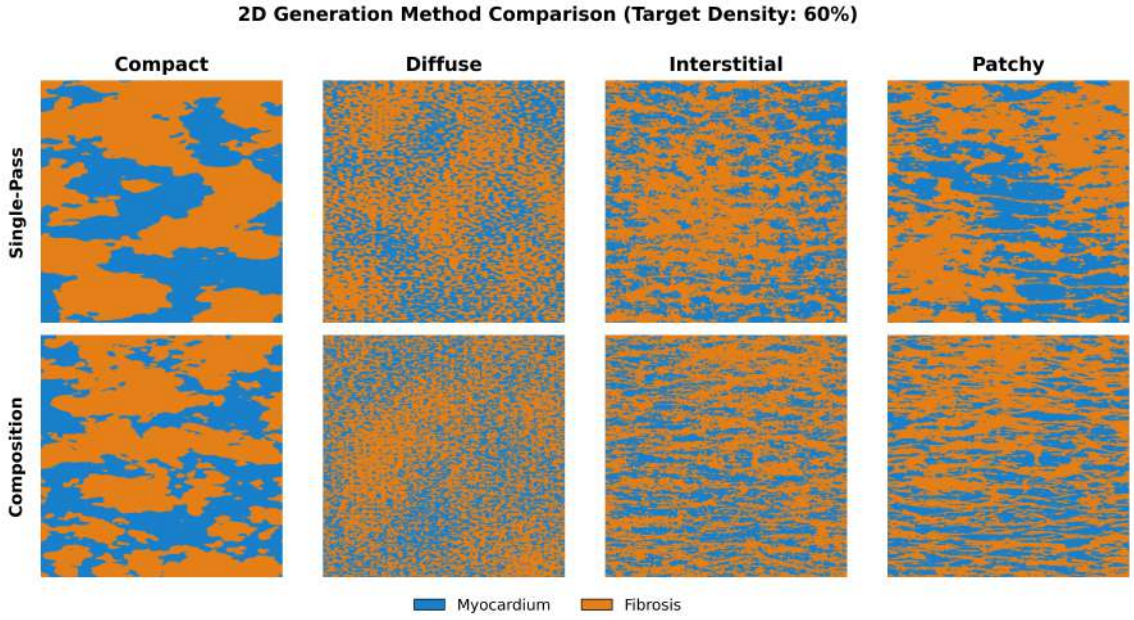

Source: Elaborated by the author (2026).

To preserve the defining spatial autocorrelation of these patterns at elevated densities, we developed an iterative generation method termed *composition* mode. Instead of a single thresholding step in the weighted Perlin noise field, this algorithm generates and superimposes multiple low-density binary masks (typically $\leq 10\%$ density per layer) derived from randomly perturbed seeds as shown in Algorithm 1 (a step-by-step visual breakdown of this layering process is provided in Fig. 10). This approach successfully stacks fine structural features to construct cumulative density without artificially inflating the diameter of individual obstacles. Consequently, the composition mode was employed for *diffuse*, *interstitial*, and *patchy* phenotypes, while the single-pass mode was retained

exclusively for *compact* fibrosis, where the expansion and macroscopic merging of features accurately reflect the growth of a monolithic solid core.

Algorithm 1 Composition Mode

Require: Target Density ρ_{target}, Base Density Step $\rho_{step} \leftarrow 0.10$, Initial Seed S_0

$M_{final} \leftarrow$ ZerosMatrix(DomainSize)
$\rho_{current} \leftarrow 0$
while $\rho_{current} < \rho_{target}$ **do**
    $Seed \leftarrow PerturbSeed(S_0)$
    $\mathcal{G} \leftarrow GeneratePerlinNoise(Seed, Parameters)$
    $\rho_{needed} \leftarrow \min(\rho_{step}, \rho_{target} - \rho_{current})$
    $T \leftarrow FindBisectionThreshold(\mathcal{G}, \rho_{needed})$
    $M_{layer} \leftarrow (\mathcal{G} \geq T)$
    $M_{final} \leftarrow M_{final} \vee M_{layer}$ ▷ Logical OR superposition
    $\rho_{current} \leftarrow CalculateDensity(M_{final})$
end while
return M_{final}

Figure 10 – Step-by-step visualization of the iterative composition algorithm for an *interstitial* phenotype. Multiple low-density masks derived from randomly perturbed seeds are logically superimposed (OR operation). This approach builds up the cumulative target density (from 10.0% in Step 1 to 39.7% in Step 7) while maintaining the fine-grained structural fidelity of the individual elements

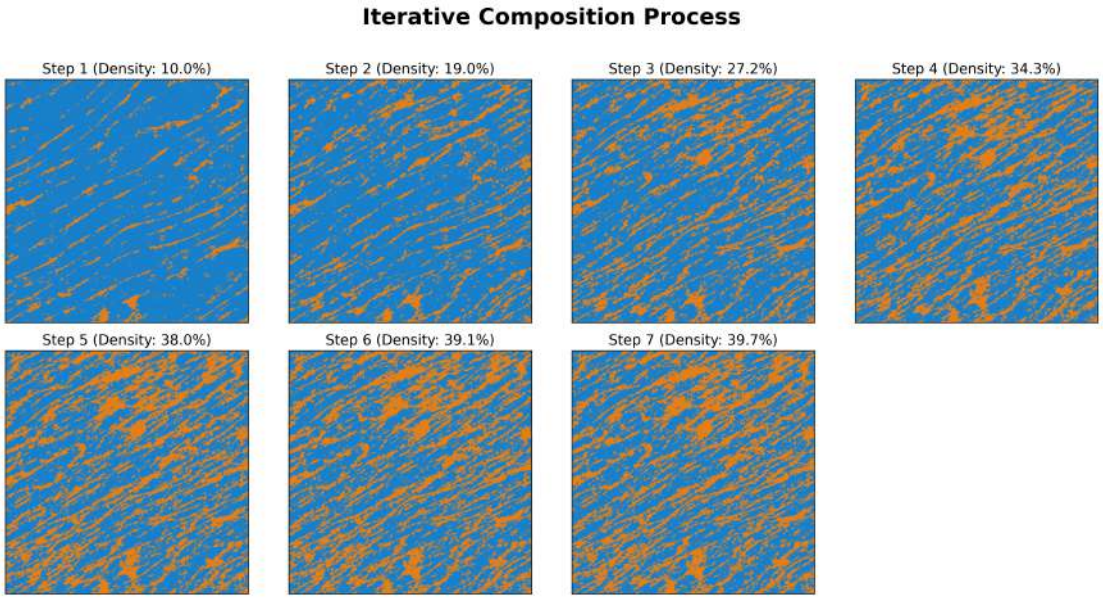

Source: Elaborated by the author (2026).

To provide a baseline against these histology-inspired and spatially correlated patterns, a *uniform* mode was also implemented that bypasses the Perlin engine entirely and assigns obstacles independently at each site with uniform probability, creating a spatially uncorrelated baseline for our comparisons.

2.3 SPATIAL DOMAINS AND BOUNDARY GRADIENTS

To support complex spatial configurations, such as focal lesions with transitional borders, we decoupled the spatial geometry from the textural noise generation (Fig. 11).

From a software engineering and computational modeling perspective, this decoupling of the macro-scale geometric constraints from the micro-scale texture generation represents a highly versatile modular architecture. The spatial domain is defined using binary masks to explicitly delineate a central Fibrotic Core (FC) and the surrounding homogeneous excitable medium. A transitional BZ is then constructed efficiently by applying a Euclidean distance transform to the FC mask, creating concentric layers propagating outward from the core. By separating the spatial masking (which establishes the global anatomical bounds of the lesion) from the underlying continuous Perlin fields, our pipeline guarantees that the definitions of the phenotypes remain completely invariant across different experimental setups. Consequently, a specific textural seed can be evaluated identically within a fully diseased continuous slab or confined within a tortuous focal scar.

Figure 11 – Overview of the modular topological pipeline using a *compact* focal lesion as an example. (A) Spatial masking isolating the FC and BZ layers. (B) Weighted multi-octave Perlin noise field. (C) Adaptive thresholding enforcing an exponential density decay in the BZ. (D) The final binarized fibrosis map.

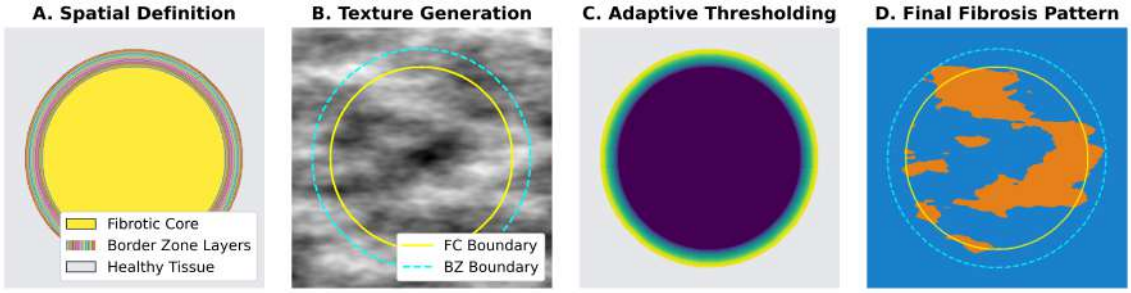

Source: Elaborated by the author (2026).

To accurately model the gradual pathophysiological transition between diseased and healthy tissue (COSTA et al., 2018), a spatial gradient governs the obstacle distribution within that zone. The BZ is geometrically discretized into a set of morphological layers ($l \in \{1, 2, \ldots, L_{total}\}$) with a thickness of exactly one spatial voxel, expanding uniformly outward from the FC (Fig. 11A). By constraining the gradient resolution to the fundamental unit of the tissue mesh, we prevent the creation of artifacts and ensure that the iterative thresholding algorithm remains structurally coherent across the entire transition region.

To ensure rigorous comparative analysis, both the *uniform* baseline and the spatially correlated Perlin patterns were constrained to obey an identical exponential density decay profile. The target obstacle density for a given BZ layer $\rho(l)$ drops exponentially from the

core density ρ_{core}, as given by:

$$\rho(l) = \rho_{core} \exp\left(-3.0 \frac{l}{L_{total}}\right), \tag{2.8}$$

where l is a morphological layer and L_{total} is the total number of BZ layers, as explained in the previous paragraph. The exponential decay profile was motivated by the steady-state solution of a reaction-diffusion system with linear consumption, the same mathematical framework that governs oxygen transport from the microvasculature into ischemic myocardium (GOLDMAN, 2008), ensuring the obstacle density drops to approximately 5% of its core value at the outermost layer without imposing abrupt structural discontinuities. For the continuous Perlin noise fields, a localized bisection algorithm dynamically iterates and identifies the exact threshold $T(l)$ required at each specific layer l so that the resulting binarized output precisely matches the target density $\rho(l)$, so each layer is done separetly. This adaptive thresholding guarantees that any observed electrophysiological divergence between phenotypes arises only from their inherent texture, rather than artifacts of uneven density scaling. On the other hand, for the *uniform* baseline, obstacles are simply scattered at this precise $\rho(l)$ probability per layer.

3 MORPHOLOGICAL AND TOPOLOGICAL CHARACTERIZATION METRICS

Prior to executing the electrophysiological simulations, we conducted a morphological and topological characterization of the synthesized domains. This step is crucial to quantify the structural boundaries that dictate wave propagation, independent of cellular kinetics.

For every unique combination of fibrosis phenotype (*compact*, *diffuse*, *interstitial*, *patchy*, and *uniform*), target density (from 5% to 95% in 5% steps), and fibre orientation (0°, 30°, 60°, and 90° — except for *uniform*, which is topologically insensitive to this variation), we generated an ensemble of 100 distinct random seeds to ensure statistical robustness. Throughout this work, the structural anisotropy angle (ϕ) prescribed to the Perlin noise generator is treated as strictly identical to the longitudinal fibre direction applied to the tissue conductivity tensor during the electrophysiological simulations. By enforcing this match, the directional fibrotic deposits (e.g., *interstitial* and *patchy* patterns) naturally align and run parallel to the myocardial fibres. This combinatorial parameter space yielded a total of 7600 distinct samples for each histology-inspired phenotype (using the parameters specified in Table 1) and 1900 for *uniform*. To accommodate macroscopic reentrant circuits in the subsequent electrophysiological analyses, the structurally generated patterns were geometrically scaled by a factor of 10 (the implications of this scaling are further discussed in Chapter 7). Consequently, the binarized domains were discretized with $\Delta x = 100$ μm, yielding macroscopic physical grids of 4×4 cm for the 2D planar scenarios and $1 \times 1 \times 1$ cm for the 3D volumetric scenarios. Within these spatial grids, the excitable medium (myocardium) and the obstacles (fibrosis) are represented as distinct binary phases: conductive and non-conductive. These samples were subsequently evaluated across three structural domains: cluster morphology, algebraic topology, and percolation theory.

3.1 GEOMETRIC AND MORPHOLOGICAL CLUSTER DESCRIPTORS

To quantitatively evaluate how the physical aggregation and spatial layout of collagenous barriers might be expected to impact wavefront stability, we implemented a structural analysis pipeline based on the geometric properties of the fibrotic phase. The first phase of this characterization relies on connected-component labeling to partition the non-conducting obstacles into discrete structural entities. To replicate the pathways of electrical propagation around micro-obstacles, all clustering operations were constrained to Moore connectivity — utilizing an 8-connected neighborhood model in 2D and a 26-connected voxel neighborhood model in 3D (GONZALEZ; WOODS, 2018).

3.1.1 Normalized Mean Cluster Size ($\hat{S}$)

A pivotal parameter derived from statistical mechanics and percolation theory is the Mean Cluster Size, which acts as a proxy for the wave-scattering potential of the substrate (STAUFFER; AHARONY, 2018; SAHIMI; HUNT, 2021; SAHIMI, 1994). In a heterogeneous excitable medium, the collision of a wavefront with scattered non-conducting obstacles causes localized wave fractionation. The severity of this phenomenon depends strictly on the size distribution of these obstacles. Mathematically, the average size of a finite cluster chosen by selecting a random fibrotic voxel is governed by the ratio of the second moment to the first moment of the cluster size distribution (STAUFFER; AHARONY, 2018; SAHIMI, 1994). To achieve strict mathematical comparability across distinct grid sizes (N) and spatial dimensions, we define the Normalized Mean Cluster Size ($\hat{S}$) as illustrated in Eq. (3.1):

$$\hat{S} = \frac{1}{N} \frac{\sum_k s_k^2}{\sum_k s_k}, \tag{3.1}$$

where s_k is the total volume (number of elements) comprising the finite cluster k. Crucially, to prevent massive scaling cluster bias, the largest fibrotic cluster is dynamically identified and excluded from the summation.

3.1.2 Mean Aspect Ratio (AR)

While $\hat{S}$ dictates the mass of the barriers, their spatial elongation is captured via the mean Aspect Ratio (AR). Histologically, patterns such as *interstitial* and *patchy* fibrosis are characterized by extended collagen septa that run parallel to myocardial fibres, severely altering transverse conduction velocities. To formalize this elongation without incurring prohibitive computational costs, we compute the bounding box dimensions (height h_k, width w_k, and depth d_k for volumetric domains) for each individual cluster k. The global aspect ratio is formulated as an area- or volume-weighted average (Eq. (3.2)) to ensure that dominant structural strands dictate the metric over tiny elements:

$$AR = \frac{\sum_k s_k \left(\frac{\max(h_k, w_k, d_k)}{\min(h_k, w_k, d_k)} \right)}{\sum_k s_k}. \tag{3.2}$$

3.2 SPATIAL CORRELATION AND COMPLEX STRUCTURAL SCALING

3.2.1 Moran's I Spatial Autocorrelation

To establish a mathematically rigorous division between the uncorrelated white noise baseline and the spatially structured Perlin noise configurations, we computed global spatial autocorrelation via Moran's I index (MORAN, 1950; GETIS, 2009). While standard descriptive metrics quantify the global volume of a remodeling tissue, they are fundamentally blind to spatial dependency. Moran's I isolates this dependency by

evaluating the spatial co-variance of the binary grid points relative to a localized adjacency matrix w_{ij}, formulated as follows:

$$I = \frac{N}{W} \frac{\sum_i \sum_j w_{ij}(x_i - \bar{x})(x_j - \bar{x})}{\sum_i (x_i - \bar{x})^2}, \tag{3.3}$$

where $x_i \in \{0, 1\}$ represents the tissue state (myocardium or fibrosis) at voxel i, $\bar{x}$ is the mean global obstacle density, and $W = \sum_i \sum_j w_{ij}$ is the sum of the spatial weights. To achieve complete parity with the physical dimensions calibrated from histological human slices by Lawson *et al.* (LAWSON et al., 2024), we defined the adjacency matrix w_{ij} using a strict inverse Euclidean distance formulation restricted within a local Chebyshev radius of 2. For any pair of elements i and j separated by a distance d_{ij}, the weights are assigned algebraically via:

$$w_{ij} = \begin{cases} d_{ij}^{-1} & \text{if } 0 < d_{ij} \leq \sqrt{8} \\ 0 & \text{otherwise.} \end{cases}$$

In a 3D volumetric matrix, this logic naturally expands into a $5 \times 5 \times 5$ isotropic distance stencil centred on each voxel (LAWSON et al., 2024). A Moran's I value of approximately zero indicates complete spatial randomness (white noise), where the probability of any given site being fibrotic is independent of its neighbors. Conversely, values approaching $+1$ mathematically validate the presence of extended, continuous structural features where nearby cells share identical states, providing a density-invariant signature for structural tissue categorization. These spatial distribution regimes, ranging from perfect chessboard dispersion to highly clustered domains, is conceptually illustrated in Fig. 12 (TSUI et al., 2022).

3.2.2 Fractal Dimension (D_f)

Finally, to characterize the space-filling complexity, roughness, and multi-scale self-similarity of these architectures, we evaluate the Fractal Dimension (D_f) (FALCONER, 2013; IANNACCONE; KHOKHA, 1996). In the clinical setting, fractal analysis of LGE-CMR has emerged as an independent predictor of ventricular fibrillation, as high spatial complexity correlates with erratic wave meandering (CAPTUR et al., 2017; XIE et al., 2024). Computationally, we resolve D_f utilizing a standard box-counting scheme (LIEBOVITCH; TOTH, 1989). The binarized matrix is systematically partitioned by a sequence of regular grids composed of boxes with side lengths ϵ. Let $N(\epsilon)$ represent the total number of boxes that contain at least one non-conductive element at a given scale ϵ. The fractal dimension is then approximated via the limiting power-law relationship defined in Eq. (3.4) (FALCONER, 2013):

$$D_f = \lim_{\epsilon \to 0} \frac{\log N(\epsilon)}{\log(1/\epsilon)}. \tag{3.4}$$

Figure 12 – Schematic distribution regimes of Moran's I spatial autocorrelation. The figure illustrates how the index shifts from negative spatial autocorrelation (dispersion/chessboard) to positive spatial autocorrelation (clustering/feature aggregation). The parameter $E(I)$ represents the mathematically expected value for a completely random pattern with no spatial autocorrelation.

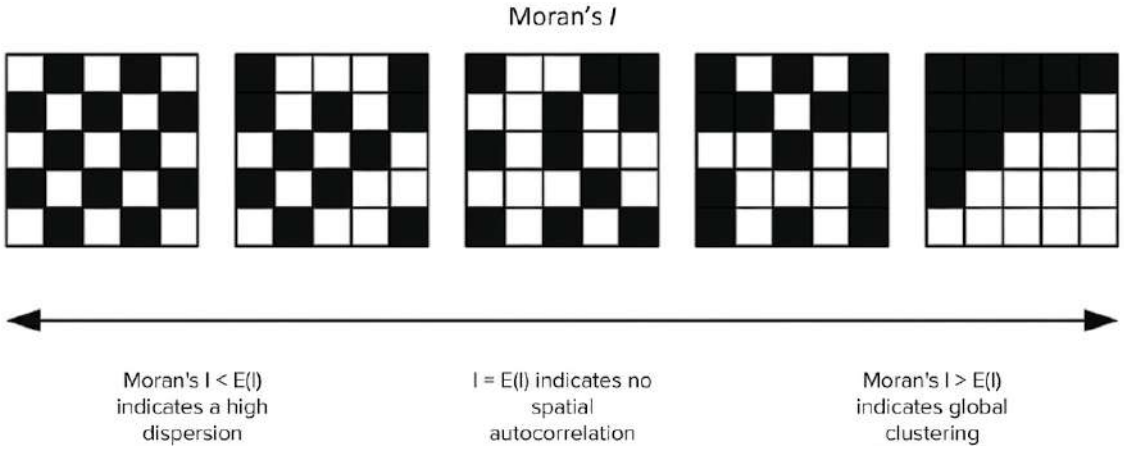

Source: Adapted from Tsui *et al.* (TSUI et al., 2022).

In practice, because our simulated domains are discrete spatial grids, this theoretical limit cannot be evaluated to an infinitely small point. Instead, the box size ϵ is iteratively evaluated across discrete macroscopic scales. The fractal dimension is then computationally extracted as the slope of the linear least-squares regression line fitted to the log-log plot of $N(\epsilon)$ versus $1/\epsilon$. In our computational meshes, D_f serves as an early indicator of wave behaviour: media approaching the upper Euclidean limits ($D_f \to 2$ in 2D; $D_f \to 3$ in 3D) introduce ubiquitous microscopic heterogeneities that favor continuous wave fractionation, whereas lower fractal dimensions signify monolithic blocks that preserve large conduction corridors.

3.3 ALGEBRAIC TOPOLOGY AND NETWORK PERCOLATION ANALYSIS

3.3.1 Homology Groups and Betti Numbers (β_n)

While Moran's I addresses spatial clustering, the global connectedness of the surviving excitable pathways is characterized using computational algebraic topology (EDELSBRUNNER; HARER, 2010). By treating the conducting myocardial medium as a finite cubical complex — where individual pixels or voxels represent elementary cells bonded via shared faces, edges, and vertices — we computed the homology groups and extracted the Betti numbers (β_n) to serve as exact topological invariants of the substrate (EDELSBRUNNER; HARER, 2010).

In the context of cardiac tissue electrophysiology, these topological invariants provide a direct physical interpretation of the structural mechanisms responsible for

conduction block and rotor stabilization, as geometrically mapped through classic canonical shapes in Fig. 13:

- β_0 quantifies the zero-dimensional homology, which counts the number of structurally isolated myocardial components. From an electrophysiological standpoint, a high β_0 translates to extreme electrical fragmentation; these isolated healthy clusters, though metabolically viable, are physically cut off from the main wavefront.
- β_1 quantifies the one-dimensional homology, which explicitly counts the number of independent 1D topological loops. Biophysically, each β_1 loop represents a closed conductive pathway that completely encircles a localized fibrotic obstacle block. These loops form the exact anatomical substrate required to anchor reentrant circuits, allowing a wavefront to continuously circulate around the non-conducting core without encountering refractory tissue.
- β_2 quantifies the two-dimensional homology, evaluated strictly within 3D volumetric domains, which counts the number of completely enclosed internal voids. In electrophysiology, β_2 represents a myocardial shell that fully encapsulates a fibrotic pocket, acting as a complex structural feature that can alter the three-dimensional scroll wave.

Figure 13 – Geometric representation of Betti numbers across standard shapes. The classical notation b_n corresponds directly to the topological invariants β_n, where b_0 counts separate connected pieces, b_1 maps independent circular tunnels or loops, and b_2 identifies completely enclosed three-dimensional voids.

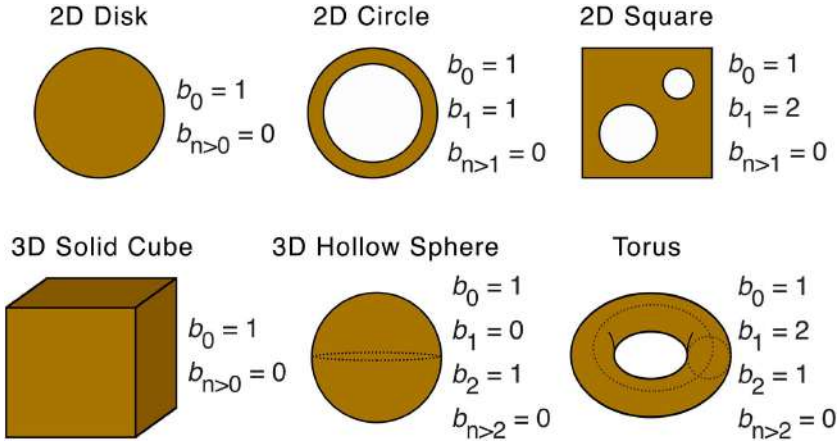

Source: Adapted from Stenseke (STENSEKE, 2021).

3.3.2 Structural Percolation Thresholds (p_c, p_{tw})

The critical transition where a continuous, well-coupled myocardial syncytium degrades into a non-conducting, highly fragmented tissue substrate is fundamentally governed by percolation theory (STAUFFER; AHARONY, 2018; SAHIMI; HUNT, 2021; SAHIMI, 1994). To evaluate this phase transition independently of cellular ionic kinetics, the binarized tissue grid is modeled as an unweighted graph where conductive myocardial voxels act as vertices and their von Neumann neighborhood represents valid edges. To determine if a specific realization percolates, we implemented a graph-traversal routine based on the Breadth-First Search (BFS) algorithm (CORMEN et al., 2022). The search initializes by pushing all conductive nodes located along the absolute left boundary into a first-in first-out queue, and the algorithm systematically explores the network layer by layer. If the exploration successfully activates at least one node on the opposite right boundary, the path is continuous, and the sample is logged as a conducting medium; otherwise, it is logged as non-conductive.

By evaluating an ensemble of 100 independent random seeds at each 5% density interval, we construct an empirical probability curve of continuous conduction block as a function of fibrosis density. These distributions are subsequently fitted with a non-linear sigmoid function to extract two critical macroscopic parameters:

- The critical percolation threshold (p_c), defined as the exact fibrosis density at which the probability of complete conduction block reaches exactly 50% (SAHIMI; HUNT, 2021). A high p_c indicates that the structural architecture retains cross-domain connectivity even under severe collagen accumulation.
- The percolation transition width (p_{tw}), calculated as the density interval between 10% and 90% block probability. The p_{tw} measures the smoothness of the phase transition; a narrow width indicates an abrupt network collapse, whereas a wide transition window signifies a gradual degradation of the conducting pathways.

Characterizing this structural phase transition is essential, as clinical and computational studies demonstrate that maximum wavefront meandering, fractionated electrograms, and spontaneous rotor formation are highly concentrated near the critical percolation threshold (ALONSO; BÄR, 2013; SACHETTO; ALONSO; SANTOS, 2018; VIGMOND et al., 2016).

3.3.3 Topological Conduction Efficiency (TCE)

While percolation analysis maps the absolute limits of conduction, it does not quantify the geometric retardation imposed on a wave that successfully navigates through a partially blocked medium. To capture this structural delay, we developed a graph-theoretic metric termed the Topological Conduction Efficiency (TCE). For every sample

where cross-domain percolation is achieved, we execute the BFS algorithm a second time, leveraging its property of naturally finding the shortest path length (minimum number of hops) in unweighted graphs from a single source to all reachable destinations (CORMEN et al., 2022). Let L_{dom} represent the absolute Euclidean straight-line distance between the opposing boundaries (equal to the number of cells along the horizontal axis), and L_{avg} denote the mean shortest discrete path length calculated across all successfully reached nodes on the target right boundary. The metric is formulated as:

$$TCE = \frac{L_{dom}}{L_{avg}}. \tag{3.5}$$

Because any non-conducting fibrotic obstacle forces the BFS traversal to take tortuous detours around its boundaries, L_{avg} will strictly exceed L_{dom} in a remodeled substrate, bound by the limit $TCE \in (0, 1]$. In this computational framework, TCE acts as a direct structural proxy for physical wave meandering and tissue tortuosity. A low TCE indicates a labyrinthine substrate that imposes severe geometric conduction slowing, decoupling the physics of structural delay from the sub-cellular kinetics of ionic channel downregulation.

4 ELECTROPHYSIOLOGY AND NUMERICAL METHODS

Once the spatial and structural distributions of cardiac fibrosis have been mathematically generated and categorized, the next fundamental phase of our computational pipeline consists of translating these static geometric domains into dynamic and excitable domains. The objective of this chapter is to formalize the biophysical and mathematical formulations that govern electrical wave propagation and metabolic stress in cardiac tissue, alongside the numerical methods used to solve these systems.

The electrophysiological simulations were designed to measure how geometric features dictate the probability of sustained reentry. Again, using the same procedure as the previous characterization (Chapter 3), 7600 samples — considering the permutation of densities, fibre orientations, and 100 random seeds — were generated per fibrosis phenotype, including *uniform*, to ensure statistical robustness.

4.1 CELLULAR MODEL AND HYPOXIC ADAPTATION

We model the FC as a heterogeneous excitable medium composed of two distinct elements: a non-conductive obstacle field representing the collagen-rich ECM and a surviving population of cardiomyocytes. The surviving cardiomyocytes, entrapped within the boundaries of the FC, are modeled to reflect the severe electrophysiological consequences of a compromised metabolic microenvironment, differentiating them from the fully excitable healthy tissue surrounding the lesion.

To simulate human ventricular action potential dynamics under these complex conditions, we employed the ten Tusscher (TT3) ventricular cell model (TUSSCHER; PANFILOV, 2006) adjusted to represent the epicardial variant. The ionic currents (I_{ion}) present in the TT3 model are:

$$\begin{aligned} I_{ion} = I_{Na} + I_{K1} + I_{to} + I_{Kr} + I_{Ks} + I_{CaL} + I_{NaCa} + \\ + I_{NaK} + I_{pCa} + I_{pK} + I_{bCa} + I_{bNa}, \end{aligned} \tag{4.1}$$

where each ion channel, exchanger, or pump depends on the transmembrane potential and specific gating variables. Under healthy physiological conditions, this formulation reproduces a standard APD of approximately 300 ms.

To formalize the hypoxic status of the entrapped myocytes, we introduced specific adaptations to the standard TT3 equations to account for intracellular Adenosine Triphosphate (ATP) depletion, a hallmark of severe ischemia. Following established modeling procedures for hypoxia (SACHETTO; ALONSO; SANTOS, 2018; OLIVEIRA et al., 2018; PEREIRA et al., 2024), we modified the cellular dynamics primarily by introducing an outward ATP-sensitive potassium current (I_{KATP}) in Eq. (4.1). The formulation for this

current is defined by:

$$I_{KATP} = g_{KATP}(V - E_K), \tag{4.2}$$

where E_K is the potassium reversal potential and g_{KATP} is proportional to the fraction of open channels (P_{ATP}), which is calculated following:

$$P_{ATP} = \frac{1}{1 + \left(\frac{[ATP]_i}{k_{0.5}}\right)^H}, \tag{4.3}$$

with the constants as established by Oliveira *et al.* (OLIVEIRA et al., 2018), $H = 2$ and $k_{0.5} = 0.250$ mM.

The conductance of the L-type calcium current (I_{CaL}) was also modified to become dependent on ATP availability, reflecting the metabolic down-regulation of calcium handling during extreme stress. This is achieved by scaling the original permeability by the factor $P_{CaL,ATP}$ as follows:

$$P_{CaL,ATP} = \frac{1}{1 + \left(\frac{k_{0.5}}{[ATP]_i}\right)^H}, \tag{4.4}$$

with the parameters values (OLIVEIRA et al., 2018) $H = 2.6$ and $k_{0.5} = 1.4$ mM.

This approach provides a framework where the severity of the hypoxic condition is directly and inversely governed by the scalar parameter $[\text{ATP}]_i$. As $[\text{ATP}]_i$ decreases, I_{KATP} intensifies (Eq. (4.3)) and the inward calcium flux is suppressed (Eq. (4.4)). Consequently, the primary outcome of this metabolic degradation is a progressive and severe abbreviation of the APD. In our experimental scenarios, simulating acute localized hypoxia, the intracellular ATP concentration within the fibrotic core was set to $[ATP]_i = 2.0$ mM. According to this modifications and this specific parametrization, the cellular APD drastically abbreviates to approximately 21 ms (SACHETTO; ALONSO; SANTOS, 2018).

4.2 TISSUE ELECTROPHYSIOLOGY MODEL

To simulate the macroscopic propagation of electrical excitation wavefronts through the medium, we employed the standard reaction-diffusion monodomain formulation. Mathematically, the cardiac tissue is modeled as a functional continuum where the intracellular and extracellular spaces are coupled through a localized membrane capacitance. The system is governed by a non-linear parabolic partial differential equation (PDE) coupled with a vector of ordinary differential equations (ODEs) describing sub-cellular channel gating variables (BERG et al., 2026):

$$\begin{aligned} \chi C_m \frac{\partial V}{\partial t} &= \nabla \cdot (\boldsymbol{\sigma} \nabla V) - \chi I_{ion}(V, \boldsymbol{\eta}) + I_{stim}, \\ \frac{\partial \boldsymbol{\eta}}{\partial t} &= f(V, \boldsymbol{\eta}), \end{aligned} \tag{4.5}$$

where V is the transmembrane potential, $\chi = 0.14\,\mu\text{m}^{-1}$ is the cell surface-to-volume ratio, $C_m = 1.0\,\mu\text{F/cm}^2$ represents the specific membrane capacitance, I_{ion} is the total transmembrane current density derived from the ventricular cell model kinetics (given by the modified Eq. (4.1) in this work), $\boldsymbol{\eta}$ is the state vector of gating and concentration variables, f is the right hand side of the non-linear system of ODEs describing the dynamics of the state variables, and I_{stim} is an external stimulus.

To account for the complex electrical anisotropy imposed by the myocardial fibre architecture, the electrical conductivity tensor $\boldsymbol{\sigma}(\mathbf{x})$ is defined as a transversely isotropic matrix aligned with the local fibre orientation vector $\mathbf{f}$[1]:

$$\boldsymbol{\sigma} = \sigma_n \mathbf{I} + (\sigma_l - \sigma_n)\mathbf{f} \otimes \mathbf{f}, \tag{4.6}$$

where $\mathbf{I}$ is the identity tensor, $\otimes$ denotes the tensor product, $\sigma_l = 1.334 \times 10^{-4}\,\text{mS}\,\mu\text{m}^{-1}$ represents the longitudinal conductivity parallel to the fibre direction, and $\sigma_n = 1.76 \times 10^{-5}\,\text{mS}\,\mu\text{m}^{-1}$ represents the transverse conductivity perpendicular to the fibres (OLIVEIRA et al., 2018). To guarantee conservation of current within the isolated boundaries of our domain, the system was subjected to homogeneous Neumann no-flux boundary conditions at all external physical interfaces:

$$\mathbf{n} \cdot (\boldsymbol{\sigma} \nabla V) = 0, \tag{4.7}$$

where $\mathbf{n}$ is the outward unit normal vector of the domain surface.

4.3 NUMERICAL SOLVER AND HIGH-PERFORMANCE COMPUTATION

The numerical integration of the coupled systems defined by Eqs. (4.5) and (4.1) presents a severe computational bottleneck due to the stiff nature of the ionic reaction currents and the grid resolutions required to solve macroscopic sheets. Numerical solutions were achieved using `MonoAlg3D`, an open-source high-performance solver specifically optimized for parallel execution on GPUs via the NVIDIA CUDA architecture (OLIVEIRA et al., 2018; BERG et al., 2026).

The spatial discretization of the domain utilized a cell-centred Finite Volume Method (FVM) implemented on a regular hexahedral mesh with a spatial resolution of $\Delta x = 100\,\mu\text{m}$. This FVM approach guarantees strict local mass conservation of current across the heterogeneous interfaces separating the conductive myocardium and the non-conductive fibrotic voxels. To handle the computational stiffness efficiently, a Godunov operator splitting scheme (SUNDNES; MARDAL; CAI, 2006) decoupled the parabolic PDE propagation from the non-linear ODE reaction systems at each time step

[1] In our computational tissue domains, the local coordinate system defines $\mathbf{f}$ along the longitudinal axis of the coordinates, but it is dynamically rotated using the rotation matrices defined in Chapter 2 to introduce fibre orientation anisotropy.

$\Delta t = 0.02\,\text{ms}$. The cellular gating kinetics ODEs were integrated using the second-order Rush-Larsen method, thereby maintaining extreme numerical stability without requiring computationally prohibitive fully implicit solvers.

4.4 SIMULATION SCENARIOS AND DOMAINS

To systematically evaluate the arrhythmogenic potential of the generated patterns, we designed three distinct computational configurations (Fig. 14). These span from planar models to 3D domains: a 2D homogeneous substrate (Scenario I), a 2D heterogeneous tissue incorporating a dense FC and a structural BZ (Scenario II), and a fully 3D volumetric domain to capture transmural wave dynamics (Scenario III).

Figure 14 – Representative spatial domains across the three experimental scenarios. Columns illustrate the distinct spatially correlated phenotypes alongside the *uniform* baseline. Rows depict the geometric configurations: Scenario I features a fibrotic homogeneous 2D slab, Scenario II introduces a heterogeneous 2D focal lesion with a transitional BZ, and Scenario III extends the substrate into a 3D volumetric domain. The displayed densities correspond to the specific realizations shown.

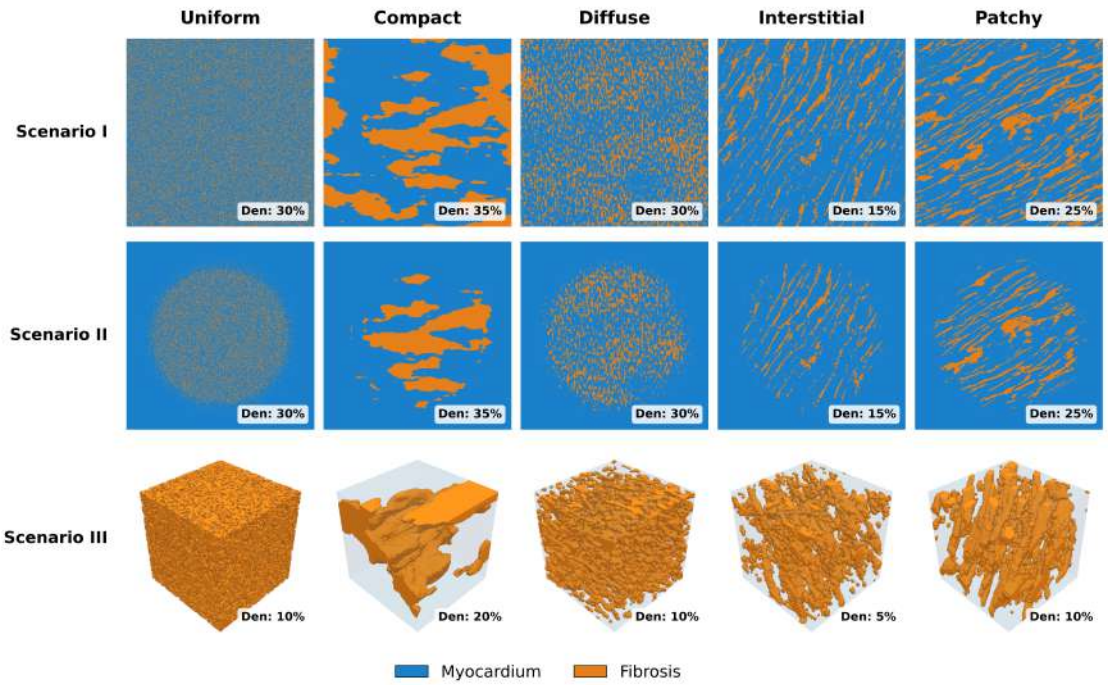

Source: Elaborated by the author (2026).

Scenario I (2D Full Fibrotic Domain): The first configuration consisted of a homogeneous 4×4 cm two-dimensional slab. The entire domain was populated by the fibrotic structure and its associated metabolic stress ($[\text{ATP}]_i = 2.0$ mM). This scenario isolates the intrinsic wave fractionation dynamics within a highly diseased substrate.

Scenario II (2D Heterogeneous Domain with FC and BZ): To mimic the architecture of a focal lesion, the second configuration embedded a central circular FC (diameter = 2.8 cm) within a 4×4 cm healthy myocardial domain. To represent pathophysiological transition, a BZ with a width of 0.28 cm was implemented around the FC. Within the BZ, two gradients were established: (i) a metabolic gradient, linearly interpolating $[ATP]_i$ from 2.0 mM to 6.8 mM; and (ii) a structural gradient, where the target obstacle density decayed exponentially according to Eq. (2.8).

Scenario III (3D Full Fibrotic Domain): To assess the influence of transmural connectivity, the homogeneous substrate from Scenario I was expanded into a $1 \times 1 \times 1$ cm volumetric domain under hypoxia. This setup is crucial for determining if the structural hierarchies observed in planar substrates persist when the wavefront gains new propagation routes.

4.5 STIMULATION PROTOCOL AND OUTPUT DEFINITION

To assess the arrhythmogenic potential of each specific realization without introducing bias from artificial external triggers, a single planar stimulus was delivered along the left boundary of the tissue, encompassing a 500 μm region parallel to the vertical edge. The stimulus consisted of a rectangular current pulse with an amplitude of $-38.0\,\mu A/cm^2$ and a duration of 2.0 ms. No secondary cross-shocks or premature (S1-S2) stimulation protocols were applied. Consequently, any rotating wavefront or chaotic wave fractionations observed later in the execution arose spontaneously from the mechanical break of the wavefront as it interacted with the discrete boundaries and tortuous corridors of the fibrotic obstacle fields under metabolic hypoxic stress.

The electrophysiological outcome of each individual simulation run was tracked dynamically and classified as a discrete binary event. We explicitly defined a *sustained reentry* as the persistence of self-sustaining electrical activation that continuously rotated within the grid boundaries for more than 1000 ms after the application of the initial pulse (as illustrated in the snapshot timeline of Fig. 15). This cutoff represents a biophysical regime equivalent to multiple full rotations of a rotor given the abbreviated 21 ms hypoxic APD (SACHETTO; ALONSO; SANTOS, 2018). Conversely, if the wavefront collided with the non-conductive boundaries or self-extinguished prior to the 1000 ms threshold, the simulation was catalogued as a *non-sustained event*.

Figure 15 – Representative visual definition of a sustained reentry within a 2D domain featuring a *diffuse* fibrosis pattern. Following the initial planar stimulus at the left boundary (2 ms), the wavefront propagates through the tissue. This chaotic electrical activity persists beyond the predefined 1000 ms threshold, fulfilling the empirical criteria for a sustained arrhythmogenic event.

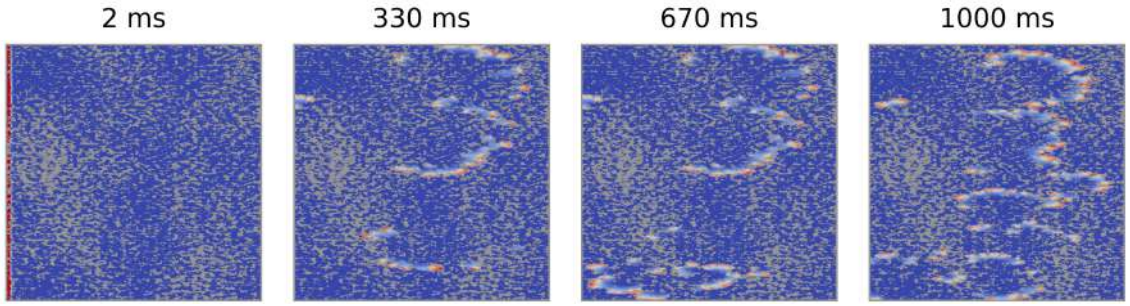

Source: Elaborated by the author (2026).

5 STATISTICAL MODELING AND ARRHYTHMOGENIC RISK QUANTIFICATION

The biophysical simulations executed within `MonoAlg3D` generate a massive dataset of discrete binary outcomes: either the successful induction of a self-sustaining reentrant circuit or the premature self-termination of the wavefront. While these individual mechanistic runs provide deep insights into localized wave-obstacle interactions, a higher-level mathematical framework is required to synthesize these discrete points into knowledge about reentry induction. This chapter formalizes our secondary data science pipeline, designed to rigorously quantify and compare the arrhythmogenic risk profiles emerging from the distinct fibrotic micro-architectures.

To ensure transparency and separate experimental observation from mathematical inference, this chapter is structured into three progressive analytical stages. First, we outline the criteria used to establish the raw, empirical vulnerability windows directly from our simulation ensemble. Second, we present Firth's bias-reduced penalized logistic regression, deployed to handle the mathematical challenges of rare events and calculate global relative odds ratios against the uncorrelated *uniform* baseline. Finally, we detail the mathematical formulation of GAM using penalized regression splines, which allow us to map the complex, topology-specific probability curves across the density spectrum and pinpoint the exact critical thresholds of maximum arrhythmic vulnerability.

5.1 DELINEATION OF EMPIRICAL VULNERABILITY WINDOWS

Prior to the application of predictive mathematical curves, the raw data collected from the simulation ensemble was evaluated to define the exact *empirical vulnerability window* of each phenotype. In the context of this study, a vulnerability window represents the physical range of collagen densities $[\rho_{min}, \rho_{max}]$ wherein at least one independent random seed successfully triggered a sustained reentry.

5.2 STATISTICAL RISK QUANTIFICATION

To translate the discrete, highly non-linear binary outcomes collected across the density spectrum into smooth, continuous probabilistic risk profiles, we deployed a secondary multi-stage statistical pipeline executed in R. While the empirical windows establish the absolute boundaries of risk, they are subject to stochastic sampling variations. Statistical modeling allows us to estimate the underlying maximum probabilities and pinpoint the critical peak risk densities.

5.2.1 Firth's Bias-Reduced Logistic Regression

To quantify the overall magnitude of arrhythmogenic risk between the distinct patterns, we employed Firth's bias-reduced logistic regression (FIRTH, 1993). This penalized likelihood method provides valid parameter estimates even in the presence of rare events (e.g., within highly protective phenotypes). The spatially uncorrelated *uniform* pattern was designated as the reference baseline (Odds Ratio = 1.00), allowing us to formally quantify the relative risk introduced by macroscopic spatial correlation.

5.2.2 GAM for Non-linear Risk Profiles

To map these complex dynamics without forcing arbitrary polynomial shapes on the risk distributions, we implemented GAM (HASTIE; TIBSHIRANI, 1986) utilizing the `mgcv` package (WOOD, 2017). However, a strict prerequisite was established to ensure mathematical validity: a specific fibrosis pattern was classified as *active* and subjected to the GAM spline fitting only if it achieved a minimum threshold of 10 sustained reentries across its complete multi-seed ensemble.

This filtering criterion is critical to avoid dilution bias and prevent mathematical artifacts during the convergence of the penalized splines. For the active phenotypes, the model was fitted using a `quasibinomial` family with a `logit` link function to account for overdispersion in clustered data, optimizing the penalized regression splines using a basis dimension constrained to $k = 5$ to guarantee smooth risk profiles.

Furthermore, to ensure robust spline parameter estimation and prevent boundary artifacts caused by extended regions devoid of events, the GAM was strictly fitted within an effective density envelope. This global envelope was dynamically defined by bounding the absolute minimum and maximum densities at which sustained reentries were empirically observed across all active phenotypes, symmetrically extended by a 5% density padding.

6 RESULTS

6.1 QUANTITATIVE STRUCTURAL DESCRIPTORS

The structural metrics summarized in Table 2 and Table 3 quantitatively characterize the morphological diversity of the synthesized fibrotic phenotypes across both 2D and 3D domains. It is crucial to note that the values presented in these tables represent the global means for each metric, averaged across all generated samples spanning the entire simulated density spectrum. These aggregated values demonstrate that each pattern occupies a distinct region of the structural parameter space. The dynamic evolution of these metrics as collagen density increases is explicitly shown in Figs. 16 and 17.

Table 2 – Topological and morphological metrics for 2D domains (400×400 cells). Values denote global means. The evaluated metrics are defined as follows: Moran's I (I), Aspect Ratio (AR), Fractal Dimension (D_f), Betti 0 (β_0), Betti 1 (β_1), and Normalized Mean Cluster Size ($\hat{S}$).

Phenotype	I	AR	D_f	β_0	β_1	$\hat{S}$ (%)
Uniform	0.000	1.155	1.854	3565.9	9007.3	0.09
Compact	0.916	1.499	1.659	17.9	11.6	3.40
Diffuse	0.315	1.377	1.816	1440.4	1639.0	0.38
Interstitial	0.445	1.779	1.790	1000.6	948.1	0.69
Patchy	0.548	2.148	1.767	525.4	370.5	1.04

Source: Elaborated by the author (2026).

Table 3 – Topological and morphological metrics for 3D domains ($100 \times 100 \times 100$ cells). Values denote global means. The evaluated metrics are defined as follows: Moran's I (I), Aspect Ratio (AR), Fractal Dimension (D_f), Betti 0 (β_0), Betti 1 (β_1), Betti 2 (β_2), and Normalized Mean Cluster Size ($\hat{S}$).

Phenotype	I	AR	D_f	β_0	β_1	β_2	$\hat{S}$ (%)
Uniform	0.000	1.080	2.696	2243.8	40028.9	25041.4	<0.01
Compact	0.877	1.204	2.448	6.5	10.8	2.1	0.77
Diffuse	0.228	1.109	2.665	955.8	7778.4	2115.9	0.02
Interstitial	0.334	1.183	2.642	732.2	5008.7	1544.0	0.05
Patchy	0.467	1.310	2.601	352.5	1595.5	395.5	0.14

Source: Elaborated by the author (2026).

The spatial autocorrelation, quantified via Moran's I, provides a defining topological signature for each phenotype. As shown in Tables 2 and 3, the *uniform* distribution consistently yields $I = 0.000$, perfectly confirming its mathematical definition as a random spatially uncorrelated field. In contrast, the spatially correlated patterns exhibit an

Figure 16 – Evolution of structural and topological metrics as a function of fibrosis density in 2D domains. Note how Moran's I is the only metric that maintains strict hierarchical separation across the entire spectrum.

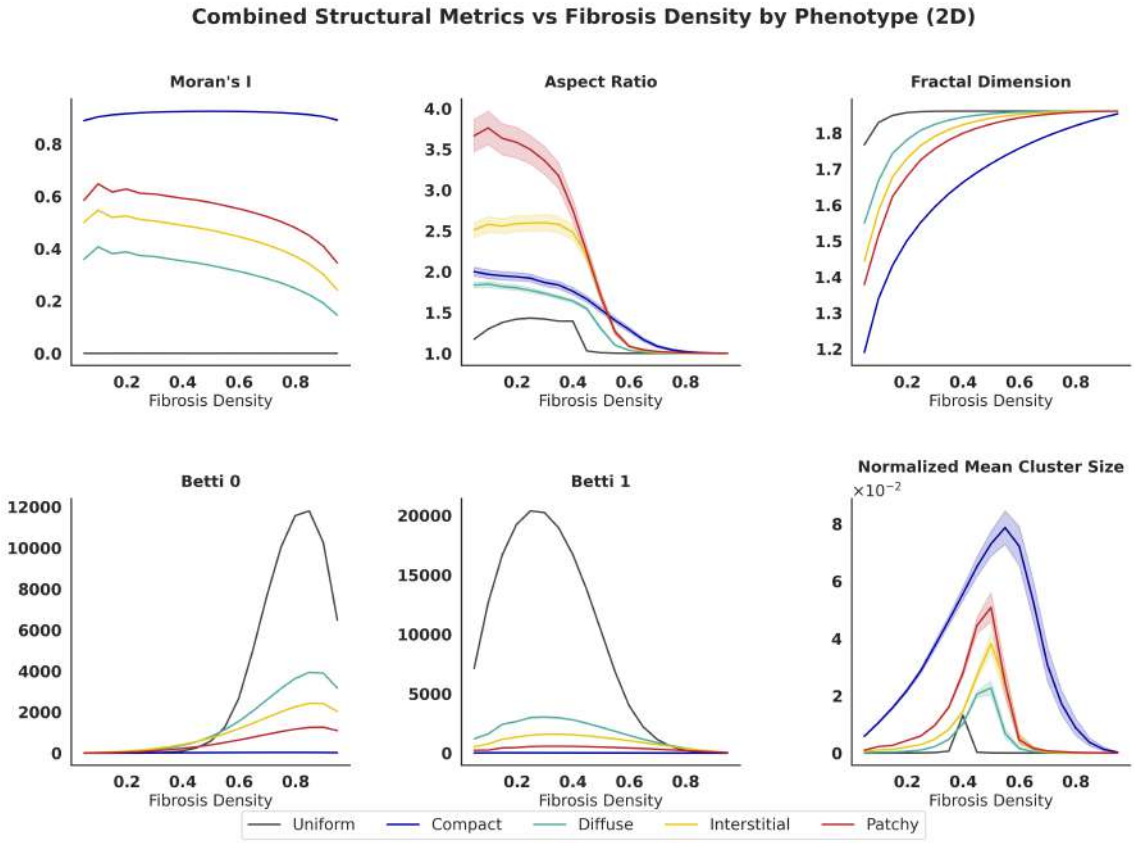

Source: Elaborated by the author (2026).

expected progressive hierarchy: *diffuse* fibrosis ($I = 0.315$ in 2D and $I = 0.228$ in 3D) presents the lowest correlation among the histology-inspired structures, reflecting its scattered nature, while the large solid blocks of the *compact* phenotype yield the highest clustering values ($I = 0.916$ in 2D and $I = 0.877$ in 3D). As expected, since *patchy* has the intrinsic characteristic to have more irregular collagen aggregation, its autocorrelation values ($I = 0.548$ in 2D and $I = 0.467$ in 3D) were consistently greater than *interstitial* ($I = 0.445$ in 2D and $I = 0.334$ in 3D). As illustrated in Figs. 16 and 17, Moran's I is the only evaluated metric that maintains strict hierarchical separation across the entire density spectrum. This density-invariant characteristic confirms that the Perlin framework successfully embeds distinct, intrinsic clustering rules, rendering it a robust feature for automated structural classification and other machine learning applications.

Beyond isolated metrics, the interaction between these geometric features reveals deep structural dependencies. Bivariate distributions (Appendix Figs. 31 for 2D and 32 for 3D) demonstrate that the metrics form distinct relations. To formally quantify these interdependencies, we compared linear (Pearson) and rank-based monotonic (Spearman)

Figure 17 – Evolution of structural and topological metrics as a function of fibrosis density in 3D domains. Note how Moran's I maintains strict hierarchical separation across the entire spectrum, unlike metrics such as Betti numbers, which exhibit density-dependent phase transitions.

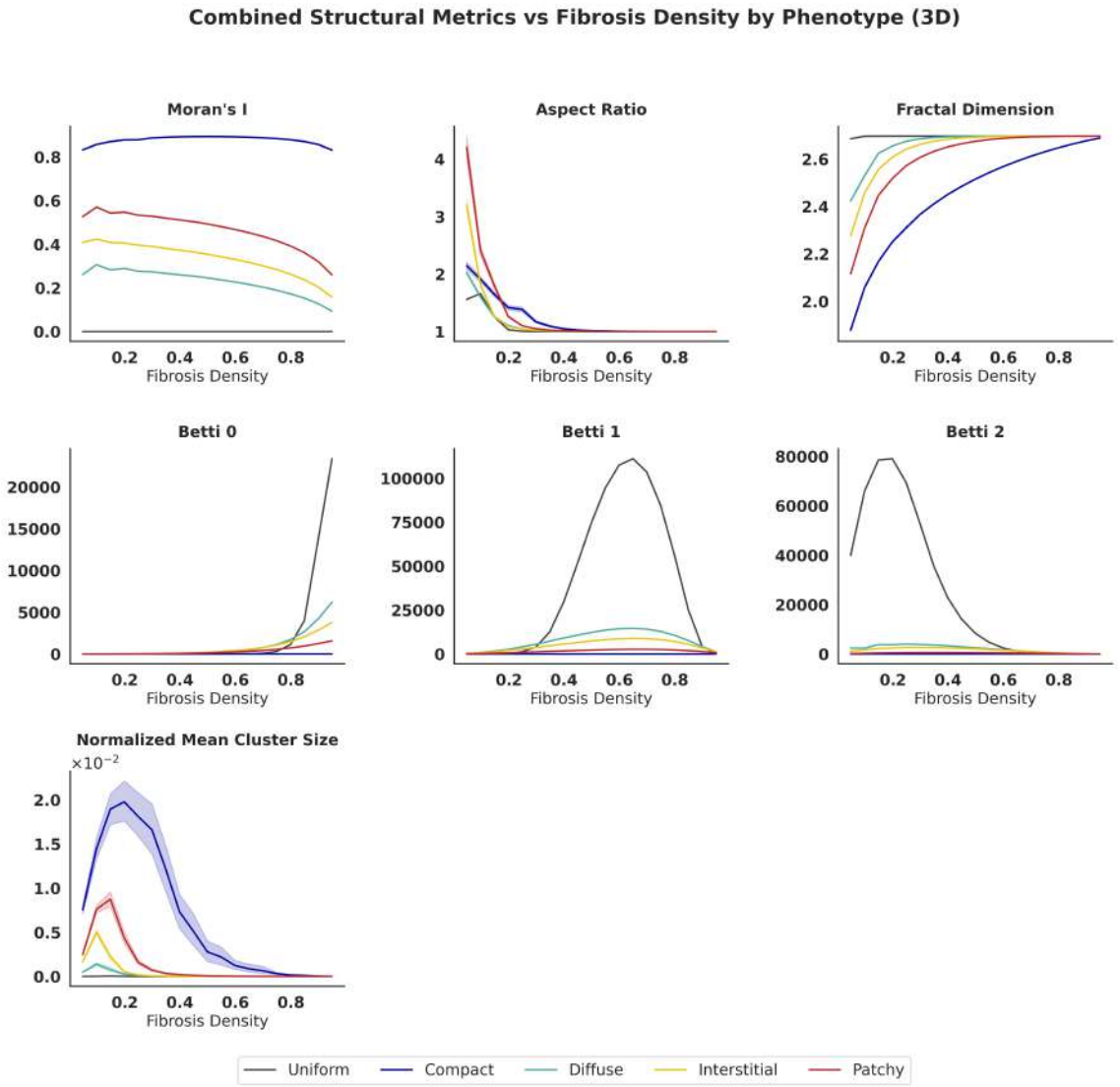

Source: Elaborated by the author (2026).

correlation matrices (Appendix Figs. 33 for 2D and 34 for 3D). The consistently stronger coefficients observed in the Spearman analyses confirm that the relationships governing cardiac tissue architecture, such as the dynamic between I and $\hat{S}$, are fundamentally non-linear.

The geometric elongation of the generated barriers is captured by AR. In 2D domains, the *patchy* ($AR = 2.148$) and *interstitial* ($AR = 1.779$) patterns form elongated and thin macroscopic features and have the highest ARs, accurately reflecting their biological tendency to trace parallel to myocardial fibres. The *uniform* pattern, lacking any directional bias, yields nearly equilateral features, consequently having the lowest

AR ($AR = 1.155$). Interestingly, the transition to 3D volumetric domains induces a universal decrease in AR across all phenotypes. While the *patchy* pattern remains the most elongated ($AR = 1.310$), the *compact* and *interstitial* patterns swap hierarchical positions ($AR = 1.204$ for *compact* and $AR = 1.183$ for *interstitial*). This disruption highlights a potential limitation in the current mathematical formulation of the 3D AR. Because the metric evaluates the ratio between the absolute maximum and minimum bounding box dimensions, ignoring the intermediate third axis, it may hide complex planar deformations (e.g., sheet-like versus tube-like structures) that occur when planar barriers expand into the volumetric domain. The *uniform* noise remains the most isometric pattern ($AR = 1.080$), closely followed by *diffuse* ($AR = 1.109$).

D_f encapsulates the scaling from planar to volumetric limits in terms of Euclidean space: 2D textures scale between 1 and 2, while 3D textures scale between 2 and 3. In both dimensions, the hierarchy remained strictly consistent: *uniform* and *diffuse* approach the maximum Euclidean limits ($D_f = 1.854$ and 1.816 in 2D, respectively), highlighting penetrating branching throughout the medium that maximizes the interfacial boundary area between the conductive and non-conductive regions. On the other hand, the *compact* pattern exhibits the lowest scale-invariance ($D_f = 1.659$ in 2D), mathematically reflecting its dense and non-branching features that minimizes surface roughness.

The topological connectivity, evaluated via Betti numbers (β_0, β_1, and β_2), reveals the impact of dimensionality on the conducting tissue, while corroborating the phenotypic definitions. In 2D (results of Table 2), the highly fragmented *uniform* pattern shatters the myocardium into thousands of isolated islands ($\beta_0 = 3565.9$) and tiny independent loops ($\beta_1 = 9007.3$). Conversely, the contiguous walls of the *compact* pattern barely disrupt global connectivity ($\beta_0 = 17.9$, $\beta_1 = 11.6$). As observed in Figs. 16 and 17, Betti numbers exhibit pronounced density-dependent parabolic transitions. This behaviour makes physical sense: at low densities, adding fibrosis creates new isolated obstacles (increasing loops, β_1); however, as density further increases, these individual obstacles begin to touch and merge into massive structures, destroying the separate loops and causing the Betti metrics to decline. In 3D domains, the number of isolated healthy clusters (β_0) drops significantly compared to 2D, as volumetric space allows myocytes to easily overcome isolation via the z-axis. Simultaneously, β_1 explodes exponentially (except for the *compact* core) because the additional spatial dimension offers more pathways for myocardial strands to encircle fibrotic obstacles, thereby multiplying the number of independent topological loops embedded within the tissue matrix.

Finally, $\hat{S}$ dictates the mass and surface boundaries of the barriers, tracking the expected biological aggregation of each pattern. As detailed in Table 2, the values follow an hierarchical sequence: the *compact* pattern forms the most massive fibrotic blocks ($\hat{S} = 3.40\%$), followed by the thick strands of *patchy* ($\hat{S} = 1.04\%$) and *interstitial* ($\hat{S} = 0.69\%$), down to the finely scattered *diffuse* ($\hat{S} = 0.38\%$) and *uniform* ($\hat{S} = 0.09\%$)

distributions. While its hierarchy is fully preserved between 2D and 3D, its magnitude changed. In 3D, $\hat{S}$ drops by orders of magnitude because the volumetric connectivity causes almost all isolated elements to be rapidly absorbed into the largest cluster, which is excluded from the calculation.

6.2 WAVE PERCOLATION AND CONDUCTION EFFICIENCY

Plots in Fig. 18 show the probability of continuous conduction as a function of fibrosis density, with p_c and p_{tw} values summarized in Tables 4 and 5. It is important to formally establish that TCE values reported in these tables represent the average exclusively across the subset of samples that conducts from left to right — that is, specific fibrosis configurations that maintained at least one continuous conducting pathway connecting the left stimulus boundary to the right boundary of the domain.

Figure 18 – Structural percolation analysis for 2D (A) and 3D (B) fibrotic domains. The curves represent the sigmoid fits for the probability of continuous conduction as a function of fibrosis density. Vertical dashed lines indicate the critical percolation threshold (p_c) for each phenotype. The introduction of spatial correlation in textures smoothens the phase transition compared to the abrupt collapse of the *uniform* baseline. Moreover, the transition to 3D induces a right-shift in p_c.

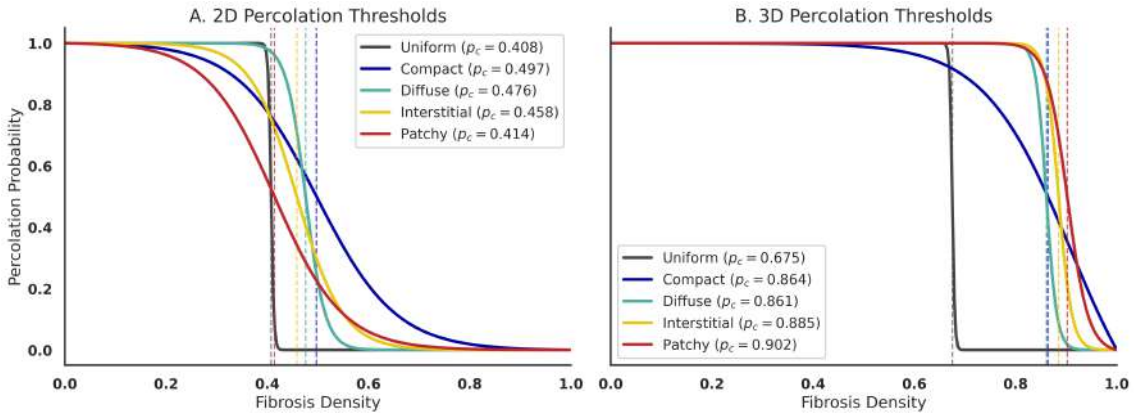

Source: Elaborated by the author (2026).

Table 4 – Wave percolation and conduction efficiency metrics for 2D domains.

Phenotype	p_c	p_{tw}	TCE
Uniform	0.408	0.012	0.813
Compact	0.497	0.343	0.839
Diffuse	0.476	0.085	0.820
Interstitial	0.458	0.200	0.788
Patchy	0.414	0.296	0.767

Source: Elaborated by the author (2026).

Table 5 – Wave percolation and conduction efficiency metrics for 3D domains.

Phenotype	p_c	p_{tw}	TCE
Uniform	0.675	0.011	0.794
Compact	0.864	0.378	0.855
Diffuse	0.861	0.045	0.801
Interstitial	0.885	0.057	0.803
Patchy	0.902	0.090	0.808

Source: Elaborated by the author (2026).

The critical thresholds obtained for the uncorrelated *uniform* distribution ($p_c = 0.408$ in 2D; $p_c = 0.675$ in 3D) correspond precisely to the theoretical site percolation thresholds for classical 2D square and 3D simple cubic lattices (STAUFFER; AHARONY, 2018; SAHIMI; HUNT, 2021), validating their computational calculation here. For the spatially correlated patterns, the analysis reveals some links between the percolation metrics and the geometric descriptors previously established and shown in Tables 2 and 3. In 2D, despite possessing one of the highest macroscopic mass among the patterns ($\hat{S} = 1.04\%$), the *patchy* phenotype exhibits a relative low percolation threshold ($p_c = 0.414$), nearly identical to the *uniform* baseline. This behaviour might be explained by its $AR = 2.148$, because, in a 2D grid, long continuous collagen septa, characteristic of *patchy* fibrosis, easily bisect the domain, severing cross-tissue connectivity even at lower densities. Conversely, *compact* fibrosis requires much higher density burdens to block conduction ($p_c = 0.497$), as its localized clustering ($\hat{S} = 3.40\%$ and $I = 0.916$) leaves vast myocardial corridors unobstructed.

The leap to 3D drastically shifts p_c to much higher densities (for the spatially correlated patterns from ≈ 0.46 in 2D to ≈ 0.87 in 3D). Remarkably, the hierarchy of p_c is entirely inverted for the *patchy* pattern in 3D, becoming the most resilient conducting medium ($p_c = 0.902$). This demonstrates that while elongated 2D strands act as perfect planar separators, enhanced 3D spatial connectivity allows the wavefront to effortlessly bypass these walls via z-axis routes.

The transition width (p_{tw}) further separates the *uniform* fibrosis from the histology-inspired microstructures. The *uniform* baseline undergoes an abrupt, nearly instantaneous phase change from conductive to non-conductive ($p_{tw} \approx 0.01$). In contrast, the other patterns, characterized by high spatial autocorrelation (I) and cluster sizes ($\hat{S}$), such as the *compact* and *patchy* patterns, drastically stretch the transition window. This indicates that macroscopic clustering degrades the tissue network more gradually, supporting wave propagation across a much broader spectrum of tissue damage.

Geometric retardation is quantified by TCE; values close to 1 indicate that the fibrotic structure does not interfere too much in the electrical wave propagation. Across

all dimensions, *compact* consistently remains as the pattern that least interferes the propagation ($TCE = 0.839$ in 2D and $TCE = 0.855$ in 3D). This behaviour is mechanistically corroborated by its extremely low topological fragmentation ($\beta_1 = 11.6$) and low boundary roughness ($D_f = 1.659$), so the electrical wave simply travels around a few dense fibrotic blocks without suffering constant detours. In 2D, *patchy* ($TCE = 0.767$) and *interstitial* ($TCE = 0.788$) dictate the highest conduction delays. This severe retardation is the direct consequence of their high AR. The elongated septa force the advancing wavefront into tortuous, zigzagging pathways, significantly increasing the path that the propagation wave has to travel from one side to the other of the domain.

However, in 3D, this hierarchy is entirely disrupted: *uniform* noise becomes the most restrictive medium ($TCE = 0.794$), while *patchy* and *interstitial* conduction efficiency recover ($TCE = 0.808$ and $TCE = 0.803$). This inversion might be explained looking at the Betti numbers and D_f. In 3D, the *uniform* transforms the medium into a microscopic sponge, mathematically reflected by its maximal fractal dimension ($D_f = 2.696$) and an explosion of independent topological loops ($\beta_1 = 40,028.9$). Navigating this pervasive labyrinth imposes constant localized splitting and delays on the wavefront. Conversely, the macroscopic walls of *patchy* and *interstitial* architectures lose their geometric blocking efficiency in 3D due to the aforementioned volumetric bypass, allowing the wave to navigate using less tortuous paths.

6.3 SCENARIO I: WAVE FRACTIONATION AND ANCHORING DYNAMICS

In the first 2D electrophysiology scenario, the arrhythmogenic risk profiles reveal a fundamental divergence between *uniform* and histology-inspired topologies. The empirical probability curves and corresponding vulnerability windows are explicitly detailed in Fig. 19. The top panel plots the absolute probability of inducing a sustained reentry (y-axis) as a function of the fibrosis density (x-axis), with distinct curves tracking each fibrosis phenotype. The bottom Gantt chart visually maps the effective vulnerability windows, the continuous density intervals where at least one sustained event was recorded, annotated with the absolute count of induced arrhythmias per pattern in that window.

Analysing these distributions shows that the uncorrelated *uniform* restricts arrhythmic events to a narrow density window (20% to 40%). In contrast, correlated architectures such as *diffuse* and *patchy* support sustained reentries across a vastly expanded spectrum (5% to 60%). This broadening of the vulnerability window is a direct electrophysiological consequence of the extended p_{tw} previously reported in Table 4. Because spatial correlation prevents an abrupt topological collapse, the tissue maintains fractionated but viable conduction pathways over a much wider range of collagen density.

The *uniform* distribution exhibits an anomalous bimodal risk profile in Fig. 19, with sharp peaks emerging at 25% and 35% densities. To investigate the origin of this

Figure 19 – Empirical analysis of sustained reentries in Scenario I. (Top) Absolute probability of sustained reentry across fibrosis densities. (Bottom) Gantt chart illustrating the effective vulnerability windows. Uncorrelated *uniform* exhibits a narrow arrhythmogenic band, whereas spatially correlated patterns maintain arrhythmic substrates over a broad spectrum of tissue degradation. Numbers inside the bars indicate the sustained reentry count per interval.

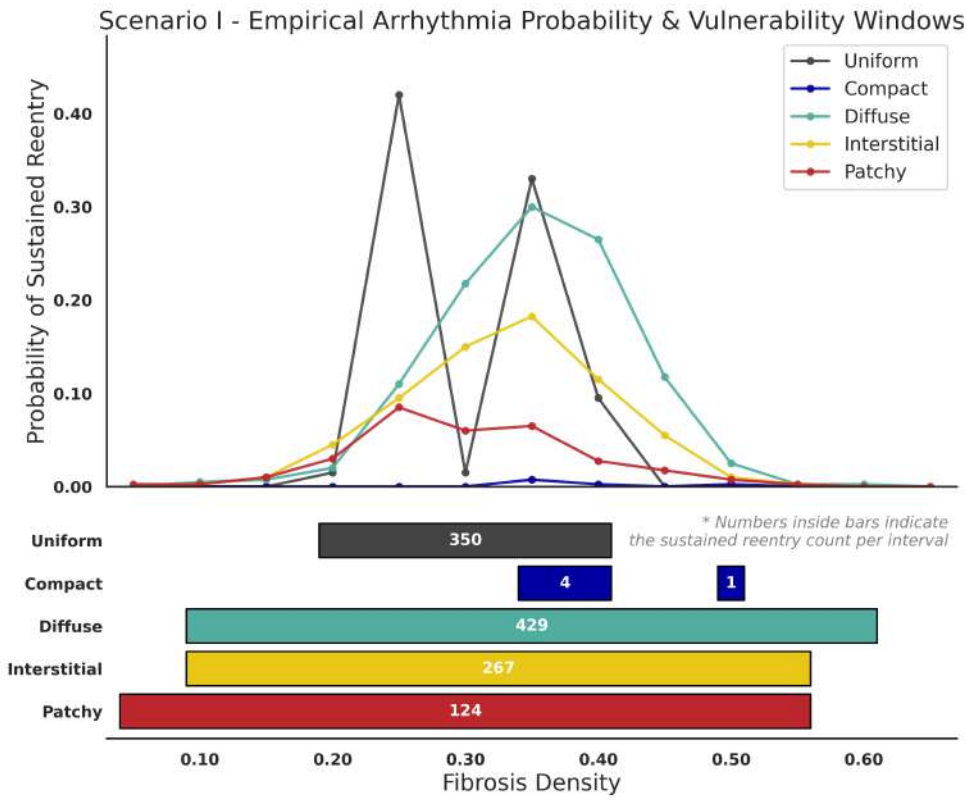

Source: Elaborated by the author (2026).

bimodality, we decomposed the empirical probabilities by the underlying myocardial fibre orientation angle, as presented in Fig. 20. This breakdown reveals that the apparent dual-peak behaviour is not apparently a true intrinsic property of the *uniform* noise, but rather an artifact of the angular sampling interacting with the model's electrical anisotropy tensor. The vulnerability peak explicitly shifts as a function of the fibre angle, probably resetting at 45°. Consequently, orthogonal and parallel alignments (0° and 90°) generate identical sharp vulnerability peaks exactly at 25% density, while intermediate complementary angles (30° and 60°) shift the functional block threshold, peaking synchronously at 35%. This indicates that the *uniform* distribution possesses a rigid, orientation-dependent vulnerability that was under-represented by evaluating only four discrete angles.

To quantify the overall global risk magnitude across the entire density spectrum, Firth's regression (Fig. 21) evaluated the relative odds of each spatially correlated phenotype against the *uniform* baseline (OR = 1.00). In this forest plot, markers positioned to the

Figure 20 – Empirical probability of sustained reentry separated by fibre orientation in Scenario I.

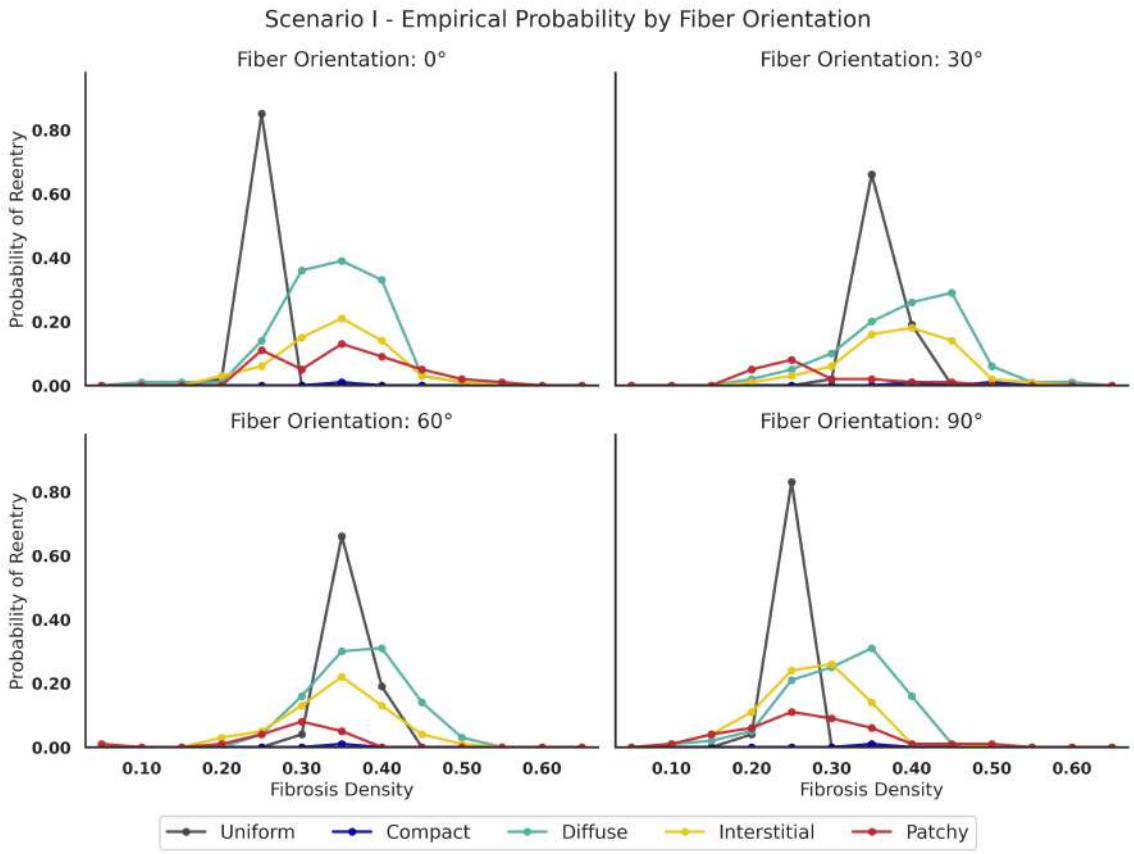

Source: Elaborated by the author (2026).

right of the dashed baseline indicate an exacerbated arrhythmogenic risk, while markers to the left denote a protective effect.

The *compact* phenotype remained functionally inert (OR = 0.01). This near-zero risk is mathematically consistent with its massive cluster size ($\hat{S}$ = 3.40%, Table 2) and low fractal boundary roughness (D_f = 1.659), reflecting its massive and smooth obstacles that simply deflect wavefronts without causing continuous wave break. *Diffuse* fibrosis generated the highest incidence of events (429 sustained reentries) and was the only phenotype to present an elevated global risk (OR = 1.24) compared to the *uniform* baseline. This severe arrhythmogenicity may be associated to its high fractal dimension (D_f = 1.816) and β_1 (β_1 = 1639.0), reflecting its characteristic of being microscopically rough and scattered, maximizing localized source-sink mismatches across the tissue.

In contrast, the highly anisotropic *interstitial* (OR = 0.75) and *patchy* (OR = 0.34) patterns manifested functionally protective profiles, despite their extended vulnerability windows. This protective nature can be traced to their topological connectivity. Both patterns exhibited a high number of independent topological loops (β_1, Table 2) combined with extreme aspect ratios ($AR > 1.77$). When a wave navigates these structures, it

is forced into parallel corridors rather than being shattered by random micro-obstacles, reducing the probability of chaotic fibrillation. It is noteworthy, however, that *interstitial* fibrosis generated more than twice the number of sustained reentries (267 events) compared to the *patchy* architecture (124 events).

Figure 21 – Firth's Bias-Reduced Logistic Regression for relative arrhythmia risk in Scenario I. The uncorrelated *uniform* serves as the reference (OR = 1.00). *Diffuse* fibrosis exacerbates global risk, while *patchy* and *interstitial* manifest electrophysiologically protective profiles.

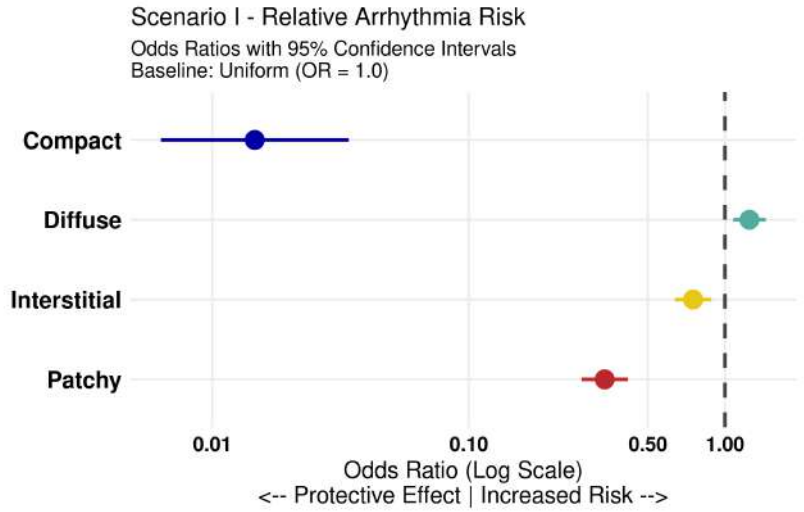

Source: Elaborated by the author (2026).

These mathematically derived hypotheses regarding wave interaction are visually confirmed through the dynamic wavefront analysis presented in Fig. 22. The sequential snapshots of the electrical wave propagation confirm that *uniform* and *diffuse* patterns induce widespread wavefront fractionation, generating multiple transient anchoring points. The *compact* pattern exhibits cohesive propagation, rarely breaking, and when it does, reentries emerge as single anchored rotors. Meanwhile, the geometric constraints of the *interstitial* and *patchy* phenotypes force the wave through narrow parallel corridors, physically stretching the rotating wave and resulting in elliptical reentrant circuits.

6.4 SCENARIO II: STRUCTURAL BOUNDARIES AND ROTOR STABILIZATION

In Scenario II, the homogeneous fibrotic slab of Scenario I is replaced by a localized FC surrounded by a transitional BZ and healthy myocardium. The empirical probability distributions and effective vulnerability windows for this configuration are detailed in Fig. 23. Similar to the previous scenario, the top panel tracks the absolute probability of inducing a sustained reentry against the core fibrosis density, while the bottom Gantt chart quantifies the absolute number of events. Comparing these outcomes directly with

Scenario I reveals a drastic reduction in the absolute incidence of sustained reentries across all phenotypes and a systemic compression of the vulnerability windows. For instance, the maximum reentry probability for the *uniform* baseline plummeted from over 40% in Scenario I to approximately 15% in Scenario II. This global attenuation is a direct consequence of the reduced spatial mass of the diseased tissue; the smaller fibrotic footprint simply provides less physical space for a wandering wavefront to establish the minimum path length required to stabilize a sustained reentrant circuit.

When evaluating peak vulnerabilities giving by the GAM (Appendix Fig. 36 and Appendix Table 7), the elongated *interstitial* and *patchy* phenotypes exhibited a substantial rightward shift in their critical densities (moving from 33% to 41%, and from 29% to 45%, respectively). This shift can be mechanistically attributed to the spatial gradient of the BZ. Because the obstacle density decays exponentially from the core towards the healthy tissue, a much higher collagen density is required to maintain the critical degree of structural fragmentation needed to fractionate the wavefront across the lesion's periphery. The critical density for the *diffuse* architecture remained relatively preserved (36% to 37%).

To verify if the circular geometry of the localized FC mitigated the angular artifacts observed in Scenario I, we evaluated the empirical probabilities parsed by fibre orientation (Fig. 24). The *uniform* baseline continued to exhibit the same fibre orientation-dependent vulnerability peaks. As observed in the individual panels, core densities of 25% consistently generated sharp peaks at orthogonal angles (0° and 90°), while the complementary intermediate angles (30° and 60°) shifted the peak vulnerability to higher densities ($\approx 35\% - 40\%$).

This boundary interaction reconfigured the global risk hierarchy, as quantified by Firth's regression in Fig. 25. The forest plot maps the relative arrhythmogenic odds of the spatially correlated patterns against the *uniform* baseline (OR = 1.00). Unlike Scenario I (where *diffuse* fibrosis was significantly more arrhythmogenic), *diffuse* and *uniform* patterns presented statistically identical global risk profiles in Scenario II (OR = 1.00). This convergence highlights a critical bio-physical dynamic: the smooth structural density gradient of the BZ might be acting as an artificial spatial correlator for the *uniform* noise. By gradually ramping up the obstacle density, the BZ forces a smooth structural transition that allows the otherwise abrupt *uniform* model to anchor rotors at the healthy-diseased interface just as efficiently as the inherently correlated *diffuse* mesh. Meanwhile, the elongated architectures maintained their protective profiles, with *interstitial* (OR = 0.42) and *patchy* (OR = 0.16) suppressing global risk.

Visual analysis of the wave dynamics, capturing the interaction between the propagating wavefront and the circular FC boundaries, is illustrated in Fig. 26. The sequential spatial frames reveal that reentrant activity largely remains sequestered within

the FC. Because the hypoxic core suffers from severe APD abbreviation compared to the surrounding healthy myocardium, any wavefront attempting to exit the lesion encounters a massive electrical sink of cells still in their effective refractory period. Consequently, the rotors remain trapped inside the fibrotic boundaries, acting as an ectopic source persistently exciting the surrounding healthy tissue.

6.5 SCENARIO III: VOLUMETRIC PROPAGATION ROUTES

The extension of the homogeneous fibrotic substrate into a 3D volumetric domain fundamentally disrupts the electrophysiological hierarchies observed in planar tissues. The empirical probability curves and vulnerability windows for this scenario are detailed in Fig. 27. Following the established layout, the top panel maps the absolute probability of sustained reentry against fibrosis density, while the bottom Gantt chart quantifies the absolute event occurrences across the effective arrhythmic intervals. To dissect how the reentry probability change depending on the fibre orientation in the same way we did to the other scenarios, we parsed the empirical probabilities by fibre orientation in Fig. 28.

The transition to 3D introduced a systemic rightward shift in the vulnerability windows across all phenotypes. While 2D arrhythmias peaked predominantly between 25% and 40%, 3D events were extensively delayed, emerging only between 60% and 80%. This functional shift perfectly mirrors the displacement of p_c reported in Table 5, where critical boundaries jumped from approximately 0.45 in 2D to approximately 0.88 in 3D. The volumetric space allows the wavefront to exploit more propagation routes, requiring an higher collagen density to achieve the critical level of structural fragmentation necessary to induce wave break. The transition to 3D also induced a systemic contraction of the vulnerability windows when compared to Scenario I, characterized by a universal decrease in p_{tw} (as shown in Table 5) across almost all phenotypes.

Firth's regression analysis (Fig. 29) demonstrated that both *diffuse* (OR = 1.71) and *interstitial* (OR = 1.32) patterns presented significantly higher global risks than the *uniform* reference. Because these spatially correlated patterns maintain intrinsic clustering rules (Moran's $I > 0.22$), they provide just enough contiguous interfacial boundaries to successfully anchor scroll wave while simultaneously maximizing wavefront fractionation.

While the total number of sustained reentries dropped significantly for most patterns in 3D due to the transmural bypass mitigating conduction blocks, there is a notable exception: the *patchy* pattern, which increased its sustained events from 124 in 2D to 150 in 3D, and converged its global risk profile (OR = 1.01) with the *uniform* baseline. This unique dimensional resilience is directly explained by the quantitative descriptors of its morphology. As shown in Table 3, the *patchy* architecture possesses the highest geometric elongation ($AR = 1.310$) and the second largest cluster mass among the textures ($\hat{S} = 0.14\%$). In a 3D syncytium, these massive, elongated collagen strands

act as robust, transmural stabilizing columns. Instead of contorting and self-terminating, scroll waves securely attach to these macro-structures, demonstrating that the malignant arrhythmogenic nature of *patchy* fibrosis is fundamentally a volumetric phenomenon.

These mechanistic hypotheses are visually corroborated by the spatio-temporal wave propagation frames rendered in Fig. 30. The 3D visualizations of the action potential fronts clearly highlight the transmural bypass mechanism, where waves seamlessly navigate over and under the discrete barriers. Furthermore, it visually captures how the fragmented *diffuse* and *interstitial* media force a labyrinthine propagation, while the *patchy* architecture provides solid, elongated walls that firmly anchor the rotating scroll waves.

Figure 22 – Spatio-temporal wave propagation frames in Scenario I. The sequential panels track transmembrane potential showing how wavefronts interact with explicit fibrotic barriers. The *uniform* and *diffuse* structures induce widespread fractionation; *compact* fibrosis stabilizes a single anchored rotor; while *interstitial* and *patchy* architectures constrain conduction to tight corridors, turning the wave into elliptical circuits.

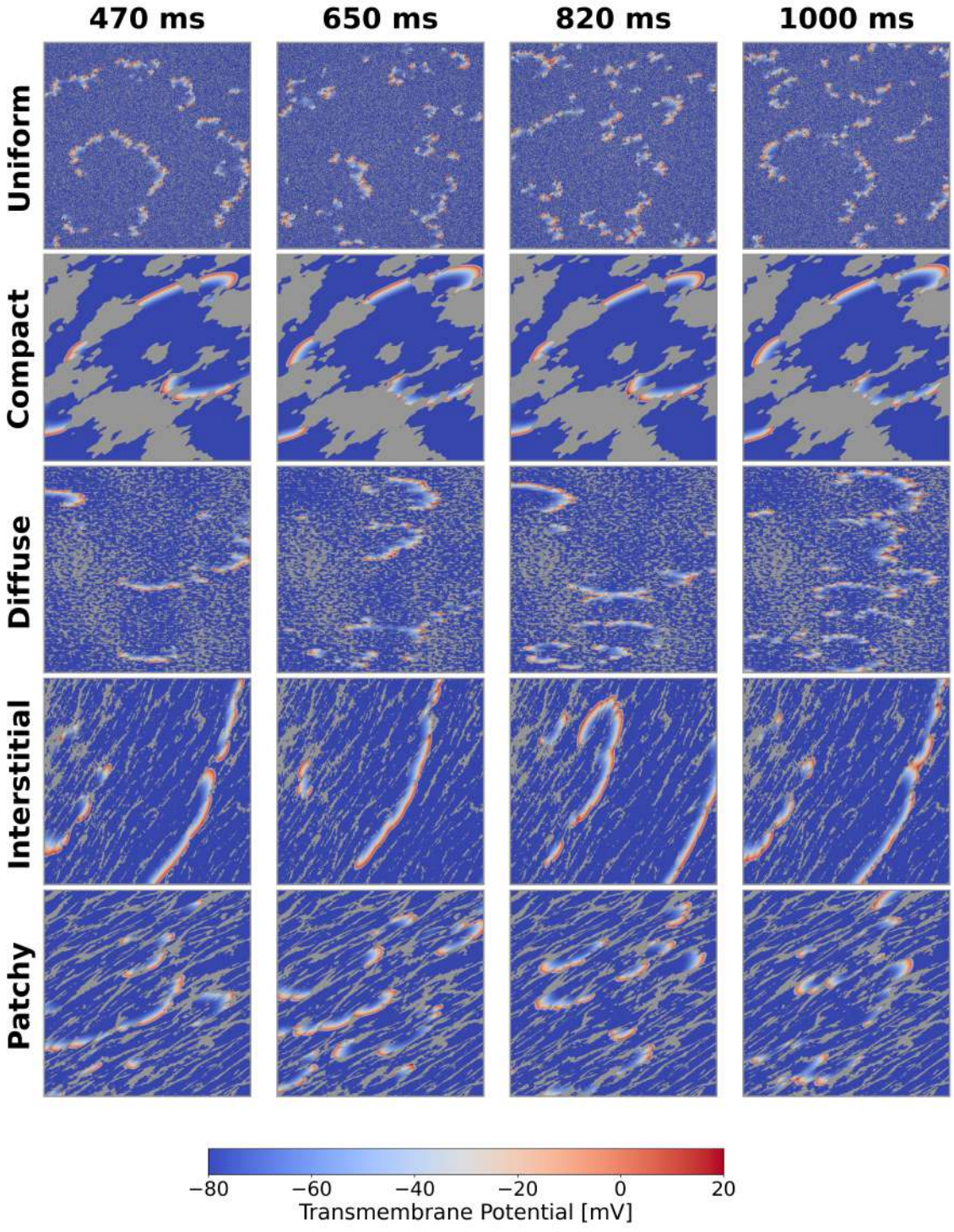

Source: Elaborated by the author (2026).

Figure 23 – Empirical analysis of sustained reentries in Scenario II. (Top) Absolute probability distributions for each structural phenotype. (Bottom) Gantt chart detailing the effective vulnerability windows. The presence of a BZ and healthy myocardium promotes a global reduction in arrhythmogenic incidence and compresses the vulnerability intervals compared to the fully diseased slab of Scenario I. Numbers inside the bars indicate the sustained reentry count per interval.

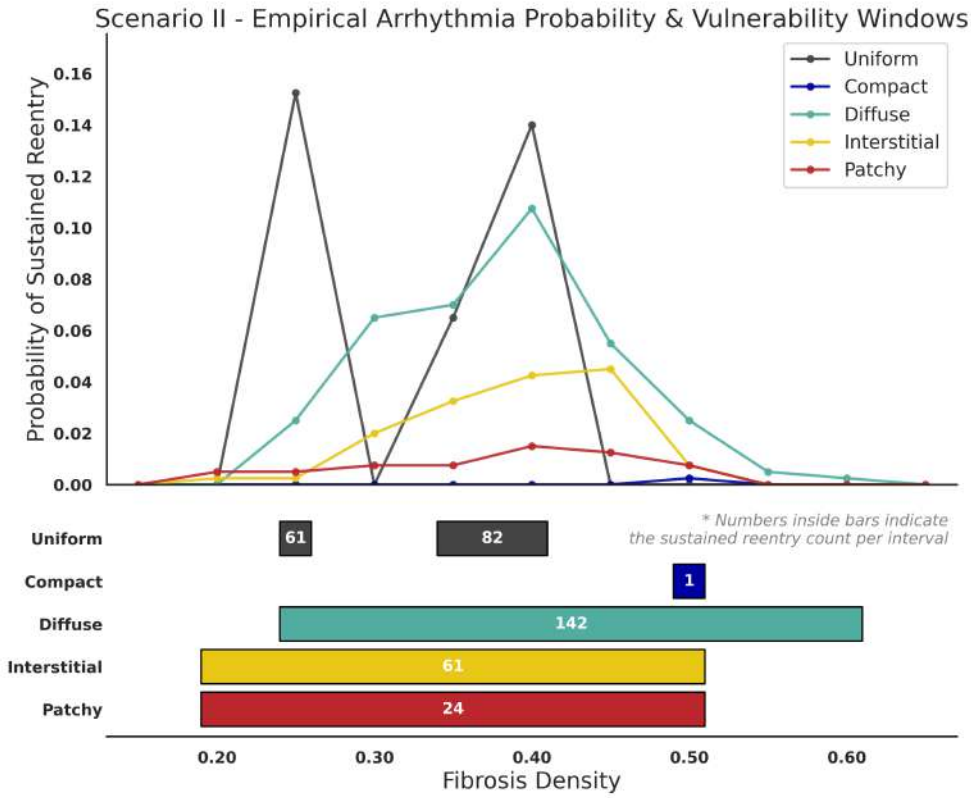

Source: Elaborated by the author (2026).

Figure 24 – Empirical probability of sustained reentry separated by fibre orientation in Scenario II.

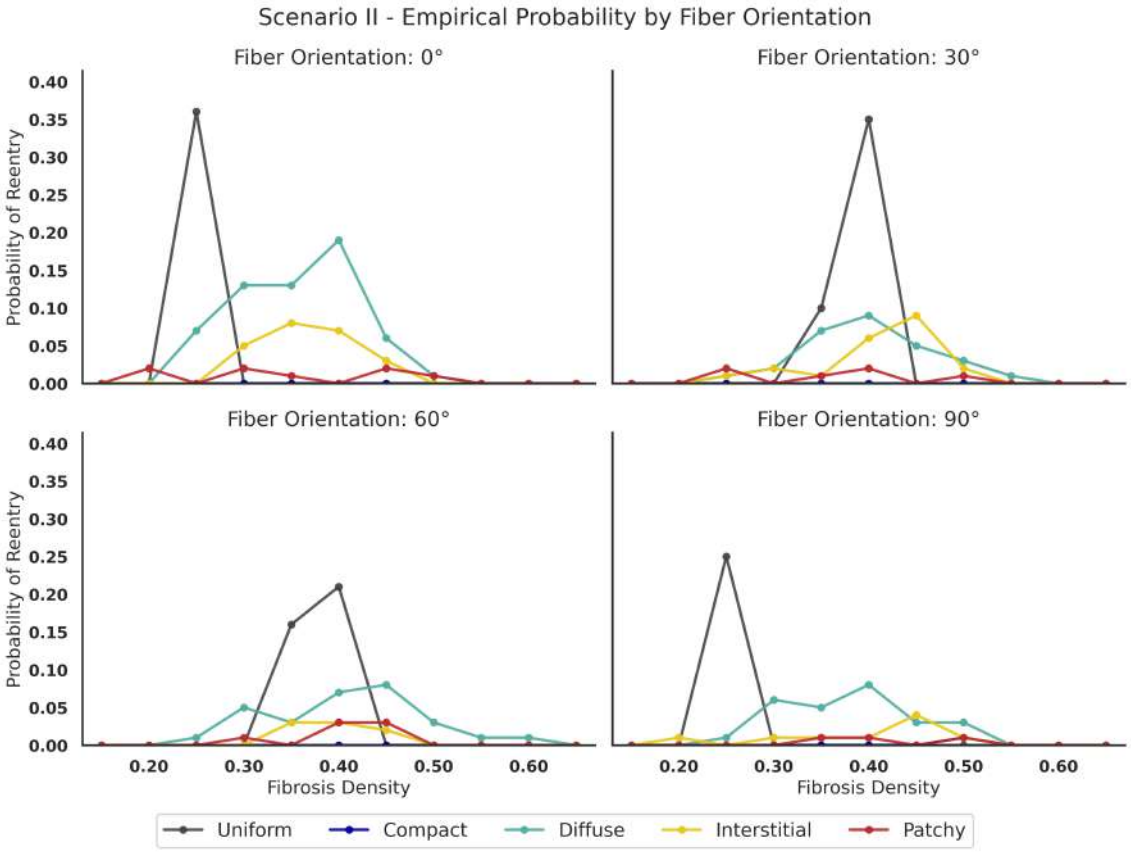

Source: Elaborated by the author (2026).

Figure 25 – Firth's Bias-Reduced Logistic Regression for relative arrhythmia risk in Scenario II. With the *uniform* distribution set as the baseline (OR = 1.00), *diffuse* fibrosis exhibits an identical global risk profile, while *interstitial* (OR = 0.42) and *patchy* (OR = 0.16) architectures manifest strong protective effects.

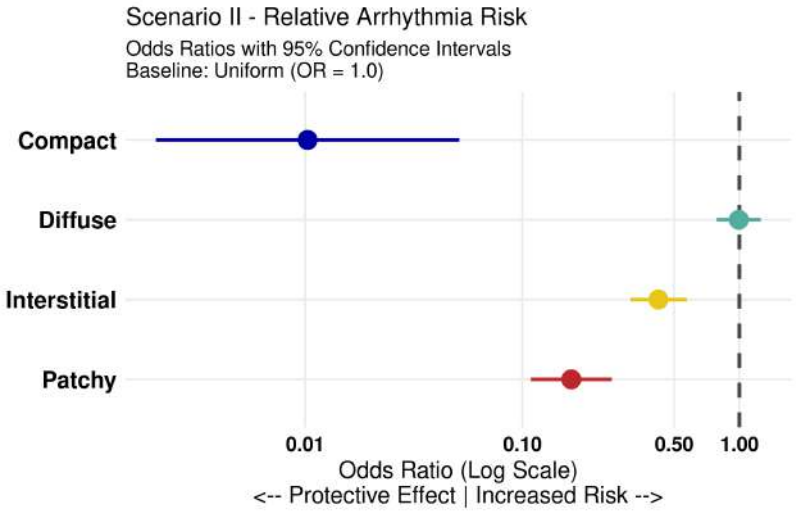

Source: Elaborated by the author (2026).

Figure 26 – Spatio-temporal wave propagation frames in Scenario II. The frames capture the dynamic entry and persistent formation of reentrant circuits within the hypoxic FC. The BZ prevents the wave from easily exiting the lesion by creating a severe source-sink mismatch and functional blocks in the interface with the healthy tissue, helping to keep the reentry spirals inside the fibrotic core boundaries.

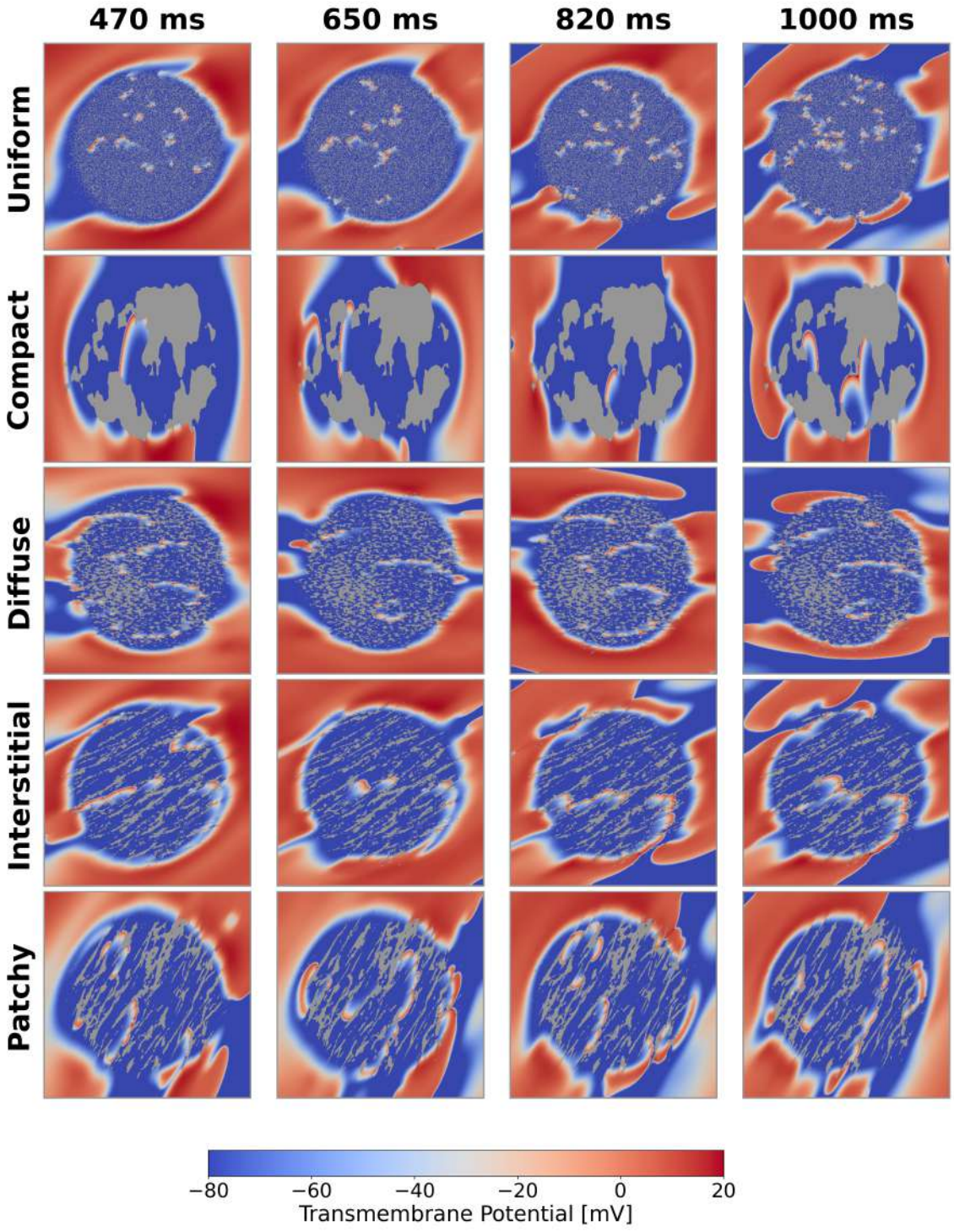

Source: Elaborated by the author (2026).

Figure 27 – Empirical analysis of sustained reentries in Scenario III. (Top) Absolute probability across fibrosis densities. (Bottom) Gantt chart illustrating the effective vulnerability intervals. Compared to 2D domains, all vulnerability windows undergo a systemic rightward shift, reflecting the capacity of the 3D wavefront to bypass structural obstacles. Numbers inside the bars indicate the sustained reentry count per interval.

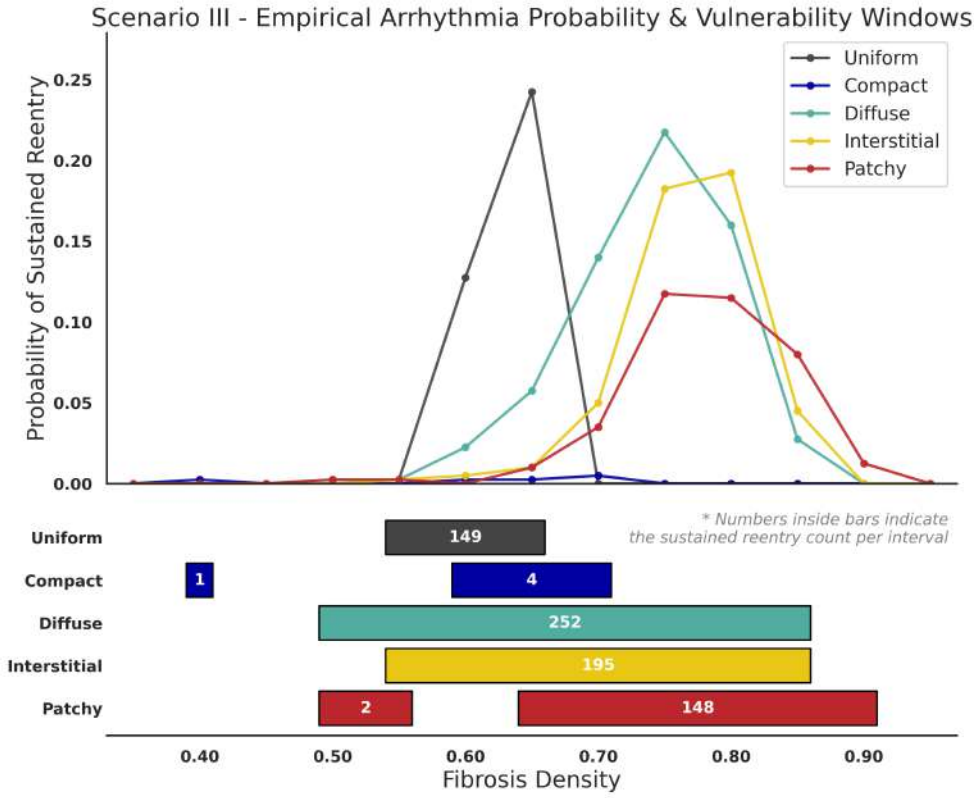

Source: Elaborated by the author (2026).

Figure 28 – Empirical probability of sustained reentry separated by fibre orientation in Scenario III.

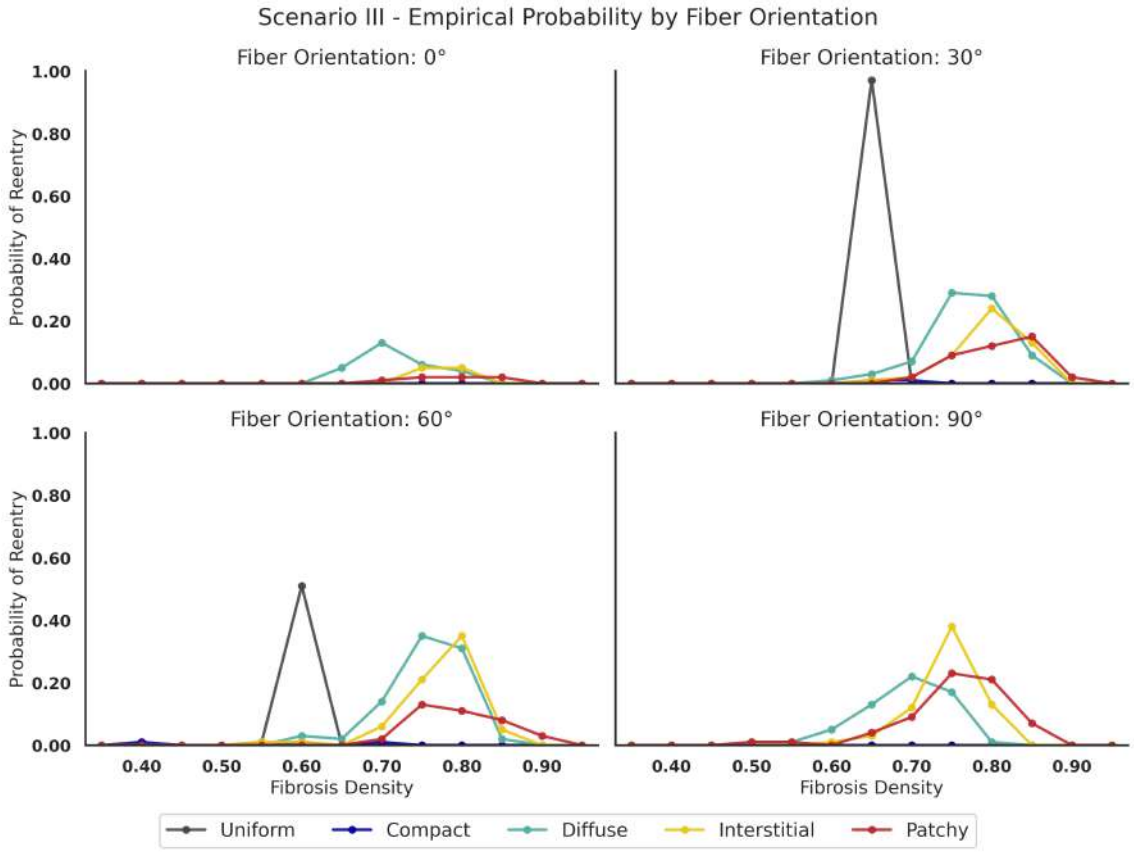

Source: Elaborated by the author (2026).

Figure 29 – Firth's Bias-Reduced Logistic Regression for relative arrhythmia risk in Scenario III. With the *uniform* distribution set as the baseline (OR = 1.00); highly fractionating correlated patterns (*diffuse*, *interstitial*) exhibit higher arrhythmogenic burdens.

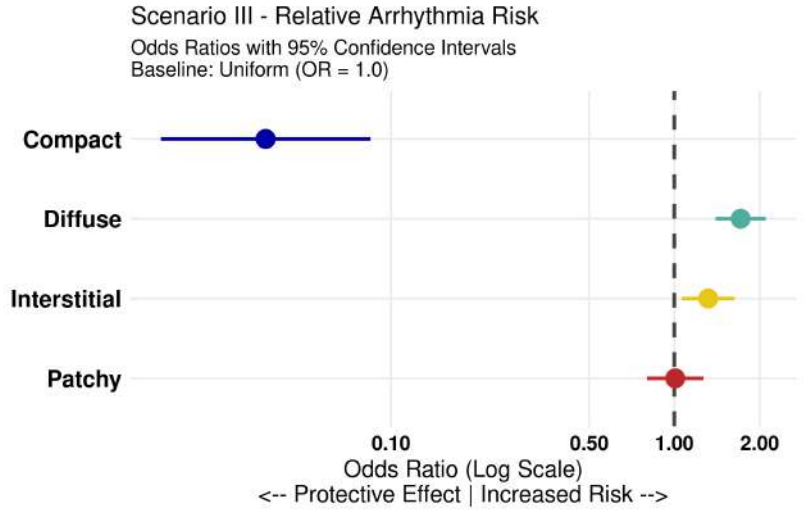

Source: Elaborated by the author (2026).

Figure 30 – Spatio-temporal wave propagation frames in Scenario III. Renders of the volumetric action potential front highlight the transmural bypass mechanism, where the wave utilizes the z-axis to overcome obstacles. The frames reveal the highly fragmented propagation within the *diffuse* pattern and the stabilization of scroll waves around the fibrotic features of the *patchy* architecture.

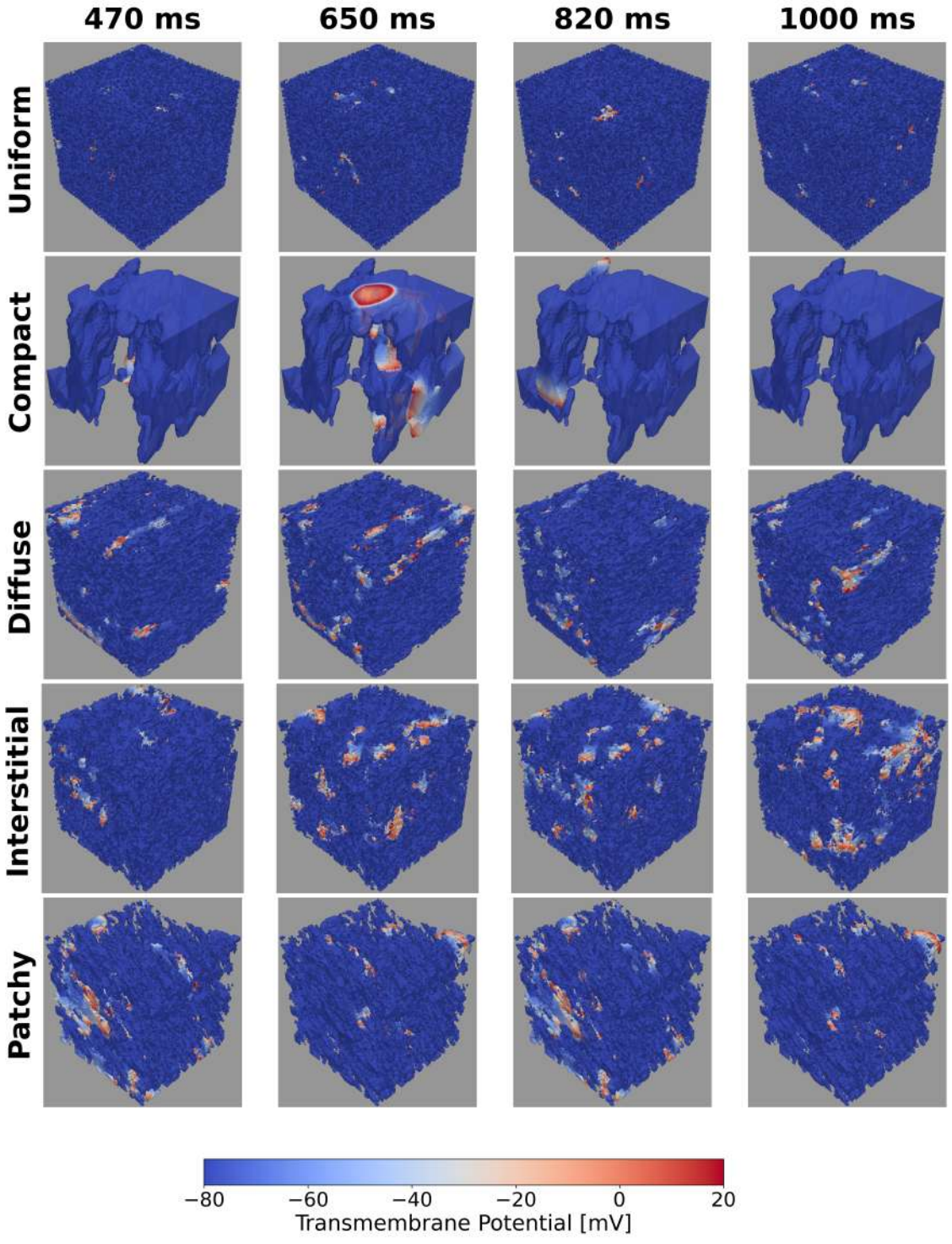

Source: Elaborated by the author (2026).

7 DISCUSSIONS

7.1 METHODOLOGICAL SCALING AND FUNCTIONAL PERCOLATION

As established in Chapter 2, the spatially correlated Perlin microstructures possess quantitative structural properties that are inherently tied to the biological scale of the histological sampling (i.e., millimetre scale). However, resolving complete reentrant circuits around these features requires substantial spatial domains to prevent wave-boundary collisions from prematurely extinguishing the arrhythmia. Given the computational constraints of simulating macroscopic domains (i.e., potential centimetre scale) with a microscopic discretization ($\Delta x = 10$ μm), we employed a geometric spatial scaling. The structural patterns were linearly scaled by a factor of 10 to construct a computationally feasible domain, allowing for a spatial resolution of $\Delta x = 100$ μm in the finite volume solver. This decision, scaling from mm to cm, preserved the topological archetypes of the barriers while allowing the wavefront to interact dynamically with explicit physical boundaries. We explicitly acknowledge alternative frameworks, such as homogenisation techniques (LAWSON et al., 2023; LAWSON et al., 2024; GOKHALE et al., 2018; FARQUHAR et al., 2022), that have been applied to incorporate microscopic structures into a macro-scale problem using different approaches. However, as our objective was to investigate the dynamic of macroscopic spiral waves against discrete structural features, scaling the explicit obstacles ensures the preservation of the topological mechanisms responsible for wave fractionation.

As quantified in Tables 4 and 5, the analysis of structural percolation revealed that *compact* and *patchy* phenotypes significantly widen the transition window (p_{tw}). According to percolation theory, this attenuation is driven not only by spatial autocorrelation (Moran's I) but mainly by the macroscopic mass of the generated obstacles, quantified by $\hat{S}$ (Table 2). By aggregating fibrosis into massive clusters (high $\hat{S}$), these architectures preserve large tracts of viable myocardium that effectively delay the complete topological collapse of the network. In contrast, the scattered micro-obstacles of the *uniform* distribution (lowest $\hat{S}$) precipitate a nearly instantaneous failure. This behaviour aligns directly with established principles for percolation in complex media, often discussed in the context of finite-size scaling (STAUFFER; AHARONY, 2018; SAHIMI; HUNT, 2021) and the Harris criterion (HARRIS, 1974; STAUFFER; AHARONY, 2018; SAHIMI; HUNT, 2021). Specifically, finite-size scaling dictates that the abruptness of a theoretical phase transition is intrinsically smeared by the boundaries of a finite physical computational domain. Concurrently, the Harris criterion posits that introducing spatially correlated disorder, such as the clusters generated by the Perlin noise, fundamentally alters the critical dynamics of the system. Because the obstacle density fluctuates wildly at the macroscopic level, different local regions of the tissue undergo percolation at completely different collagen

amount, stretching the global transition curve. Biologically, this implies that rather than a binary switch between healthy conduction and total block, correlated and clustered fibrotic deposition creates an extended critical regime of fractionated conduction.

An apparent biophysical paradox emerges when contrasting the arrhythmogenic peaks (Appendix Table 6 for 2D and Appendix Table 8 for 3D) with the strict structural p_c (Table 4 for 2D and Table 5 for 3D). While theoretical studies suggest that the maximum wave meandering occurs close to p_c (ALONSO; BÄR, 2013; ALONSO; SANTOS; BÄR, 2016; VIGMOND et al., 2016), our GAM analysis reveals peaks of reentry probability at lower densities. To disentangle this behaviour, it is necessary to understand that this leftward shift underscores the distinction between structural and functional percolation in excitable media (SAHIMI, 1994; SACHETTO; ALONSO; SANTOS, 2018). Because our medium is coupled with severe acute hypoxia, the wavefront fails to propagate through narrow anatomical isthmuses that are geometrically continuous but functionally impassable due to insufficient electrotonic driving force (KLÉBER; RUDY, 2004; GOKHALE et al., 2018).

Interestingly, despite this functional shift, the hierarchy of vulnerability remains perfectly conserved relative to the structural limits. Specifically, in 2D, for the *diffuse*, *interstitial*, and *patchy* phenotypes, the descending order of their structural percolation thresholds ($p_c = 0.476, 0.458$, and 0.414, respectively; Table 4) is identical to the hierarchical sequence of their peak arrhythmogenic densities (35.8%, 33.3%, and 29.4%, respectively; Appendix Table 6). The continuous non-linear probability profiles and penalized regression splines modeled by the GAM framework for these active phenotypes are illustrated in Appendix Fig. 35. In 3D, that same behaviour, but with a different order (*patchy* > *interstitial* > *diffuse*), is observed (Table 5 and Appendix Table 8). This strict alignment indicates that the intrinsic topological robustness of the fibrotic network dictates the sequence of electrophysiological failure. The continuous and smooth non-linear profiles given by the GAM for 3D are shown in Appendix Fig. 37.

7.2 TOPOLOGICAL DRIVERS OF ARRHYTHMOGENESIS

The empirical results from Scenario I (Fig. 19) establish that arrhythmic risk is driven by a delicate balance between structural fragmentation and contiguous viable pathways (CHERRY; FENTON; JR, 2012). From a biophysical perspective, the geometric scaling of D_f (reaching 1.854 and 1.816 for *uniform* and *diffuse* in Table 2) provides early indicators of these tendencies. Media approaching space-filling limits (*uniform* and *diffuse*) introduce heterogeneities that continuously fractionate wavefronts. However, while *uniform* noise possesses extreme microscopic fragmentation, it often fails to provide conduction pathways long enough to sustain circuits. Conversely, the correlated *diffuse* pattern introduces sufficient interfacial boundaries to induce wave break, while its spatial correlation

preserves micro-corridors large enough to anchor high-frequency rotors (FENTON et al., 2002; CHERRY; FENTON; JR, 2012), explaining its position as the most arrhythmogenic planar pattern on our simulations (Fig. 21).

On the other hand, topological connectivity (β_1 loops) and structural elongation (AR) explains the protective nature of highly anisotropic patterns. Biologically, β_1 loops may represent anatomical reentrant circuits where myocardial strands completely encircle fibrotic obstacles. In 2D, the positive difference between β_0 and β_1 of *interstitial* and *patchy* patterns (Table 2) indicates topologies dominated by isolated islands (β_0) with longer conductive loops (β_1). When a wavefront collides with these macroscopic barriers, it is forcibly diverted. By forcing a zigzag conduction pattern, these specific architectures impose localized delays but maintain spatial wave cohesion (BAKKER et al., 1993), significantly restricting the continuous fractionation required for fibrillation, which was visually confirmed by the elliptical trajectories in Fig. 22.

The divergence between *interstitial* and *patchy* architectures can be attributed to their macroscopic aggregation (MYKLEBUST; MALECKAR; AREVALO, 2024) ($\hat{S}$). Biologically, *patchy* fibrosis forms massive dense macro-nodules that act as regional insulators. *Interstitial* fibrosis distributes its collagen into finer septa; this fine-grained labyrinth maintains a higher density of viable parallel corridors, slightly increasing the probability that a fractionated wavelet will navigate through the obstacle course and find a viable reentrant loop (BALABAN et al., 2020).

The possible correlation observed between these topological metrics (D_f, β_1, AR) and the electrophysiological outcomes points toward a horizon of a possible predictive value in computational cardiology. It suggests the feasibility of stratifying arrhythmogenic risk using geometric and structural metrics as an informative tool. By feeding these quantitative descriptors into machine learning classifiers, it may become possible to reliably predict wave fractionation and rotor stability directly from tissue imaging, circumventing the massive computational costs of executing thousands of electrophysiological simulations for patient-specific risk assessments.

7.3 BOUNDARY DYNAMICS AND SOURCE-SINK MISMATCHES

The overall attenuation of absolute risk and the compression of vulnerability intervals (Fig. 23) in Scenario II appears to contradict clinical literature, which often identifies the BZ as a primary catalyst for arrhythmogenesis (PANDIT; JALIFE, 2013). However, this divergence is rooted in the geometric constraints of our computational setup rather than a failure of the physiological mechanism. The transition from a fully remodeled 16 cm^2 domain (Scenario I) to a localized configuration reduces the diseased area to approximately 9 cm^2 (FC plus BZ). As emphasized by the critical mass hypothesis (HARTLEY et al., 2021), reducing the contiguous electrical mass limits the available spatial substrate, thereby

decreasing the probability of accommodating the minimum path length required to sustain a rotating spiral wave. Therefore, while the absolute number of events decreased, the mechanisms of wave anchoring observed in this scenario provide deep insights into focal lesion dynamics.

This boundary block is exacerbated by repolarization dispersion. As established, severe hypoxia abbreviates the APD within the FC to approximately 21 ms, while the surrounding healthy tissue maintains a physiological APD of approximately 330 ms (SACHETTO; ALONSO; SANTOS, 2018). Consequently, any wavefront that overcomes the source-sink barrier and exits the FC instantly collides with healthy cells still within their effective refractory period. For an arrhythmia to sustain itself in this scenario, the rotor must remain strictly anchored within the internal micro-architecture of the FC for a duration sufficient to allow the external healthy boundaries to repolarize, a restrictive dynamic that extinguishes the majority of transient wave breaks.

Nevertheless, the boundary interactions provide deep biophysical insights. The convergence of global risk between *diffuse* and *uniform* patterns in Scenario II (Fig. 25) suggests that the gradual structural gradient of the BZ acts as an artificial spatial correlator for the *uniform* noise. By slowly ramping up the probability of non-conducting sites, the gradient physically forces a smooth transition zone, allowing the abrupt *uniform* model to anchor rotors at the interface with the same efficiency as the naturally correlated *diffuse* mesh.

Furthermore, visual analysis of the simulations confirmed that structural obstacles frequently spawned rotors inside the FC (Fig. 26). However, as the spiral wavefront attempted to propagate outward from the poorly coupled FC into the excitable healthy myocardium, it encountered an abrupt geometric expansion. This tissue boundary acts as a massive electrical sink. The small source current generated by the surviving hypoxic FC myocytes struggles to depolarize the surrounding healthy tissue, creating a severe source-sink mismatch specifically at the exit of the lesion that promotes localized conduction delays and unidirectional block (KLÉBER; RUDY, 2004; CHERRY; FENTON, 2011; CIACCIO et al., 2018). Consequently, the reentrant circuits become physically trapped within the boundaries of the FC. Because these rotors are strictly confined to the internal micro-architecture of this smaller diseased area, they have significantly less spatial mass to anchor and stabilize compared to a fully fibrotic domain. This spatial restriction is the precise reason why we observe a marked reduction in overall arrhythmic risk and much narrower vulnerability windows when evaluating localized lesions.

Furthermore, this localized geometric delay interacts dynamically with the intrinsic electrophysiological restitution properties of the tissue. As the wavefront slows down at the narrow exits of the fibrotic corridors due to the source-sink mismatch, this localized drop in CV exacerbates the existing repolarization heterogeneities between the hypoxic

core and the healthy border. This interaction between anatomical tortuosity and dynamic wave restitution provides the exact substrate required for unidirectional block, ensuring that reentries only survive if they find perfectly synchronized recovery pathways within the core.

7.4 VOLUMETRIC COMPLEXITY AND TRANSMURAL BYPASS

The leap to 3D volumetric domains fundamentally disrupted the structural hierarchies observed in planar tissues (FENTON; KARMA, 1998). The delayed onset of arrhythmogenesis (shifting to 60%–90% densities in Fig. 27) and the inversion of TCE (Table 5) directly reflect transmural bypass effects. In 3D, the wavefront leverages out-of-plane routes to simply propagate between the elongated walls of *patchy* and *interstitial* patterns, a volumetric bypass mechanism illustrated through sequential simulation frames across all phenotypes in Fig. 30.

Conversely, the fragmented dispersion of *uniform* and *diffuse* obstacles (characterized by $D_f > 2.66$ in Table 3) behaves as a highly porous volumetric sponge. Biologically, every microscopic division of the wavefront as it navigates this 3D sponge increases the electrotonic load on viable myocytes, explaining why these scatter patterns produce the highest conduction delays (lowest TCE) in 3D.

Regarding the *uniform* pattern in 3D, despite imposing the worst TCE, it generated fewer reentries than correlated patterns (Fig. 29). We hypothesize this disconnect originates from the mechanics of scroll waves, which possess inherent tension (BIKTASHEV; HOLDEN; ZHANG, 1994) and actively seek continuous macroscopic boundaries to anchor (FENTON; KARMA, 1998; CHERRY; FENTON, 2008; MAJUMDER; NAYAK; PANDIT, 2011). Because the *uniform* medium lacks contiguous macroscopic circuits ($\hat{S} < 0.01\%$ and huge β_1 in Table 3), its transient wave breaks rapidly self-terminate.

In contrast, the dense macro-nodules of the *patchy* architecture (highest AR and highest active $\hat{S}$ in 3D) provide ideal, robust stabilization columns for scroll waves, explaining its unique resilience and increased event count in the restricted 3D space. Notably, this dimensionality-dependent amplification offers a compelling mechanistic bridge to clinical and histological observations. While our generalized planar models identified *diffuse* fibrosis as presenting the highest absolute event incidence, de Jong *et al.* (JONG et al., 2011) classified *patchy* fibrosis as the most highly arrhythmogenic substrate in biological tissue. Although our idealized procedural framework lacks the complete anatomical fidelity of a real human ventricle, the unique capacity of the *patchy* architecture to actively increase its arrhythmogenic burden when translated to 3D suggests that its clinically observed malignancy is essentially a volumetric phenomenon. It relies on transmural macro-structures to stabilize three-dimensional scroll waves that would otherwise extinguish in thinner, or more fragmented, tissue matrices.

7.5 LIMITATIONS AND FUTURE WORKS

Several methodological limitations of this study must be explicitly acknowledged. From a computational and structural perspective, a primary constraint lies in the spatial discretization utilized for the simulations. We employed a resolution of $100\,\mu m$, meaning that spatial features, including cluster volumes, obstacle tortuosity, and the thickness of the BZ layers, were inherently defined in terms of discrete cellular voxels. Consequently, the morphological thresholds and percolation dynamics observed are sensitive to this specific spatial grid and may not perfectly capture the continuous nature of histological collagen fibres at a finer scale. Additionally, all simulated domains assumed a uniform fibre orientation. In realistic cardiac anatomy, myofibres exhibit a continuous transmural rotation, an anisotropic feature that significantly influences three-dimensional scroll wave dynamics (FENTON; KARMA, 1998; MAJUMDER; NAYAK; PANDIT, 2011). Also, 3D samples considered a simplified fibrosis distribution, not taking into account a histological transmural fibrosis profile (RAVELLI et al., 2023). Furthermore, regarding the stimulation protocol, arrhythmic events were initiated by a single planar wavefront; employing standard premature protocols (e.g., S1-S2) or rapid pacing could uncover alternative vulnerability dynamics. Specifically, our current risk analysis has predominantly focused on the onset of reentry directly induced by the structural fragmentation of a stable wavefront. By evaluating wave break initiation rather than pure anchorage, we may underestimate the arrhythmogenic peril of certain spatial configurations. For example, while *compact* fibrosis exhibits a protective profile against initiating wave breaks from a single planar stimulus, it is highly plausible that such dense barriers act as major risk factors for anchoring and stabilizing pre-existing dysfunctional activation patterns originating from premature ectopic beats.

Physiologically, our investigations were conducted using a single human ventricular cellular model. Given the distinct ionic currents and the clinical prevalence of structural arrhythmias in other cardiac chambers, such as atrial fibrillation in the atria, future evaluations should incorporate atrial dynamics. Moreover, our metabolic framework induced APD abbreviation solely via ATP depletion under a single state of acute hypoxia. Exploring a broader metabolic spectrum, including hyperkalemia and acidosis (SHAW; RUDY, 1997; FERRERO; GONZALEZ-ASCASO; MATAS, 2023), would yield a more comprehensive electrophysiological landscape. Finally, fibroblasts were modeled as purely non-conductive obstacles. In biological tissue, myofibroblasts may actively modulate local electrophysiology (CAMELLITI; BORG; KOHL, 2005; MIRAGOLI; GAUDESIUS; ROHR, 2006; MIRAGOLI; SALVARANI; ROHR, 2007; SIMON-CHICA; LOEWE; KOHL, 2026; ROG-ZIELINSKA et al., 2016; GOURDIE; DIMMELER; KOHL, 2016; WANG et al., 2023) and the release of paracrine signalling molecules, which can significantly alter tissue excitability.

Additionally, this study centred its statistical analyses on four discrete histological classifications (*compact*, *diffuse*, *interstitial*, and *patchy*). In biological reality, these phenotypes frequently coexist and blend, forming a continuous and heterogeneous spectrum of structural remodeling rather than isolated bins. The current categorical approach, while pivotal for establishing baseline behaviours, inherently simplifies this geometric complexity. Future investigations must disentangle this continuum by leveraging non-linear statistical models, such as GAMs, to map arrhythmogenic probabilities directly as a function of the continuous structural metrics (D_f, β_n, AR, I), bypassing the need for discrete phenomenological labels altogether.

These limitations outline clear paths for future research. Extending the current computational pipeline to incorporate multi-physics models that couple electrophysiology with cardiac mechanics will provide a more holistic understanding of fibrotic heart failure. Ultimately, bridging the gap between our micro-scale topological findings and macroscopic clinical applications represents the natural final step of this pipeline (NIEDERER; LUMENS; TRAYANOVA, 2019; TRAYANOVA et al., 2024). Future work will focus on the application of mathematical homogenization techniques. By upscaling the effective conduction properties derived from these detailed microscopic patterns, it will be possible to incorporate histology-based textural behaviours into whole-heart, patient-specific geometries derived from low-resolution clinical imaging (e.g., LGE-CMR) without incurring prohibitive computational costs (TRAYANOVA et al., 2024; O'HARA et al., 2022; AREVALO et al., 2016). This multi scale approach aims to refine personalized computational diagnostics and improve the mechanistic accuracy of sudden cardiac death risk assessments.

8 CONCLUSIONS

In this study, we systematically investigated the arrhythmogenic mechanisms driven by distinct fibrotic patterns under acute hypoxic conditions. To achieve this, we centred our computational framework on four histologically inspired structural classifications: *compact*, *diffuse*, *interstitial*, and *patchy* fibrosis, alongside an uncorrelated *uniform* noise baseline. We adopted a Perlin noise-based generator to synthesize these patterns across computational domains and we introduced two major methodological advancements to this generator. First, we implemented an iterative *composition* generation mode designed to preserve the specific morphological characteristics of the fractionated phenotypes even at elevated fibrosis densities. Second, we developed a BZ support in the generator, allowing the creation of spatial density gradients around FC.

To systematically evaluate the risk of sustaining reentries, we organized our study into three distinct experimental scenarios: 2D homogeneous substrates, 2D domains featuring localized FCs and their BZs, and 3D homogeneous tissues. Across these configurations, we deployed electrophysiological simulations governed by the monodomain formulation to explicitly capture dynamic wave propagation. Furthermore, the integration of Firth's logistic regression and GAM allowed us to translate the discrete simulation outcomes into continuous risk profiles.

Quantitatively, our morphological and topological characterizations yielded distinct values across the evaluated metrics (such as $\hat{S}$, D_f, Betti numbers, AR, and Moran's I) for each fibrotic microstructure. This variation allowed us to effectively differentiate and classify the generated architectures. We found that phenotype-specific spatial correlations and collagen clustering effectively smeared the abrupt transition window characteristic of the *uniform* white noise. This attenuation significantly extended p_{tw}, indicating that correlated fibrosis degrades the tissue network gradually as density increases. Moreover, p_c and TCE varied substantially among patterns, confirming that structural architecture directly dictates both the absolute limits of conduction and the geometric retardation imposed on the wavefront.

Electrophysiologically, we observed some correlations between the quantified structural and percolation metrics and the simulated outputs. Each fibrosis phenotype governed arrhythmia probabilities through distinct wave-structure interactions. Dispersed patterns with high space-filling complexity (high D_f), such as *diffuse* fibrosis, significantly fractionated the wavefront, creating microscopic isthmuses that maximized arrhythmogenic risk in our scenarios. Conversely, patterns that aggregated into elongated parallel corridors (e.g., *interstitial* and *patchy*) forced the wave into zigzag pathways, exhibiting a protective effect against continuous wave break. Consequently, the dynamics of wave fractionation, rotor anchoring, and zigzag conduction were mostly related to the underlying structural

descriptors of each phenotype.

When evaluating localized FCs with BZ (Scenario II), the restricted spatial mass of the diseased tissue reduced the absolute incidence of sustained reentries. However, the structural gradient of the BZ functionally transformed the core into a persistent ectopic generator. It actively modulated arrhythmogenesis by exacerbating source-sink mismatches and functional blocks at the healthy-diseased interface, facilitating rotor anchoring and stabilization at the lesion's core. Finally, tissue dimensionality altered these arrhythmogenic mechanisms. In Scenario III, the transition to 3D volumetric domains introduced transmural bypass routes that attenuated planar conduction blocks observed in Scenario I, significantly increasing the percolation thresholds and inducing a systemic rightward shift in peak vulnerability densities. Notably, the leap to 3D fundamentally disrupted the risk hierarchy observed in 2D. While the other patterns exhibited a reduction on the total number of sustained reentries, the elongated and dense nodules of the *patchy* architecture provided robust stabilizing columns for three-dimensional scroll wave, actively increasing its arrhythmogenic burden.

Our analyses established a direct link between micro-scale geometric clustering, structural percolation, and electrical wave propagation. This work demonstrates that stratifying arrhythmic risk and predicting complex wavefront behaviours can potentially be achieved by evaluating fundamental topological metrics, paving the way for diagnostic frameworks that bypass the exclusive reliance on computationally demanding biophysical simulations.

8.1 DECLARATION OF GENERATIVE AI USE

During the preparation of this work, Artificial Intelligence was employed to aid in the generation of data analysis plots, support the organization and refactoring of the underlying codebase, and assist with English translation, grammar correction, and overall text refinement. All AI-assisted outputs were rigorously reviewed, validated, and edited by the authors, who assume full responsibility for the final content, integrity, and original ideas presented in this manuscript.

REFERENCES

LAWSON, B. A. et al. Perlin noise generation of physiologically realistic cardiac fibrosis. *Medical Image Analysis*, Elsevier, v. 98, p. 103240, 2024.

CAMELLITI, P.; BORG, T. K.; KOHL, P. Structural and functional characterisation of cardiac fibroblasts. *Cardiovascular research*, Elsevier Science, v. 65, n. 1, p. 40–51, 2005.

TALMAN, V.; RUSKOAHO, H. Cardiac fibrosis in myocardial infarction—from repair and remodeling to regeneration. *Cell and tissue research*, Springer, v. 365, n. 3, p. 563–581, 2016.

FRANGOGIANNIS, N. G. Cardiac fibrosis. *Cardiovascular research*, Oxford University Press, v. 117, n. 6, p. 1450–1488, 2021.

GLASHAN, C. A. et al. Whole human heart histology to validate electroanatomical voltage mapping in patients with non-ischaemic cardiomyopathy and ventricular tachycardia. *European heart journal*, Oxford University Press, v. 39, n. 31, p. 2867–2875, 2018.

MARUYAMA, K.; IMANAKA-YOSHIDA, K. The pathogenesis of cardiac fibrosis: a review of recent progress. *International journal of molecular sciences*, MDPI, v. 23, n. 5, p. 2617, 2022.

BOER, R. A. D. et al. Towards better definition, quantification and treatment of fibrosis in heart failure. a scientific roadmap by the committee of translational research of the heart failure association (hfa) of the european society of cardiology. *European journal of heart failure*, Oxford University Press, v. 21, n. 3, p. 272–285, 2019.

ZENG, L. et al. Ubiquitin proteasome system in cardiac fibrosis. *Journal of Advanced Research*, Elsevier, 2024.

GULATI, A. et al. Association of fibrosis with mortality and sudden cardiac death in patients with nonischemic dilated cardiomyopathy. *Jama*, American Medical Association, v. 309, n. 9, p. 896–908, 2013.

LUNDE, I. G. et al. Myocardial fibrosis from the perspective of the extracellular matrix: Mechanisms to clinical impact. *Matrix Biology*, Elsevier, v. 134, p. 1–22, 2024.

VERHEULE, S.; SCHOTTEN, U. Electrophysiological consequences of cardiac fibrosis. *Cells*, MDPI, v. 10, n. 11, p. 3220, 2021.

DARBY, I. A.; HEWITSON, T. D. Hypoxia in tissue repair and fibrosis. *Cell and tissue research*, Springer, v. 365, n. 3, p. 553–562, 2016.

BRADLEY, T. D.; FLORAS, J. S. Obstructive sleep apnoea and its cardiovascular consequences. *The Lancet*, Elsevier, v. 373, n. 9657, p. 82–93, 2009.

YEGHIAZARIANS, Y. et al. Obstructive sleep apnea and cardiovascular disease: a scientific statement from the american heart association. *Circulation*, Lippincott Williams & Wilkins Hagerstown, MD, v. 144, n. 3, p. e56–e67, 2021.

MARIN-NETO, J. A. et al. Pathogenesis of chronic chagas heart disease. *Circulation*, Lippincott Williams & Wilkins, v. 115, n. 9, p. 1109–1123, 2007.

TSCHÖPE, C. et al. Myocarditis and inflammatory cardiomyopathy: current evidence and future directions. *Nature reviews cardiology*, Nature Publishing Group UK London, v. 18, n. 3, p. 169–193, 2021.

SACHETTO, R.; ALONSO, S.; SANTOS, R. W. D. Killing many birds with two stones: hypoxia and fibrosis can generate ectopic beats in a human ventricular model. *Frontiers in Physiology*, Frontiers Media SA, v. 9, p. 764, 2018.

OLIVEIRA, R. S. et al. Ectopic beats arise from micro-reentries near infarct regions in simulations of a patient-specific heart model. *Scientific reports*, Nature Publishing Group UK London, v. 8, n. 1, p. 16392, 2018.

SHAW, R. M.; RUDY, Y. Electrophysiologic effects of acute myocardial ischemia: a mechanistic investigation of action potential conduction and conduction failure. *Circulation research*, Lippincott Williams & Wilkins, v. 80, n. 1, p. 124–138, 1997.

ZHAO, Y. et al. Hypoxia-induced signaling in the cardiovascular system: pathogenesis and therapeutic targets. *Signal transduction and targeted therapy*, Nature Publishing Group UK London, v. 8, n. 1, p. 431, 2023.

WINFREE, A. T. Varieties of spiral wave behavior: An experimentalist's approach to the theory of excitable media. *Chaos: An Interdisciplinary Journal of Nonlinear Science*, American Institute of Physics, v. 1, n. 3, p. 303–334, 1991.

ALONSO, S.; SANTOS, R. W. D.; BÄR, M. Reentry and ectopic pacemakers emerge in a three-dimensional model for a slab of cardiac tissue with diffuse microfibrosis near the percolation threshold. *PloS one*, Public Library of Science San Francisco, CA USA, v. 11, n. 11, p. e0166972, 2016.

ALONSO, S.; BÄR, M.; ECHEBARRIA, B. Nonlinear physics of electrical wave propagation in the heart: a review. *Reports on Progress in Physics*, IOP Publishing, v. 79, n. 9, p. 096601, 2016.

MCDOWELL, K. S. et al. Susceptibility to arrhythmia in the infarcted heart depends on myofibroblast density. *Biophysical journal*, Elsevier, v. 101, n. 6, p. 1307–1315, 2011.

MORITA, N. et al. Increased susceptibility of aged hearts to ventricular fibrillation during oxidative stress. *American Journal of Physiology-Heart and Circulatory Physiology*, American Physiological Society Bethesda, MD, v. 297, n. 5, p. H1594–H1605, 2009.

NGUYEN, T. P.; QU, Z.; WEISS, J. N. Cardiac fibrosis and arrhythmogenesis: the road to repair is paved with perils. *Journal of molecular and cellular cardiology*, Elsevier, v. 70, p. 83–91, 2014.

BALABAN, G. et al. Fibrosis microstructure modulates reentry in non-ischemic dilated cardiomyopathy: insights from imaged guided 2d computational modeling. *Frontiers in physiology*, Frontiers Media SA, v. 9, p. 1832, 2018.

KAWARA, T. et al. Activation delay after premature stimulation in chronically diseased human myocardium relates to the architecture of interstitial fibrosis. *Circulation*, Lippincott Williams & Wilkins, v. 104, n. 25, p. 3069–3075, 2001.

JONG, S. D. et al. Fibrosis and cardiac arrhythmias. *Journal of cardiovascular pharmacology*, LWW, v. 57, n. 6, p. 630–638, 2011.

TUSSCHER, K. H. T.; PANFILOV, A. V. Influence of diffuse fibrosis on wave propagation in human ventricular tissue. *Europace*, Oxford University Press, v. 9, n. suppl_6, p. vi38–vi45, 2007.

MYKLEBUST, L.; MALECKAR, M. M.; AREVALO, H. Fibrosis modeling choice affects morphology of ventricular arrhythmia in non-ischemic cardiomyopathy. *Frontiers in Physiology*, Frontiers Media SA, v. 15, p. 1370795, 2024.

DOKUCHAEV, A.; PANFILOV, A. V.; SOLOVYOVA, O. Myocardial fibrosis in a 3d model: Effect of texture on wave propagation. *Mathematics*, Mdpi, v. 8, n. 8, p. 1352, 2020.

DISERTORI, M.; MASÈ, M.; RAVELLI, F. Myocardial fibrosis predicts ventricular tachyarrhythmias. *Trends in cardiovascular medicine*, Elsevier, v. 27, n. 5, p. 363–372, 2017.

MASÈ, M. et al. Systematic in-silico evaluation of fibrosis effects on re-entrant wave dynamics in atrial tissue. *Scientific Reports*, Nature Publishing Group UK London, v. 14, n. 1, p. 11427, 2024.

OKENOV, A. et al. Analysis and generation of the fibrosis textures based on histology data of the human hearts with non-ischemic cardiomyopathy. *Physics in Medicine & Biology*, IOP Publishing, v. 70, n. 13, p. 135002, 2025.

BAKKER, J. D. et al. Slow conduction in the infarcted human heart.'zigzag'course of activation. *Circulation*, v. 88, n. 3, p. 915–926, 1993.

KUDRYASHOVA, N. et al. Self-organization of conducting pathways explains electrical wave propagation in cardiac tissues with high fraction of non-conducting cells. *PLoS computational biology*, Public Library of Science San Francisco, CA USA, v. 15, n. 3, p. e1006597, 2019.

NEZLOBINSKY, T.; SOLOVYOVA, O.; PANFILOV, A. Anisotropic conduction in the myocardium due to fibrosis: the effect of texture on wave propagation. *Scientific reports*, Nature Publishing Group UK London, v. 10, n. 1, p. 764, 2020.

CAMPOS, F. O. et al. Electroanatomical characterization of atrial microfibrosis in a histologically detailed computer model. *IEEE Transactions on Biomedical Engineering*, IEEE, v. 60, n. 8, p. 2339–2349, 2013.

LAWSON, B. A. et al. Variability in electrophysiological properties and conducting obstacles controls re-entry risk in heterogeneous ischaemic tissue. *Philosophical Transactions of the Royal Society A: Mathematical, Physical and Engineering Sciences*, The Royal Society, v. 378, n. 2173, 2020.

O'HARA, R. P. et al. Personalized computational heart models with t1-mapped fibrotic remodeling predict sudden death risk in patients with hypertrophic cardiomyopathy. *Elife*, eLife Sciences Publications Limited, v. 11, p. e73325, 2022.

PEREIRA, J. et al. Computational modeling of sources of cardiac arrythmia to determine their effect on generating arrythmias: Ischemia, diffuse fibrosis, and long qt syndrome. In: SPRINGER. *Brazilian Congress on Biomedical Engineering*. [S.l.], 2024. p. 554–563.

SOARES, T. de J. et al. Uncovering arrhythmic substrate in a heart failure patient using digital twins. *Computing in Cardiology*, Computing in Cardiology, v. 52, 2025.

TRAYANOVA, N. A.; CHANG, K. C. How computer simulations of the human heart can improve anti-arrhythmia therapy. *The Journal of physiology*, Wiley Online Library, v. 594, n. 9, p. 2483–2502, 2016.

CLAYTON, R. H. et al. Models of cardiac tissue electrophysiology: progress, challenges and open questions. *Progress in biophysics and molecular biology*, Elsevier, v. 104, n. 1-3, p. 22–48, 2011.

HASSAN, S.; BARRETT, C. J.; CROSSMAN, D. J. Imaging tools for assessment of myocardial fibrosis in humans: the need for greater detail. *Biophysical reviews*, Springer, v. 12, n. 4, p. 969–987, 2020.

RAVASSA, S. et al. Cardiac fibrosis in heart failure: Focus on non-invasive diagnosis and emerging therapeutic strategies. *Molecular aspects of medicine*, Elsevier, v. 93, p. 101194, 2023.

SAHIMI, M. *Applications of percolation theory*. [S.l.]: CRC Press, 1994.

CIACCIO, E. J. et al. Source-sink mismatch causing functional conduction block in re-entrant ventricular tachycardia. *JACC: Clinical Electrophysiology*, American College of Cardiology Foundation Washington, DC, v. 4, n. 1, p. 1–16, 2018.

FENTON, F. H. et al. Multiple mechanisms of spiral wave breakup in a model of cardiac electrical activity. *Chaos: An Interdisciplinary Journal of Nonlinear Science*, American Institute of Physics, v. 12, n. 3, p. 852–892, 2002.

CHERRY, E. M.; FENTON, F. H. Visualization of spiral and scroll waves in simulated and experimental cardiac tissue. *New Journal of Physics*, v. 10, n. 12, p. 125016, 2008.

FENTON, F.; KARMA, A. Vortex dynamics in three-dimensional continuous myocardium with fiber rotation: Filament instability and fibrillation. *Chaos: An Interdisciplinary Journal of Nonlinear Science*, American Institute of Physics, v. 8, n. 1, p. 20–47, 1998.

MAJUMDER, R.; NAYAK, A. R.; PANDIT, R. Scroll-wave dynamics in human cardiac tissue: lessons from a mathematical model with inhomogeneities and fiber architecture. *PLOS one*, Public Library of Science San Francisco, USA, v. 6, n. 4, p. e18052, 2011.

BIKTASHEV, V.; HOLDEN, A.; ZHANG, H. Tension of organizing filaments of scroll waves. *Philosophical Transactions of the Royal Society of London. Series A: Physical and Engineering Sciences*, The Royal Society London, v. 347, n. 1685, p. 611–630, 1994.

GETIS, A. Spatial autocorrelation. In: *Handbook of applied spatial analysis: Software tools, methods and applications*. [S.l.]: Springer, 2009. p. 255–278.

FALCONER, K. *Fractal geometry: mathematical foundations and applications*. [S.l.]: John Wiley & Sons, 2013.

IANNACCONE, P. M.; KHOKHA, M. *Fractal geometry in biological systems: an analytical approach*. [S.l.]: CRC Press, 1996.

STAUFFER, D.; AHARONY, A. *Introduction to percolation theory*. [S.l.]: Taylor & Francis, 2018.

SAHIMI, M.; HUNT, A. G. *Complex media and percolation theory*. [S.l.]: Springer, 2021.

EDELSBRUNNER, H.; HARER, J. *Computational Topology: An Introduction*. [S.l.]: American Mathematical Society, 2010.

FIRTH, D. Bias reduction of maximum likelihood estimates. *Biometrika*, JSTOR, p. 27–38, 1993.

HASTIE, T.; TIBSHIRANI, R. Generalized additive models. *Statistical science*, Institute of Mathematical Statistics, v. 1, n. 3, p. 297–310, 1986.

WOOD, S. N. *Generalized Additive Models: An Introduction with R*. [S.l.]: CRC Press, 2017.

HEIKHMAKHTIAR, A. K.; TEKLE, A. A.; LIM, K. M. Influence of fibrosis amount and patterns on ventricular arrhythmogenesis and pumping efficacy: computational study. *Frontiers in Physiology*, Frontiers Media SA, v. 12, p. 644473, 2021.

NEZLOBINSKY, T.; OKENOV, A.; PANFILOV, A. Multiparametric analysis of geometric features of fibrotic textures leading to cardiac arrhythmias. *Scientific Reports*, Nature Publishing Group UK London, v. 11, n. 1, p. 21111, 2021.

GIARDINI, F. et al. Correlative imaging integrates electrophysiology with three-dimensional murine heart reconstruction to reveal electrical coupling between cell types. *Nature Cardiovascular Research*, Nature Publishing Group UK London, v. 4, n. 11, p. 1466–1486, 2025.

PERLIN, K. An image synthesizer. *ACM Siggraph Computer Graphics*, ACM New York, NY, USA, v. 19, n. 3, p. 287–296, 1985.

COSTA, C. M. et al. Modeling the electrophysiological properties of the infarct border zone. *Frontiers in physiology*, Frontiers Media SA, v. 9, p. 356, 2018.

GOLDMAN, D. Theoretical models of microvascular oxygen transport to tissue. *Microcirculation*, Wiley Online Library, v. 15, n. 8, p. 795–811, 2008.

GONZALEZ, R. C.; WOODS, R. E. *Digital Image Processing*. 4th. ed. New York: Pearson, 2018.

MORAN, P. A. Notes on continuous stochastic phenomena. *Biometrika*, JSTOR, v. 37, n. 1/2, p. 17–23, 1950.

TSUI, T. et al. Spatial clustering of waste reuse in a circular economy: A spatial autocorrelation analysis on locations of waste reuse in the netherlands using global and local moran's i. *Frontiers in Built Environment*, Frontiers Media SA, v. 8, p. 954642, 2022.

CAPTUR, G. et al. The fractal heart—embracing mathematics in the cardiology clinic. *Nature Reviews Cardiology*, Nature Publishing Group UK London, v. 14, n. 1, p. 56–64, 2017.

XIE, W.-H. et al. Prognostic value of left ventricular trabeculae fractal analysis in patients with dilated cardiomyopathy. *Journal of Cardiovascular Magnetic Resonance*, Elsevier, v. 26, n. 1, p. 101005, 2024.

LIEBOVITCH, L. S.; TOTH, T. A fast algorithm to determine fractal dimensions by box counting. *physics Letters A*, Elsevier, v. 141, n. 8-9, p. 386–390, 1989.

STENSEKE, J. Persistent homology and the shape of evolutionary games. *Journal of theoretical biology*, Elsevier, v. 531, p. 110903, 2021.

CORMEN, T. H. et al. *Introduction to algorithms*. [S.l.]: MIT press, 2022.

ALONSO, S.; BÄR, M. Reentry near the percolation threshold in a heterogeneous discrete model for cardiac tissue. *Physical review letters*, APS, v. 110, n. 15, p. 158101, 2013.

VIGMOND, E. et al. Percolation as a mechanism to explain atrial fractionated electrograms and reentry in a fibrosis model based on imaging data. *Heart rhythm*, Elsevier, v. 13, n. 7, p. 1536–1543, 2016.

TUSSCHER, K. H. T.; PANFILOV, A. V. Cell model for efficient simulation of wave propagation in human ventricular tissue under normal and pathological conditions. *Physics in Medicine & Biology*, v. 51, n. 23, p. 6141–6156, 2006.

BERG, L. A. et al. Toward cardiac electrophysiology digital twins with an efficient open source scalable solver on gpu clusters. *Scientific Reports*, Nature Publishing Group UK London, 2026.

OLIVEIRA, R. S. et al. Performance evaluation of gpu parallelization, space-time adaptive algorithms, and their combination for simulating cardiac electrophysiology. *International journal for numerical methods in biomedical engineering*, Wiley Online Library, v. 34, n. 2, p. e2913, 2018.

SUNDNES, J.; MARDAL, K.-A.; CAI, X. On the computational complexity of the bidomain and the monodomain models of electrophysiology. *Annals of biomedical engineering*, 2006.

LAWSON, B. A. et al. Homogenisation for the monodomain model in the presence of microscopic fibrotic structures. *Communications in Nonlinear Science and Numerical Simulation*, Elsevier, v. 116, p. 106794, 2023.

GOKHALE, T. A. et al. Microheterogeneity-induced conduction slowing and wavefront collisions govern macroscopic conduction behavior: A computational and experimental study. *PLoS Computational Biology*, Public Library of Science San Francisco, CA USA, v. 14, n. 7, p. e1006276, 2018.

FARQUHAR, M. E. et al. Graph-based homogenisation for modelling cardiac fibrosis. *Journal of Computational Physics*, Elsevier, v. 459, p. 111126, 2022.

HARRIS, A. B. Effect of random defects on the critical behaviour of ising models. *Journal of Physics C: Solid State Physics*, v. 7, n. 9, p. 1671–1692, 1974.

KLÉBER, A. G.; RUDY, Y. Basic mechanisms of cardiac impulse propagation and associated arrhythmias. *Physiological reviews*, American Physiological Society, v. 84, n. 2, p. 431–488, 2004.

CHERRY, E. M.; FENTON, F. H.; JR, R. F. G. Mechanisms of ventricular arrhythmias: a dynamical systems-based perspective. *American Journal of Physiology-Heart and Circulatory Physiology*, American Physiological Society Bethesda, MD, v. 302, n. 12, p. H2451–H2463, 2012.

BALABAN, G. et al. 3d electrophysiological modeling of interstitial fibrosis networks and their role in ventricular arrhythmias in non-ischemic cardiomyopathy. *IEEE Transactions on Biomedical Engineering*, IEEE, v. 67, n. 11, p. 3125–3133, 2020.

PANDIT, S. V.; JALIFE, J. Rotors and the dynamics of cardiac fibrillation. *Circulation research*, Lippincott Williams & Wilkins Hagerstown, MD, v. 112, n. 5, p. 849–862, 2013.

HARTLEY, A. et al. Size matters in atrial fibrillation: the underestimated importance of reduction of contiguous electrical mass underlying the effectiveness of catheter ablation. *EP Europace*, Oxford University Press, v. 23, n. 11, p. 1698–1707, 2021.

CHERRY, E. M.; FENTON, F. H. Effects of boundaries and geometry on the spatial distribution of action potential duration in cardiac tissue. *Journal of theoretical biology*, Elsevier, v. 285, n. 1, p. 164–176, 2011.

RAVELLI, F. et al. Quantitative assessment of transmural fibrosis profile in the human atrium: evidence for a three-dimensional arrhythmic substrate by slice-to-slice histology. *Europace*, Oxford University Press US, v. 25, n. 2, p. 739–747, 2023.

FERRERO, J. M.; GONZALEZ-ASCASO, A.; MATAS, J. F. R. The mechanisms of potassium loss in acute myocardial ischemia: New insights from computational simulations. *Frontiers in physiology*, Frontiers Media SA, v. 14, p. 1074160, 2023.

MIRAGOLI, M.; GAUDESIUS, G.; ROHR, S. Electrotonic modulation of cardiac impulse conduction by myofibroblasts. *Circulation research*, Lippincott Williams & Wilkins, v. 98, n. 6, p. 801–810, 2006.

MIRAGOLI, M.; SALVARANI, N.; ROHR, S. Myofibroblasts induce ectopic activity in cardiac tissue. *Circulation research*, Lippincott Williams & Wilkins, v. 101, n. 8, p. 755–758, 2007.

SIMON-CHICA, A.; LOEWE, A.; KOHL, P. Models of cardiomyocyte–non-myocyte electrical interactions. *The Journal of Physiology*, Wiley Online Library, v. 604, n. 4, p. 1607–1628, 2026.

ROG-ZIELINSKA, E. A. et al. The living scar–cardiac fibroblasts and the injured heart. *Trends in molecular medicine*, Elsevier, v. 22, n. 2, p. 99–114, 2016.

GOURDIE, R. G.; DIMMELER, S.; KOHL, P. Novel therapeutic strategies targeting fibroblasts and fibrosis in heart disease. *Nature reviews Drug discovery*, Nature Publishing Group, v. 15, n. 9, p. 620–638, 2016.

WANG, Y. et al. Fibroblasts in heart scar tissue directly regulate cardiac excitability and arrhythmogenesis. *Science*, American Association for the Advancement of Science, v. 381, n. 6665, p. 1480–1487, 2023.

NIEDERER, S. A.; LUMENS, J.; TRAYANOVA, N. A. Computational models in cardiology. *Nature reviews cardiology*, Nature Publishing Group UK London, v. 16, n. 2, p. 100–111, 2019.

TRAYANOVA, N. A. et al. Computational modeling of cardiac electrophysiology and arrhythmogenesis: toward clinical translation. *Physiological reviews*, American Physiological Society Rockville, MD, 2024.

AREVALO, H. J. et al. Arrhythmia risk stratification of patients after myocardial infarction using personalized heart models. *Nature communications*, Nature Publishing Group UK London, v. 7, n. 1, p. 11437, 2016.

APPENDIX A – Extended Topological and Morphological Characterization

Este elemento é opcional. Apresenta um texto ou documento elaborado pelo autor com o objetivo de complementar sua argumentação, sem prejuízo da unidade nuclear do trabalho.

Figure 31 – Bivariate pairplot of structural metrics for 2D domains. The scatter plots reveal highly non-linear relationships and complex morphological clustering. Phenotypes are distinctively separated in specific multi-dimensional projections, highlighting the potential of these metrics as robust features for machine learning classification. The evaluated metrics are defined as follows: Moran's I (I), Aspect Ratio (AR), Fractal Dimension (D_f), Betti 0 (β_0), Betti 1 (β_1), and Normalized Mean Cluster Size ($\hat{S}$).

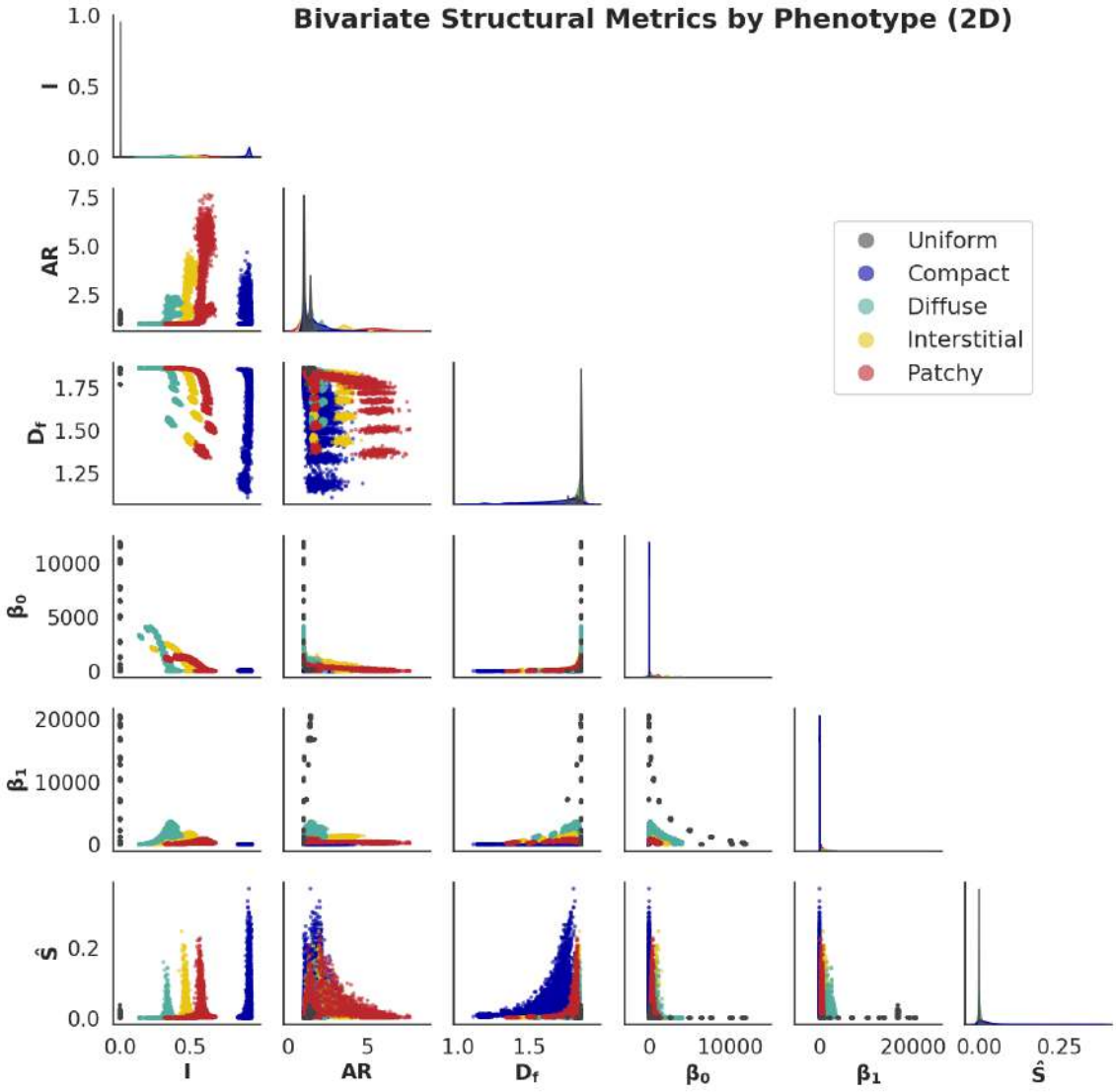

Source: Elaborated by the author (2026).

Figure 32 – Bivariate pairplot of structural metrics for 3D domains. The evaluated metrics are defined as follows: Moran's I (I), Aspect Ratio (AR), Fractal Dimension (D_f), Betti 0 (β_0), Betti 1 (β_1), Betti 2 (β_2), and Normalized Mean Cluster Size ($\hat{S}$).

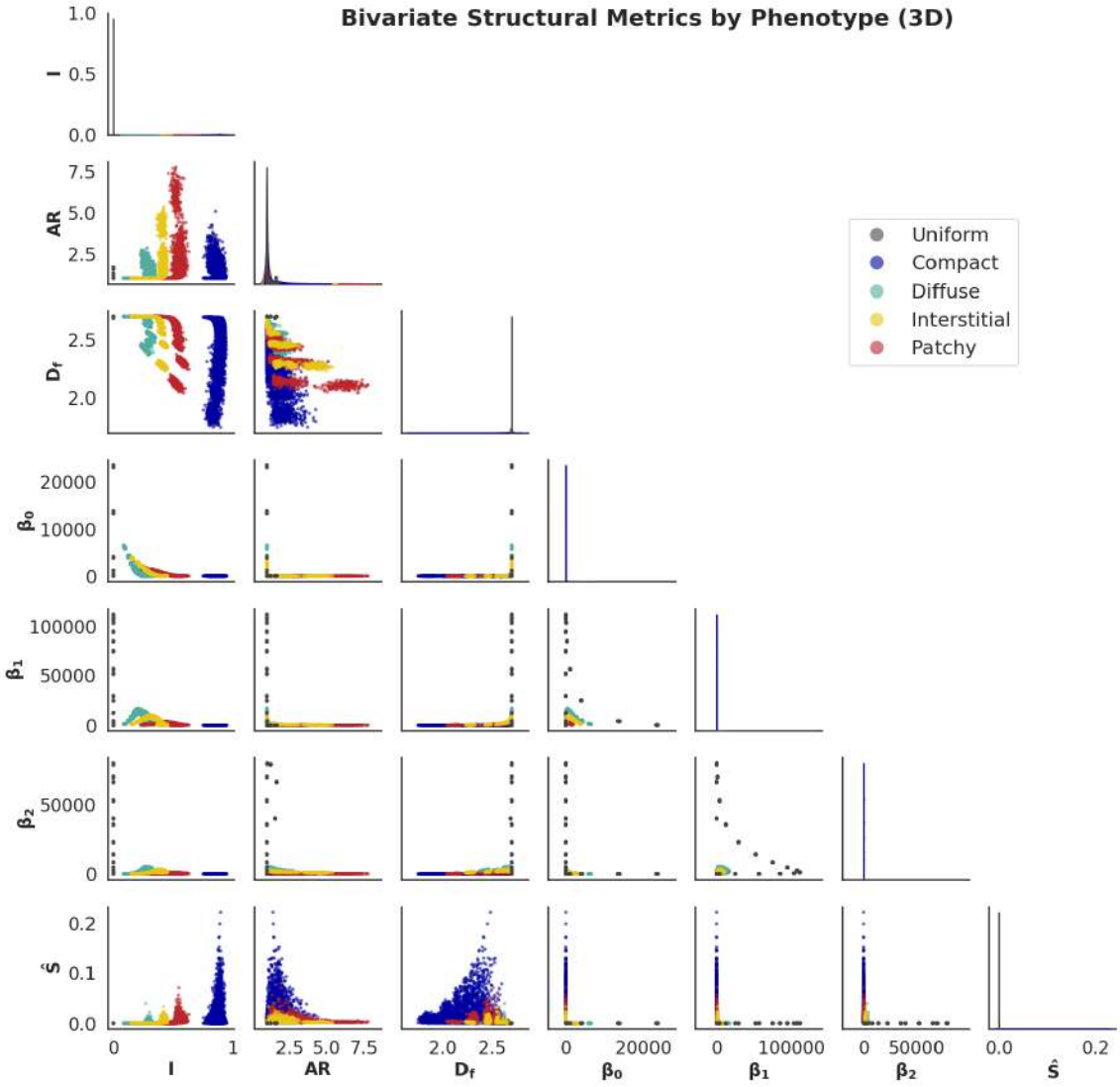

Source: Elaborated by the author (2026).

Figure 33 – Spearman versus Pearson correlation matrices for structural metrics in 2D. The generally stronger correlation coefficients in the Spearman matrix indicate that the interdependencies between topological features are governed by non-linear geometric scaling rather than simple linear proportionality. The evaluated metrics are defined as follows: Moran's I (I), Aspect Ratio (AR), Fractal Dimension (D_f), Betti 0 (β_0), Betti 1 (β_1), and Normalized Mean Cluster Size ($\hat{S}$).

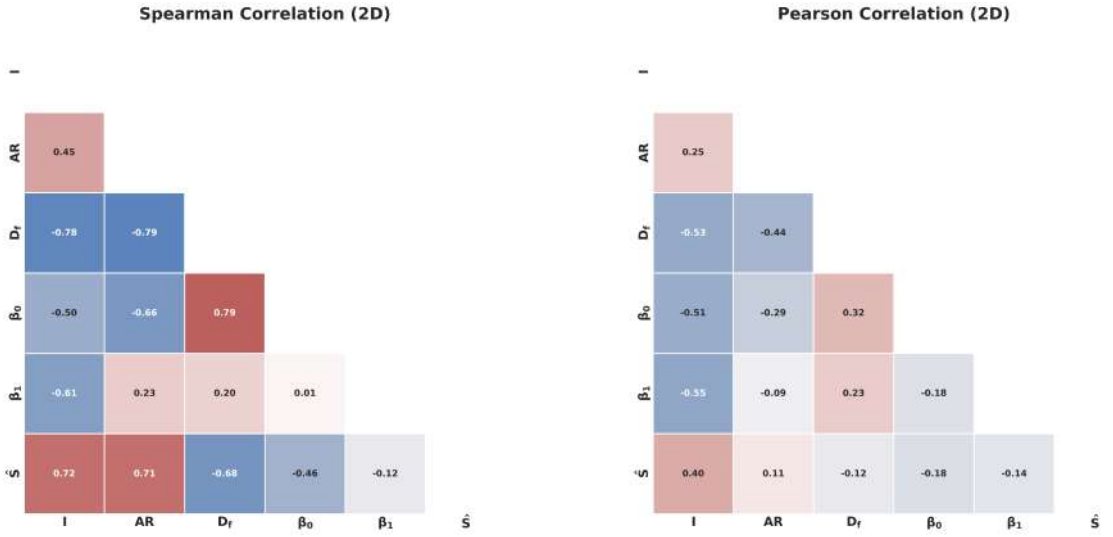

Source: Elaborated by the author (2026).

Figure 34 – Spearman versus Pearson correlation matrices for structural metrics in 3D. Consistent with the 2D results, rank-based Spearman correlations capture the complex spatial constraints of the 3D domain more effectively than linear models. The evaluated metrics are defined as follows: Moran's I (I), Aspect Ratio (AR), Fractal Dimension (D_f), Betti 0 (β_0), Betti 1 (β_1), Betti 2 (β_2), and Normalized Mean Cluster Size ($\hat{S}$).

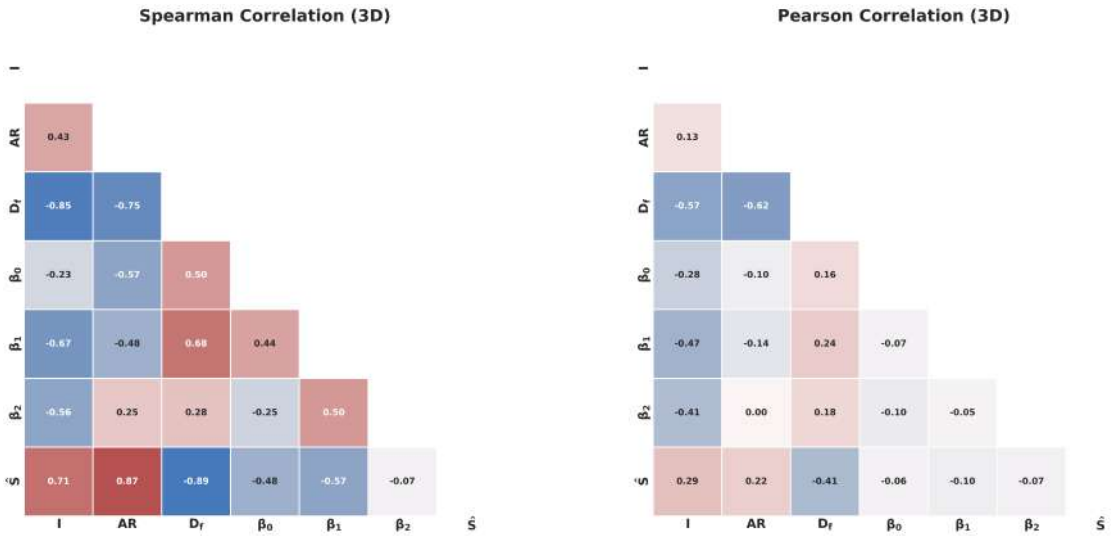

Source: Elaborated by the author (2026).

APPENDIX B – Non-linear Statistical Modeling of Arrhythmogenic Vulnerability

Figure 35 – GAM fit predicting the probability of sustained reentry in Scenario I. Shaded areas represent 95% confidence intervals. All active spatially correlated phenotypes follow non-linear bell-shaped distributions. Deviance explained = 98.9%, with all smooth terms achieving statistical significance ($p < 0.001$).

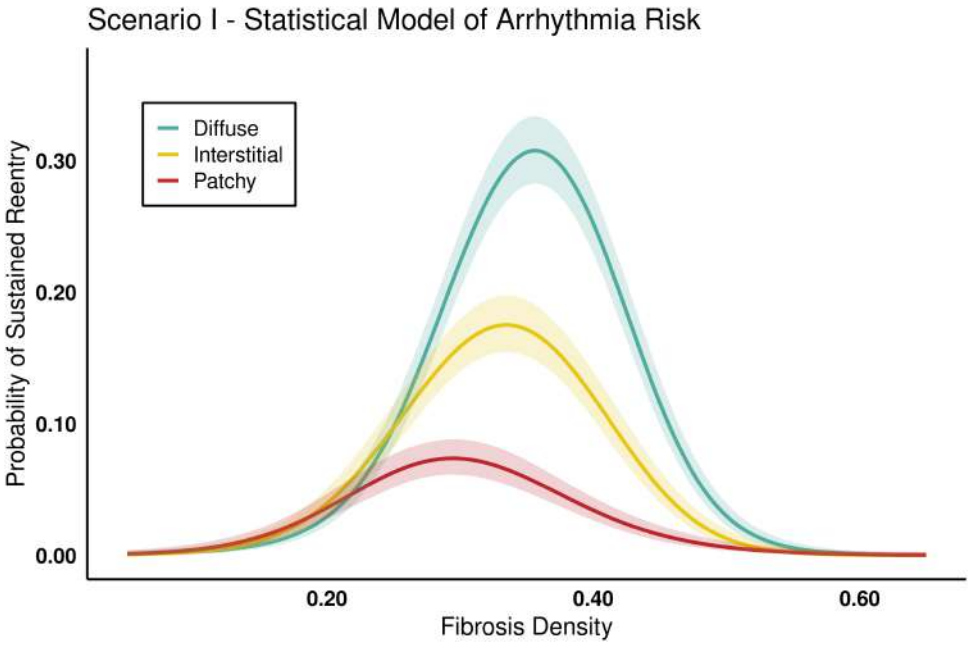

Source: Elaborated by the author (2026).

Table 6 – Estimated peak vulnerability predicted by the GAM for active phenotypes in Scenario I. Values are derived from the maximum probability coordinates of the non-linear smooths.

Phenotype	Critical Density	Max Prob.	CI Lower	CI Upper
Diffuse	35.8%	30.8%	28.3%	33.4%
Interstitial	33.3%	17.5%	15.4%	19.8%
Patchy	29.4%	7.4%	6.1%	8.8%

Source: Elaborated by the author (2026).

Figure 36 – GAM fit predicting the probability of sustained reentry for the active phenotypes in Scenario II. Shaded regions denote 95% confidence intervals. The overall model fit is robust (Deviance explained = 96.6%). All smooth terms yielded $p < 0.001$, except for the *patchy* architecture ($p \approx 0.07$), a marginal significance reflecting the extreme rarity of sustained events in this topology.

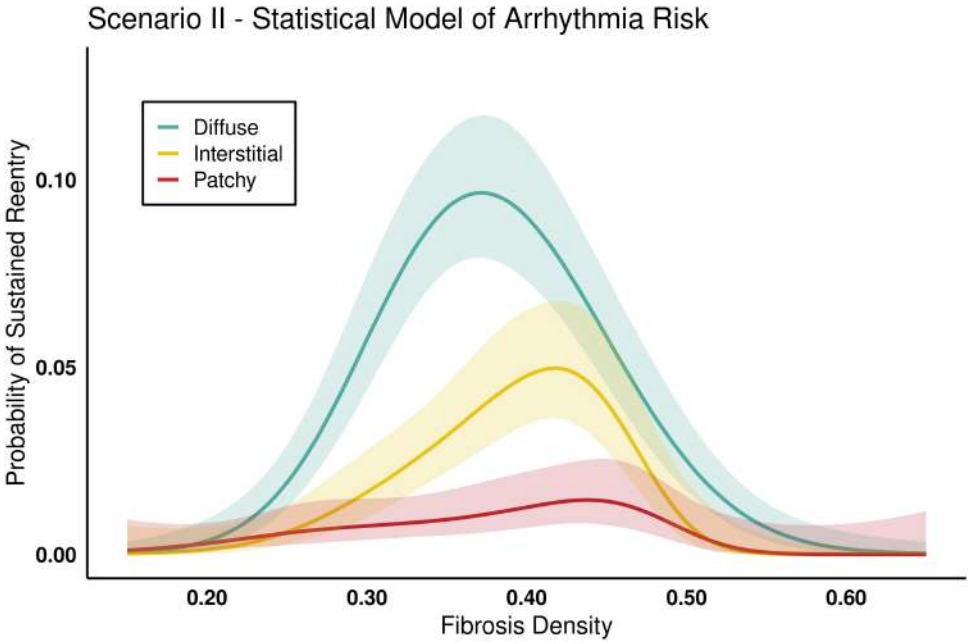

Source: Elaborated by the author (2026).

Table 7 – Estimated peak vulnerability predicted by the GAM for active phenotypes in Scenario II. Densities correspond to the core fibrosis concentration. Values are derived from the maximum probability coordinates of the non-linear smooths.

Phenotype	Critical Density	Max Prob.	CI Lower	CI Upper
Diffuse	37.1%	9.7%	7.9%	11.7%
Interstitial	41.9%	5.0%	3.6%	6.8%
Patchy	43.9%	1.4%	0.8%	2.5%

Source: Elaborated by the author (2026).

Table 8 – Estimated peak vulnerability predicted by the GAM for active phenotypes in Scenario III. Values are derived from the maximum probability coordinates of the non-linear smooths.

Phenotype	Critical Density	Max Prob.	CI Lower	CI Upper
Diffuse	75.9%	22.3%	19.7%	25.0%
Interstitial	78.2%	21.9%	19.2%	24.9%
Patchy	78.9%	13.4%	11.5%	15.6%

Source: Elaborated by the author (2026).

Figure 37 – GAM fit predicting the probability of sustained reentry in Scenario III. Shaded regions denote 95% confidence intervals. The probability peaks are extensively delayed ($> 75\%$), corroborating the massive structural density required to compromise volumetric transmural conduction. The statistical fit captures the non-linear dynamics with high fidelity (Deviance explained $= 98.8\%$), with all respective smooth terms yielding $p < 0.001$.

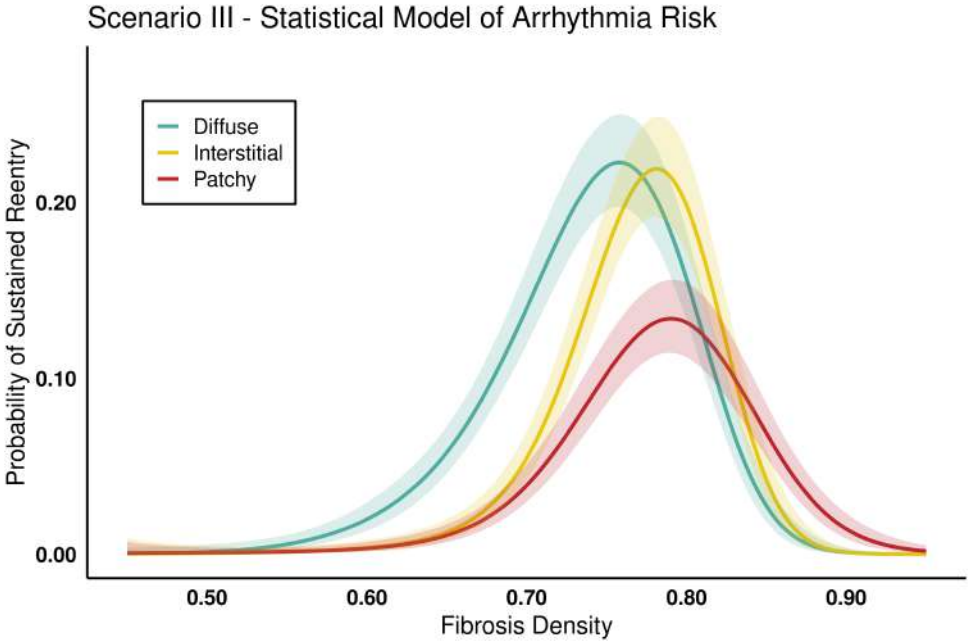

Source: Elaborated by the author (2026).